Doctoral Dissertation

博士論文

The Extreme Universe and Multi-Wavelength Sky Probed by TeV Gamma-Ray Observations: Pulsar TeV Halos, Radio Emission from Quiescent Galaxies, and Black-Hole Jets

(TeV ガンマ線観測で探る極限宇宙と多波長の空：パルサー TeV ハロー、非星形成銀河の電波放射、ブラックホール・ジェット)

A Dissertation Submitted for the Degree of Doctor of Philosophy

December, 2020

令和 2 年 12 月博士（理学）申請

Department of Astronomy, Graduate School of Science

The University of Tokyo

東京大学大学院 理学系研究科 天文学専攻

Takahiro Sudoh

須藤 貴弘

Acknowledgments

I would like to start by expressing my gratitude and respect to my supervisor, Tomonori Totani, for the continuous support and encouragement over my years in graduate school. I've learned a lot from his deep insight into physics. He has also provided me with a number of insights about critical thinking and reading.

I'm deeply indebted to John Beacom, who hosted me during my stay in the Ohio State University and has helped me a lot since then. We've had many stimulating discussions, from which I've learned a lot about scientific and creative thinking. He has also provided valuable advice on science, communication, and careers.

I would like to thank collaborators of the papers compiled in this dissertation. Tim Linden has shared with me deep knowledge on the high-energy astrophysics and data analysis and also helped me a lot with writing and presentation. Dmitry Khangulyan and Yoshiyuki Inoue have shared with me a number of helpful insights into relativistic sources and nonthermal radiation in many interesting and informative discussions.

I am also grateful to collaborators during my PhD researches: Dan Hooper, Kazumi Kashiyama, Norita Kawanaka, Ryu Makiya, Masahiro Nagashima, Ken Osato, and Naomi Tsuji. They have provided helpful insights into cosmology, galaxies, and high-energy astrophysics.

The papers compiled in this dissertation have been helped by many researchers. I am grateful for helpful discussions and comments on my work and manuscript from Felix Aharonian, Katie Auchettl, Valenti Bosch-Ramon, Shigeo Kimura, Kohta Murase, Samir Salim, and Todd Thompson. I thank Gülay Gürkan for providing us their data. I am grateful to Sophie Beacom for help with Fig. 2.1 in this dissertation.

My sincere thanks also goes to members of our group: Shotaro Yamasaki, Lin Haoxiang, Daichi Tsuna, Ryota Baba, Hidetoshi Omiya, Minori Shikauchi, and Naoya Shimono. I would like to thank colleagues, teachers, and staff of the Department of Astronomy in the University of Tokyo. I am also grateful to the members of CCAPP and the Ohio State University for warmly welcoming me. I also thank Sipra Pimputkar, at whose house I was staying, for many types of support during my time in Ohio State.

I am supported by Research Fellowship of Japan Society for the Promotion of Science (JSPS), and also supported by JSPS KAKENHI Grant Number JP18J20943. I am also grateful to acknowledge the support by ANRI Fellowship.

Finally, I would like to express my deepest appreciation to my family for their unwavering support. And I would like to extend my deepest gratitude to my wife, Misaki, for relaxing, enjoyable, and happy time at home every day.

Abstract

Observations of very-high-energy (VHE) γ-rays are important in finding powerful particle accelerators in the Galaxy and probing their nature. Recent progress in TeV γ-ray astrophysics has lead to new discoveries. This thesis studies their theoretical implications, focusing on the following four topics:

(1) The High-Altitude Water Cherenkov γ-ray Observatory (HAWC) has established the existence of a new source class, TeV halos, powered by electrons and positrons that have escaped from the pulsar wind nebula but remain trapped in a larger region where diffusion is inhibited. We perform population modeling of TeV halos considering the age dependence of halo formation. Our analysis highlights the potential importance of TeV halos in existing and future observations by HAWC, the High Energy Stereoscopic System (H.E.S.S.), and the Cherenkov Telescope Array (CTA). We quantify the contributions of TeV halos to the source counts and the diffuse Galactic disk emission. Further, we show that future observations of TeV halos are useful to constrain the statistical properties of pulsars at birth.

(2) HAWC data also show marginal evidence for the γ-ray emission around recycled/millisecond pulsars, which would indicate that they efficiently produce cosmic-ray electrons. These electrons can produce synchrotron radiation by interacting with the galactic magnetic field, contributing to the radio luminosity. We show that this emission can dominate the radio luminosities of massive quiescent galaxies. This scenario can explain recent observations that found a peculiar radio excess in galaxies with high stellar masses and low star-formation rates. We discuss the implications for the radio–far-infrared correlation, the observation of radio excesses in nearby galaxies, and local electron and positron observations.

(3) HAWC has reported the detection of the jets of the Galactic microquasar SS433. We construct a model of particle acceleration, cooling, and transport in the astrophysical jets to study the physics implication of this detection. Our model can account for the radio, X-ray, and VHE emission from this object. We find that the acceleration process should be efficient, which could be realized by diffusive shock acceleration close to the Bohm limit. This suggests that the jets of SS433 can accelerate protons beyond PeV energies.

(4) H.E.S.S. recently reported that the VHE γ-ray emission from Centaurus A is extended along the jet direction beyond a kiloparsec from the core. We use this new observation to constrain the physical conditions of the kiloparsec jet and study the origin of the nonthermal emission. We show that the diffuse jet is weakly magnetized and energetically dominated by thermal particles. We then propose that knots are the sites of both amplified magnetic field and particle (re)acceleration, but the magnetic field energy is sufficiently weak, such that particles in the knots are in the slow cooling regime. We show that the entire kiloparsec-scale diffuse emission could be powered by particles that are accelerated at and escaped from knots.

Contents

Chapter 1

Introduction

Observations of cosmic rays have revealed that the Milky Way has extreme sources that are capable of accelerating particles to very high energies (VHE; >100 GeV) (e.g., Berezinskii et al., 1990; Grenier et al., 2015). However, the origin of these cosmic rays has been a long-standing mystery (Baade & Zwicky, 1934), because the magnetic diffusion of charged particles prevents us from pointing to the location of their production sites. Cosmic rays produce various nonthermal emission (photons and neutrinos) at the acceleration site and during the propagation, providing us a valuable hint toward understanding the origin of cosmic rays (Funk, 2015).

In the past decade, γ-ray observations by *Fermi* have drastically improved our understanding of the high-energy (HE; > 100 MeV) sky (Atwood et al., 2009). In particular, it has been established that the most prominent source of GeV γ-rays is the Galactic disk itself, which is producing γ-rays via hadronic interactions (Ackermann et al., 2012). Additionally, *Fermi* has detected more than five thousand Galactic and extragalactic HE sources (Abdollahi et al., 2020), which indicates that various classes of astrophysical objects can produce nonthermal radiation. These observations have resulted in significant consequences for our understanding of cosmic-ray physics, extreme environments and phenomena, and emission from galaxies.

In the TeV range, the sky starts to be dominated by emission from individual sources, providing more information on the accelerators of cosmic rays. This energy range is of particular importance in searching for "PeVatrons", the most extreme particle accelerators in the Milky Way that are capable of accelerating protons up to energies of $\sim$ 1 PeV, which generate TeV-scale γ-rays. Our understanding of the TeV sky is limited:

- **Sources:** More than a hundred Galactic sources have been detected in TeV γ-rays. However, more than half of them are "unidentified" (Abdalla et al., 2018a; Abeysekara et al., 2017c; Albert et al., 2020) – the natures of them and emission mechanisms are not determined yet. Unveiling their nature is of significant importance for our understanding of VHE sources in the Galaxy.
- **Disk Emission:** Diffuse TeV γ-ray emission from the Galactic disk, which is a combination of authentically diffuse radiation and contributions from unresolved sources, has also been detected by multiple telescopes (Prodanović et al., 2007; Abdo et al., 2008; Bartoli et al., 2015). However, the emission is found to be brighter than expectations from the hadronic models that can fit the GeV data. Unraveling this mystery is of significant importance for our understanding of unresolved sources of TeV γ-rays and

the propagation and interactions of VHE particles.

To tackle these fundamental problems, observations are crucial. Over the last decades, imaging atmospheric Cherenkov telescopes (IACTs) like VERITAS, MAGIC, and H.E.S.S. have played substantial roles. They have considerably increased source counts in the Milky Way (Aharonian et al., 2006). They have also made significant progress in our understanding of the extragalactic sky. One of the latest and notable results is that H.E.S.S. has resolved the emission from the nearby radio galaxy Centaurus A (Cen A) (Abdalla et al., 2020) for the first time in the TeV regime, which indicates the power of high angular resolutions achieved by the IACT technique.

While IACTs have made great discoveries, recent developments in the water-Cherenkov telescopes start to shed new light on the TeV sky. The High-Altitude Water Cherenkov γ-ray Observatory (HAWC) has made significant progress thanks to its capability to detect diffuse extended emission (Abeysekara et al., 2013, 2017b). In particular, HAWC has recently made three important discoveries. First, they have discovered "TeV Halos" around nearby pulsars (Abeysekara et al., 2017a; Linden et al., 2017), an emitting region of TeV γ-rays that extend much beyond what is classically defined as a pulsar wind nebula (PWN). Second, they have detected the jets of the Galactic microquasar SS433 for the first time in the TeV range (Abeysekara et al., 2018), showing that this object is capable of producing VHE particles. Third, they have released a catalog of nine γ-ray sources detected at energies above 56 TeV, three of which above 100 TeV (Abeysekara et al., 2020), making this the first source catalog of such extreme photon energies.

Toward the understanding of the VHE sky, neutrino observations are also crucial. IceCube has detected many astrophysical neutrinos in the TeV - PeV regime (IceCube Collaboration, 2013; Aartsen et al., 2014). The dominant sources of these neutrinos have been intensively studied but remain unknown (e.g., Murase & Waxman, 2016), marking one of the most important issues in VHE astrophysics. IceCube observations place useful constraints on the nature of VHE γ-ray sources and the origin of diffuse Galactic emission (Ahlers & Murase, 2014; Aartsen et al., 2017, 2020), thanks to its capability of differentiating hadronic/leptonic emission and probing distant and/or dense sources that cannot be studied with VHE γ-rays.

Since we have experienced notable improvements in the observational data, theoretical studies are important to connect them. In this thesis, we explore theoretical insights that can be learned from these new observations. The overall aim of this thesis is to use recent discoveries in the VHE γ-ray astronomy to (1) tackle mysteries in γ-ray astrophysics, (2) study sources and production mechanisms of cosmic rays, and (3) connect the study of VHE astrophysics to broader studies, including pulsars, relativistic jets, and galaxies.

In Chapter 2, we study the theoretical implications of the detection of TeV halos. HAWC observations find that TeV halos are bright, hard spectrum, and possibly ubiquitous to many pulsars (Linden et al., 2017). If most pulsars are surrounded by such bright halos, we would expect that they may be a major contributor to the source counts, possibly explaining many of the unidentified sources. Furthermore, since these halos are diffuse and extended, many TeV halos may remain unresolved, significantly contributing to the TeV diffuse γ-ray emission. And, in the future, we can expect more detections. The main question we address in this Chapter is: *can TeV halos be important in the existing and future TeV γ-ray observations?* We

study this for the first time performing population modeling of TeV halos. We show that they can be an important source class in the existing source counts, the diffuse emission, and in the future TeV surveys – indicating the potential importance of TeV halos for understanding mysteries in the TeV γ-ray astrophysics. We also show that TeV halo observations can be a new probe of the spin period of pulsars at birth, which has not been constrained well by previous studies of radio pulsar statistics.

The detection of TeV halos, along with observations of PWNe by IACTs, indicate that young and middle-aged pulsars are efficient accelerators of electrons. A more open question is whether recycled/millisecond pulsars (MSPs) can also efficiently produce cosmic-ray electrons and positrons. Interestingly, recent HAWC data show marginal evidence of TeV γ-ray emission around MSPs, which would imply that they also produce nonthermal electrons (Hooper & Linden, 2018b). Since MSPs have a long lifetime, they can be a major source of nonthermal radiation in galaxies that have low star-formation rates (SFRs). In line with this consideration, a recent observation has found an excess radio emission in low-SFR and high-mass galaxies (Gürkan et al., 2018). Thus, in Chapter 3, we address the following question: *can MSPs produce a significant contribution to galactic radio emission?* By order-of-magnitude estimates, we point out, for the first time, that MSPs may energetically be important in quiescent galaxies. We then analyze the observed data, showing that our MSP-based model significantly improves the fit over the standard SFR-based models. Furthermore, we show that future observations of galactic radio-SFR correlation may have useful implications on our understanding of cosmic rays and γ-rays. Our results highlight that the insights from TeV γ-ray observations are crucial for understanding multi-wavelength emission from galaxies.

In the next two chapters, we study relativistic jets from compact objects, showing that TeV γ-ray observations, combined with multi-wavelength data, have a great power to uncover physical conditions in the relativistic jets and the mechanisms with which particles are accelerated to very high energies. In Chapter 4, we study the theoretical implications of the detection of VHE γ-rays from the jets of SS433. One key question in this Chapter is: *what can we learn about the physics of particle acceleration in this object?* We construct detailed models of particle acceleration, propagation and cooling inside the jets that go beyond prior studies. We find that the jets of SS433 may be accelerating particles at extreme efficiencies that could be realized by diffusive shock acceleration at the fastest speed allowed by theory ("Bohm limit"). Our results suggest the jets of SS433 as a proton "PeVatron".

In Chapter 5, we study the theoretical implications of recent measurement of the extension of the TeV γ-ray emission from Cen A. The main question we address in this Chapter is: *what are the physical conditions and particle acceleration mechanism in the kpc-scale jets?* In particular, the kiloparsec-scale jet ("kpc-jet") of Cen A exhibits two notable features, diffuse emission and many compact knots (Kraft et al., 2002; Goodger et al., 2010). Previous studies often assumed relatively high magnetic fields throughout the jet and argued that particle acceleration should take place throughout the volume of kpc-jet. However, combining the VHE and X-ray data, we show that the kpc-jet is weakly magnetized. Then we point out that particles that are accelerated at and escaped from the knots can produce the entire diffuse kpc-scale emission.

In Chapter 6, we summarize this thesis. The chapters are independent of the others,

each focusing on different questions. However, they are closely related and should be put together in the study of mysteries in γ-ray astronomy, the origin of cosmic rays, and the multi-wavelength sky. First, toward understanding the γ-ray sky, this thesis shows that recent observational discoveries contain important implications. Chapter 2 shows that the TeV sky could be dominated by TeV halos, leptonic sources that are not prominent in the GeV sky. Additionally, our results in Chapter 3 shows that the observations of galactic radio-SFR correlation suggests MSPs as a site of efficient electron/positron production. There we discuss the potential consequence of this scenario in γ-ray astronomy. Second, toward understanding cosmic rays, VHE γ-ray telescopes provide us with one of the most powerful ways to probe the sources of hadronic and leptonic cosmic rays by revealing details of their acceleration and transport. All chapters produce significant insights. Chapters 4 and 5 are mainly concerning acceleration. Our analysis shows that (mildly) relativistic shocks are an efficient acceleration site of VHE particles. Their escape from the source and transport to the Earth are linked to our work in Chapter 2. We discuss new prospects for TeV halo detection and argue that future surveys would greatly enhance our understanding of the cosmic-ray diffusion close to the acceleration sites. Chapter 2 and 3 also discusses the importance of various types of pulsars as the origin of cosmic-ray electrons and positrons. And third, toward understanding the multi-wavelength sky, observations of VHE γ-ray and cosmic rays play unique and valuable roles. Chapter 3 most pointedly demonstrates this point, where we connect VHE observations to the interpretation of radio emission from quiescent galaxies. There we also argue that understanding TeV halos, the topic of Chapter 2, may be useful to interpret galactic-scale emission because they could have a sizable impact on the confinement of nonthermal particles in galaxies. In each chapter, we further put our studies on a broader ground, discussing their connection to various topics in astronomy, including VHE neutrinos, pulsars, and black-hole jets.

Chapter 2

TeV Halos: New Source Class Identified in TeV Gamma Ray

This chapter is based on the paper "TeV halos are everywhere: Prospects for new discoveries" by Sudoh T., Linden T., Beacom J. F., 2019, published in the Physical Review D, Volume 100, Issue 4, id.043016.

2.1 Introduction to this Chapter

Milagro observations revealed extended TeV γ-ray emission surrounding the nearby Geminga pulsar, now confirmed by HAWC (Abdo et al., 2009b; Abeysekara et al., 2017a,c). Additionally, HAWC has detected similar emission surrounding another nearby pulsar, PSR B0656+14, commonly associated with the Monogem ring (Thorsett et al., 2003), and which we refer to as the "Monogem pulsar." These sources are bright ($\sim 10^{32}$ erg s^{-1}), have hard spectra ($\sim E^{-2.2}$), and are spatially extended (~ 25 pc). In addition, H.E.S.S. has detected a number of TeV γ-ray sources coincident with pulsars or pulsar wind nebulae (PWNe) (Abdalla et al., 2018a,b). Though they refer to these as "TeV PWN," they find that many are significantly larger than expected from PWN theory (Linden et al., 2017; Khangulyan et al., 2018b; Gaensler & Slane, 2006). The sources noted above appear morphologically and dynamically distinct from PWNe detected in X-ray and radio observations.

Linden et al. (2017) identified these sources as a new γ-ray source class ("TeV Halos") and interpreted their emission as the result of electrons and positrons interacting with the ambient interstellar radiation field outside the PWN. The possibility of significantly extended leptonic emission was first predicted in Aharonian (1995), and its importance was further discussed in Aharonian et al. (1997); Aharonian (2004); Yüksel et al. (2009); Aharonian (2013). Moreover, Linden et al. (2017) showed that a large fraction of 2HWC catalog sources are coincident with pulsars, and predicted that TeV halos are a generic feature of pulsar emission.

In Fig. 2.1, we show how a TeV halo compares to other features at the site of a past core-collapse supernova explosion. For a given source, it may be that not all components are detectable or even present at the same time. A PWN, powered by the rotational energy of the central pulsar, is delimited by the contact discontinuity between the shocked pulsar wind and the ejecta or interstellar matter. An SNR, powered by the energy of the supernova explosion, is delimited by its interaction with the interstellar medium. A TeV halo is likely

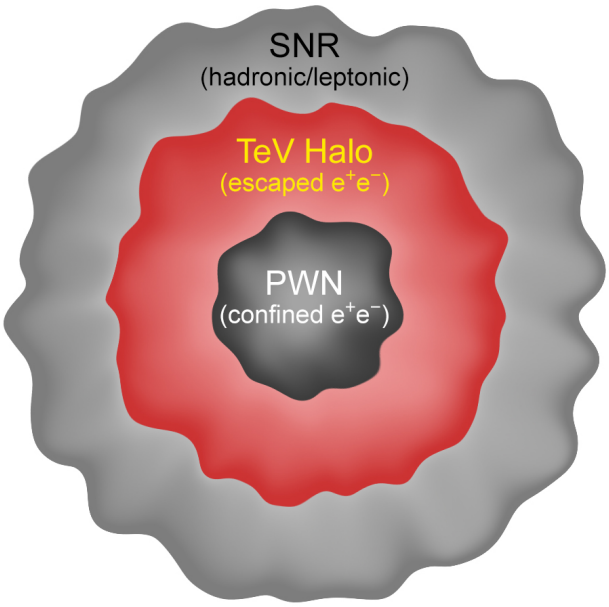

Figure 2.1. Schematic illustration of a TeV halo in relation to the more familiar PWN and supernova remnant (SNR). A TeV halo may not form early, and the SNR may be fading when the halo appears.

intermediate in size, is powered by cosmic rays diffusing away from the PWN, and does not have a well-defined boundary. The size of a PWN can be on the order of 0.1–1 pc, though some may range up to ∼10 pc (Gaensler & Slane, 2006; Kargaltsev & Pavlov, 2008), and the size of an SNR may span ∼1–100 pc (Badenes et al., 2010; Stafford et al., 2019), depending on their properties, evolutionary stages and environment. The typical size of a TeV halo is not known, but Geminga and Monogem observations indicate that it may be on the order of 10 pc for middle-aged pulsars[*1]. For the three types of object, differences in radii lead to larger differences in volumes that further support different physical origins.

The identification of TeV halos as a new source class is supported by the subsequent detection of two more TeV halos by HAWC (Riviere et al., 2017; Brisbois et al., 2018), one of which was predicted by Linden et al. (2017). However, many details about TeV halos remain unknown and further observations will have broad implications. Apart from shedding light on the properties of the TeV halos themselves, these observations will reveal new aspects of pulsar formation and evolution (Linden et al., 2017), and will probe sources of high-energy γ-rays (Hooper et al., 2018; Linden & Buckman, 2018; Hooper & Linden, 2018c) and cosmic-ray electrons and positrons (Hooper et al., 2017; Hooper & Linden, 2018a; Evoli et al., 2018; Profumo et al., 2018; Bucciantini, 2018; Tang & Piran, 2019; Xi et al., 2019).

Here, we outline a multifaceted strategy to discover more TeV halos and to constrain their evolution. We quantify the role of Galactic source searches and diffuse measurements using

[*1] Naively, one may expect that the size increases with time as $\sqrt{t}$ (i.e., diffusion) at early time, and becomes constant when it is cooling-limited. However, since we lack knowledge on how the region of slow diffusion is developed, it is still unclear how this size evolves with the system age.

water Cherenkov telescopes like HAWC. We also consider Galactic and extragalactic source surveys by imaging air Cherenkov telescopes, focusing on the Cherenkov Telescope Array (CTA). Further, we show that follow-up studies of existing TeV γ-ray sources in the H.E.S.S. catalog, especially those classified as PWN or unidentified sources, could find more TeV halos. For our overall approach, we use standard methods for pulsar population synthesis and treat the Geminga TeV halo as a prototype. Our results go significantly beyond those of prior work, yielding new insights into both the prospects for future TeV halo discoveries, and the implications of TeV halo observations for our understanding of astrophysics.

In Sec. 2.2, we briefly review the properties of TeV halos. In Sec. 2.3, we present our methods for modeling TeV halo populations. In Sec. 2.4, we compare predictions with current observations and constrain model parameters. In Sec. 2.5, we outline future directions to find more TeV halos. In Sec. 2.6, we present our conclusions.

2.2 What are TeV halos?

TeV halos are defined as the nonthermal emission produced in regions outside a PWN, but within a region where pulsar activity may dominate cosmic-ray diffusion (Linden et al., 2017; Aharonian, 1995; Aharonian et al., 1997; Aharonian, 2004; Yüksel et al., 2009). Within this region, multi-TeV γ-rays are produced by the inverse-Compton scattering of ambient photons by $\sim$10 TeV electrons and positrons accelerated by the pulsar wind termination shock. Observations indicate that the TeV halo produces bright γ-ray emission with a hard spectrum.

We begin by examining the key features of the best-studied TeV halo, Geminga, which is about 340 kyr old (Manchester et al., 2005) and believed to reside approximately 250 pc from Earth (Verbiest et al., 2012). HAWC detects TeV γ-ray emission extending to an angular size of $\sim5^\circ$, corresponding to $\sim$25 pc in physical extent (Abeysekara et al., 2017a). The differential γ-ray luminosity at 7 TeV is $2.9\times10^{31}(d/250\text{ pc})^2$ erg s^{-1}, with a local spectral index of -2.2.

The lack of gas-correlated emission indicates a leptonic origin. Within the context of an inverse-Compton model, several parameters regarding the electron population can be calculated. To produce the bright γ-ray luminosity, $\sim$10% of the total pulsar spin-down power must be converted into $e^\pm$ pairs. Furthermore, to produce the hard γ-ray spectrum, the electron population should be injected with a hard power-law spectrum between ~-1.5 and -2.3.

The most notable feature of TeV halos is their size. The Geminga TeV halo is significantly larger than its X-ray PWN, which is confined within $3'$ of the central pulsar (Posselt et al., 2017). This indicates that the electrons and positrons responsible for TeV halo emission have already escaped the PWN and are interacting with the interstellar radiation field. The TeV halo morphology is consistent with cosmic-ray diffusion, rather than advection (Abeysekara et al., 2017a). However, this diffusion must be inhibited. Assuming that the TeV halo medium is filled with the $\sim$1 eV cm^{-3} interstellar radiation field and the ~3 μG magnetic field typical of the Galactic Plane, we would expect 10 TeV $e^\pm$ to cool in $\sim$40 kyr. In the interstellar medium, electrons and positrons that propagate for $\sim$40 kyr should diffuse over a distance of $\sim$700 pc (Trotta et al., 2011). However, the TeV halo power appears to be confined within

$\sim$25 pc of the pulsar center.

TeV halo emission is not unique to Geminga. The HAWC collaboration has identified at least three other TeV halos with similar features: Monogem (111 kyr, 290 pc), PSR B0540+23 (253 kyr, 1.56 kpc), and PSR J0633+0632 (59 kyr, 1.35 kpc) (Manchester et al., 2005; Riviere et al., 2017; Brisbois et al., 2018). In addition, Linden et al. (2017) listed 13 more TeV halo candidates in the 2HWC catalog. The 2HWC survey also provides a hint of TeV halo emission around millisecond pulsars (Hooper & Linden, 2018c).

In addition to HAWC, imaging air Cherenkov telescopes like H.E.S.S., MAGIC and VERITAS have detected a number of extended TeV γ-ray sources that are associated with pulsars or PWNe observed at other wavelengths. These systems are called "TeV PWN," but many of them have an extension exceeding $\sim$10 pc (Abdalla et al., 2018a,b), while hydrodynamical simulations predict a typical PWN size on the order of 1 pc (van der Swaluw et al., 2004; Gaensler & Slane, 2006; Gelfand et al., 2009; Bucciantini, 2011; Martín et al., 2016; Ishizaki et al., 2018; Zhu et al., 2018; van Rensburg et al., 2018). More pointedly, they are usually much more extended than the size of X-ray PWN observed from the same system (Kargaltsev & Pavlov, 2010; Kargaltsev et al., 2013). These observations suggest that some of these γ-ray sources may be interpreted as TeV halos, instead of emission from confined particles inside PWNe. In particular, HESS J1825-137 has the largest radius ($\sim$50 pc; Abdalla et al., 2019) among "TeV PWN" (Khangulyan et al., 2018b). A TeV halo explanation for this source is already discussed in Aharonian (2004, 2013).

Despite the significant number of TeV halos that have been (or are potentially) detected in current surveys, many of their properties remain mysterious. In particular, we do not understand the evolution of the key observable TeV halo properties: their luminosity, spectrum, and spatial morphology. In a recent work (Linden et al., 2017), TeV halo predictions have been evaluated utilizing a "Geminga-like" model, where the ratio of the γ-ray flux to $\dot{E}/d^2$ is constant for all systems with an efficiency set to the best-fit value of Geminga, and the physical size of all TeV halos is $\sim$10 pc. On one hand, this model appears reasonably consistent with the data — choosing to instead normalize the TeV halo flux to the average γ-ray efficiency of all firmly identified TeV halos changes the normalization constant only by a factor of $\sim$2 compared to the "Geminga-like" model. On the other hand, there is nearly an order of magnitude variation in the efficiencies of individual candidate sources, the origin of which is not understood.

A key question is when a TeV halo first forms. Theoretically, high-energy cosmic rays are expected to be efficiently confined in young PWNe and quickly lose energy to adiabatic and synchrotron cooling in the strong PWN magnetic field (Rees & Gunn, 1974; Kennel & Coroniti, 1984; de Jager et al., 2009; Tanaka & Takahara, 2010; Torres et al., 2014; Vorster et al., 2013; Olmi et al., 2016). This may imply that particles do not escape into young TeV halos. Moreover, the creation of a halo may require cosmic-ray self-generated turbulence, which is produced through the resonant interactions of Alfvén waves with accelerated electrons and positrons. The growth-rate of self-generated turbulence is model dependent, but typically occurs on $>$ kyr timescales (Evoli et al., 2018).

Observationally, the Crab pulsar (964 yr, 2 kpc) does not appear to produce TeV halo emission (Aharonian et al., 2006; Albert et al., 2008; Abeysekara et al., 2017b), indicating that TeV halos may not be visible within the first kyr of pulsar evolution. An intriguing

edge case is the Vela pulsar (11 kyr, 280 pc). Vela does not appear to produce a bright TeV halo (compared to the luminosity expected if the formation efficiency is Geminga-like). However, Vela does have dim, spatially-extended emission detected in radio and GeV-TeV γ-ray observations (Abdo et al., 2010; Abramowski et al., 2012; Grondin et al., 2013; Tibaldo et al., 2018). This has historically been interpreted as a class of "relic PWN" that are left behind after the interaction of the expanding PWN and the SNR reverse shock, and which are powered by old electrons accumulated since the birth of the pulsar (Blondin et al., 2001; de Jager et al., 2008; Hinton et al., 2011; Slane et al., 2018). Interestingly, the size of this extended emission is $\sim$10 pc, comparable to that of observed TeV halos. Thus, Vela could be interpreted as a transition case, where inefficient TeV halos first form. Further TeV observations around $\sim$1–10 kyr pulsars are needed to study the properties of young systems.

Because detailed examinations of young systems are beyond the scope of the population modelling presented in this Chapter, we introduce a new parameter $T_{\rm min}$, before which pulsars are assumed to exhibit no TeV halo activity. Observations of the Crab and Vela suggests $T_{\rm min} \gtrsim$ 1–10 kyr, while Monogem and Geminga TeV halos suggest $T_{\rm min} \lesssim$ 100–300 kyr.

Another key question is whether TeV halo activity is ubiquitous to all pulsars. Theoretically, the creation of halos requires inhabited diffusion around pulsars, which might be expected for all pulsars if the turbulence is excited due to a steep cosmic-ray gradient (Evoli et al., 2018) and/or the influence of the parent SNR (Fang et al., 2019). Observationally, Linden et al. (2017) listed seven middle-aged pulsars that should be detected by HAWC, under the assumption that every pulsar has a Geminga-like TeV halo, and find that five are in fact associated with the 2HWC sources. These are consistent with the expectation that a significant fraction of pulsars have "Geminga-like" TeV halos.

We operate under the assumption that all pulsars older than $T_{\rm min}$ produce TeV halos. This can be tested in future surveys. We do not consider the maximum age of TeV halos, because late-time sources are not important due to their small spindown power.

2.3 TeV Halo Population Models

To model the population of TeV halos, we generate an ensemble of pulsars with randomly assigned initial spin periods (P_0) and magnetic fields (B_0). We assume $M = 1.4\ M_\odot$ and $R = 12$ km for all pulsars (Lattimer & Prakash, 2007). We then assign each pulsar an age ($T_{\rm age}$) drawn from a uniform distribution spanning from 0 to 1 Gyr, and calculate the pulsar spindown power as:

$$\dot{E}(t) = \frac{8\pi^4 B_0^2 R^6}{3c^3 P_0^4} \left(1 + \frac{t}{\tau_{\rm sd}}\right)^{-2}, \tag{2.1}$$

where $\tau_{\rm sd} = 3Ic^3 P_0^2 / 4\pi^2 B_0^2 R^6$ is the spindown timescale (Shapiro & Teukolsky, 1983; Hooper et al., 2018). We associate each pulsar with a randomly distributed position within the Milky Way, based on the pulsar distributions determined by previous studies. Specifically, we adopt the radial distribution of Yusifov & Küçük (2004), and a scale height of 200 pc (Porter et al., 2017a), and calculate the pulsar position relative to Earth assuming a galactocentric distance of 8.5 kpc. Our results are only slightly affected if we use the alternative spatial distributions defined in Lorimer et al. (2006). We have verified that our models are reasonably consistent with the observations of nearby neutron stars, i.e., the seven isolated neutron stars and several

pulsars younger than 1 Myr within around 500 pc (Haberl, 2005; Kaplan & van Kerkwijk, 2009). Further, we calculate the probability that the pulsed radio emission from each pulsar is beamed towards Earth following the empirical relation defined in Tauris & Manchester (1998),

$$f_{\rm beam} = \left[9 \left(\log_{10} \frac{P}{10\ {\rm s}} \right)^2 + 3 \right] \ \%. \tag{2.2}$$

Of all choices in our calculation, the most significant are those of P_0 and B_0, due to their strong dependence in Eq. 2.1: B_0^2/P_0^4 in the pre-factor and P_0^2/B_0^2 in $\tau_{\rm sd}$.

The P_0 distribution is poorly constrained (Faucher-Giguère & Kaspi, 2006; de Jager, 2008; Watters & Romani, 2011; Popov & Turolla, 2012; Noutsos et al., 2013; Igoshev & Popov, 2013; Cieślar et al., 2018; Gonthier et al., 2004; Gullón et al., 2014), because population statistics are not sensitive to it (Gonthier et al., 2004; Gullón et al., 2014). Conventionally, pulsar population models adopt a Gaussian distribution with $\langle P_0 \rangle = 300$ ms and $\sigma_{P_0} = 150$ ms, based on radio observations (Faucher-Giguère & Kaspi, 2006). However, studies of the γ-rays pulsar population hint at much smaller values $\langle P_0 \rangle = 50$ ms and $\sigma_{P_0} = 50/\sqrt{2}$ ms (Watters & Romani, 2011). In what follows, we present results for both P_0 distributions. In addition, we test an intermediate case of $\langle P_0 \rangle = 120$ ms and $\sigma_{P_0} = 60$ ms. We set a minimum spin period at the Newtonian centrifugal breakup limit, $P_{0,\rm min} = 0.85\ (M/1.4\ M_\odot)^{1/2}\ (R/12\ {\rm km})^{3/2}$ ms (Lattimer & Prakash, 2007).

For the B_0 distribution, we adopt a log-normal magnetic field distribution with mean $\langle \log_{10} B_0 \rangle = 12.65$ and variance $\sigma_{\log_{10} B_0} = 0.55$, which is derived from population studies of radio pulsars (Faucher-Giguère & Kaspi, 2006). Other studies predict magnetic fields that are larger by a factor of 2–4 (Popov et al., 2010; Gullón et al., 2014). This uncertainty is discussed in Sec. 2.4.3. We do not include any term to account for the decay of the magnetic field strength, because it occurs on timescales of >Myr, much greater than the age of the majority of detectable TeV halos.

In Fig. 2.2, we show the evolution of the spindown power for six representative pulsars. Most of the integrated spindown power is spent before $\sim \tau_{\rm sd}$, which is 4 kyr for $P_0 = 50$ ms and 160 kyr for 300 ms in the fiducial case of $B_0 = 10^{12.65}$ G (this would be more evident if we had plotted the power per log time, which would include multiplying by a factor t).

Using the ensemble of pulsars generated above, we assign a "Geminga-like" TeV halo to each pulsar that has an age older than $T_{\rm min}$. We normalize the differential γ-ray flux at 7 TeV ($\Phi_{\rm 7TeV}$) for each TeV halo relative to Geminga, using the spindown power ($\dot{E}$) and distance (d) as

$$\Phi_{\rm 7TeV} = \Phi_{\rm 7TeV}^{\mathcal{G}} \left(\frac{\dot{E}}{\dot{E}^{\mathcal{G}}} \right) \left(\frac{d^{\mathcal{G}}}{d} \right)^2 . \tag{2.3}$$

We adopt physical quantities for Geminga (superscript "$\mathcal{G}$") as summarized in Table 2.1.

In addition to directly observable parameters such as the spindown energy and the 7-TeV γ-ray flux, our models also require us to derive parameters such as the integrated γ-ray flux ($F_{\rm TeV}$) and luminosity ($L_{\rm TeV}$) for each pulsar; we calculate these above 1 TeV. To normalize these parameters to Geminga, we follow the theoretical treatment of Linden & Buckman

(2018), which calculates the inverse-Compton scattering γ-ray spectrum from Blumenthal & Gould (1970). We model the electron spectrum following Hooper et al. (2017), which derives the best-fit γ-ray spectrum from a combination of HAWC (7 TeV) and Milagro (35 TeV) observations of the Geminga TeV halo (Abeysekara et al., 2017c; Abdo et al., 2009b). Specifically, we assume that electrons are injected with a power-law index of $\alpha = 1.9$ that cuts off exponentially at $E_{\rm cut} = 49$ TeV. We adopt an energy-independent escape time of $1.8{\times}10^4$ yr from the TeV halo emission region (Hooper et al., 2017). The total $e^{\pm}$ luminosity is normalized to be $\eta\dot{E}$. We find the best fit value of $\eta = 0.12$ from the observed γ-ray flux. The derived values of $F^{\mathcal{G}}_{\rm TeV}$ and $L^{\mathcal{G}}_{\rm TeV}$ are provided in Table 2.1. We again calculate $F_{\rm TeV}$ and $L_{\rm TeV}$ for every other pulsar by scaling the best-fit Geminga values with $\dot{E}$ and d as shown in Eq. (2.3).

The 2HWC catalog reports the photon index at 7 TeV (2.23 for Geminga). If we extrapolate this spectral index down to 1 TeV and use the 7-TeV differential flux, we derive values of $F^{\mathcal{G}}_{\rm TeV}$ that fall within ~20% of the theoretically derived photon flux reported in Table 2.1. On the other hand, the values for $L^{\mathcal{G}}_{\rm TeV}$ are increased nearly by a factor of 2, and hence our calculated luminosity in Table 2.1 may be pessimistic.

In Fig. 2.3, we show the γ-ray luminosity function of Milky Way TeV halos for two different P_0 distributions and three different values of $T_{\rm min}$. We normalize the total number of Milky Way pulsars using a pulsar birth rate of 0.015 $\rm yr^{-1}$ (Lorimer et al., 2006). The upper panel shows the number weighting only, while the lower panel also includes the luminosity weighting.

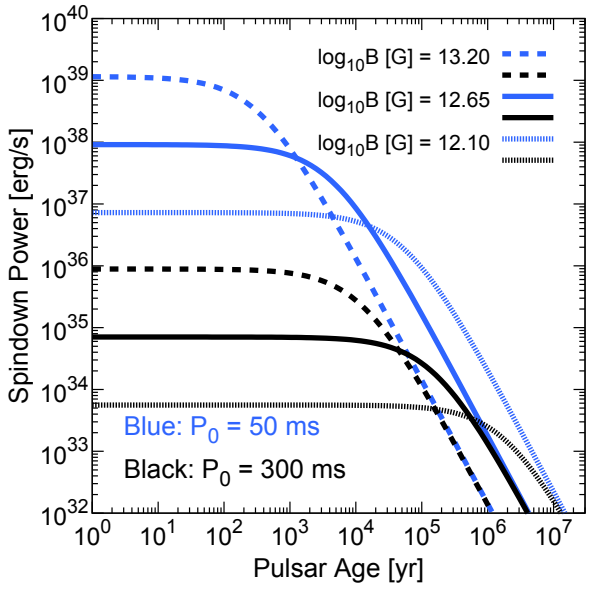

Figure 2.2. Evolution of the pulsar spindown power for six representative cases, as labeled.

Observed	$\dot{E}^{\mathcal{G}}$ [erg $\rm s^{-1}$]	$3.2{\times}10^{34}$	Manchester et al. (2005)
	$d^{\mathcal{G}}$ [pc]	250	Verbiest et al. (2012)
	$\Phi^{\mathcal{G}}_{\rm 7TeV}$ [$\rm TeV^{-1}cm^{-2}s^{-1}$]	$4.87{\times}10^{-14}$	Abeysekara et al. (2017c)
Calculated	$F^{\mathcal{G}}_{\rm TeV}$ [$\rm cm^{-2}s^{-1}$]	3.5×10^{-12}	
	$L^{\mathcal{G}}_{\rm TeV}$ [erg $\rm s^{-1}$]	$1.1{\times}10^{32}$	

Table 2.1. Physical quantities for Geminga and its TeV halo.

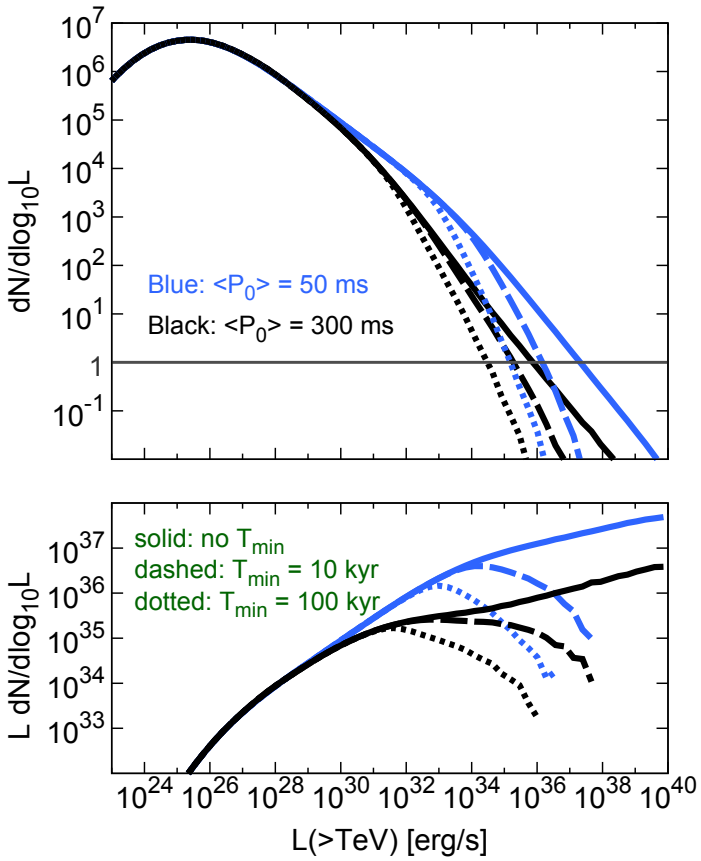

Figure 2.3. TeV γ-ray luminosity functions of TeV halos for two choices of P_0 distribution. The upper panel shows source counts and the lower panel shows the contributions to the total luminosity.

If we do not set $T_{\rm min}$, the bright end of the number count (upper panel) has a slope of $\sim L^{-0.8}$, which is driven by the distribution of P_0. As pulsars get older (above $\tau_{\rm sd}$), they lose spindown power following $\dot{E} \propto t^{-2}$ and move to the left in this plot, producing a shallower slope of $\sim L^{-0.5}$ before the peak, where pulsars with average properties $(P_0, B_0, T_{\rm age})$ reside. We do not include the effect that old pulsars may terminate their activities below the radio death line (Chen & Ruderman, 1993), because late-time sources have small γ-ray luminosities and contribute negligibly to the source count. Furthermore, due to the shallow slopes of the number count, dim sources contribute negligibly to the total Galactic emission, as shown in Fig 2.3 (bottom).

2.4 Existing Model Constraints

The range of model parameters used in our predictions below can be constrained by current data. In Sec. 2.4.1, we predict the number of TeV halos that should be detected in the 2HWC source catalog. In Sec. 2.4.2, we estimate the contribution of unresolved TeV halos to the diffuse TeV γ-ray emission across the Galactic Plane, comparing our predictions with Milagro observations. In Sec. 2.4.3, we summarize model constraints and briefly discuss uncertainties.

2.4.1 Sources in the 2HWC Catalog

The 2HWC catalog utilizes 507 days of HAWC data and identifies 39 high-significance sources within the field of view of $-20^\circ <$ decl. $< 60^\circ$. The sensitivity depends on the photon spectral index and the source declination. We adopt the average of quoted values for spectral indices of -2.5 and -2.0 and the declination dependence given in Abeysekara et al. (2017c). The best sensitivity of $4.3{\times}10^{-15}$ TeV^{-1} cm^{-2} s^{-1} (9% of the Geminga TeV halo flux) occurs at a declination of 20°, and is degraded by a factor of $\sim$2 for declinations that differ by 30°. We take into account the degradation of the flux sensitivity for sources that are larger than the size of the PSF, utilizing a model where the sensitivity decreases by a factor of $\theta_{\rm size}/\theta_{\rm PSF}$ compared to the point source sensitivity (Hinton & Hofmann, 2009). We assume a PSF size of $\theta_{\rm PSF} = 0.2^\circ$ for HAWC (Abeysekara et al., 2013). To determine the source size, we again utilize a Geminga-like model, assuming that all TeV halos have the same physical size as that of the Geminga halo ($\theta_{\rm size} = 2^\circ$ at a distance of 250 pc). We ignore source confusion, where HAWC may identify neighboring or overlapping sources as one source, because our calculations show it to be unimportant.

We constrain our TeV halo models by requiring that they do not produce too many or too few systems that would be detected in the 2HWC catalog search. We set the maximum number of potential TeV halos in the 2HWC catalog at 36, because three sources (the Crab, Mrk501, and Mrk421) are associated with objects that are definitively not TeV halos. For the minimum number, we choose 2, because Geminga and Monogem were detected while the two other sources announced by Astronomer's Telegrams (Riviere et al., 2017; Brisbois et al., 2018) did not meet the flux threshold to be included in the 2HWC catalog. Both of these choices are conservative, as they do not take into account additional information concerning individual 2HWC objects.

We can additionally constrain the number of detectable TeV halos that would have radio beams oriented towards Earth. Such sources are especially compelling because the spatial coincidence points towards a TeV halo origin. We note that while the Monogem pulsar is a firmly detected radio pulsar, the Geminga pulsar has extremely dim radio emission and would not have been detected in blind radio searches (Malofeev & Malov, 1997). Hence, we conservatively assume that at least 1 TeV halo (Monogem) has been detected in the 2HWC catalog with a radio beam oriented towards Earth.

The lower limits on the number of beamed and unbeamed TeV halos would become much stronger if the TeV halo candidates that were first identified by Linden et al. (2017) are confirmed by subsequent observations. Linden et al. (2017) finds three additional 2HWC sources that are consistent with the position of middle-aged radio pulsars, and twelve additional 2HWC sources that are consistent with the positions of younger pulsars. They estimate that only 2.6 chance coincidences would be expected if the 2HWC sources were not associated with pulsar activity. We compare our model predictions with these candidate sources.

In Fig. 2.4 (top), we show the total number of detectable TeV halos produced by our model, regardless of whether the system has a radio beam that is oriented towards Earth. This prediction should thus be compared to the total number of detected 2HWC sources. We plot results for models with initial pulsar spin periods of $\langle P_0 \rangle = 50$ ms, 120 ms, and 300 ms,

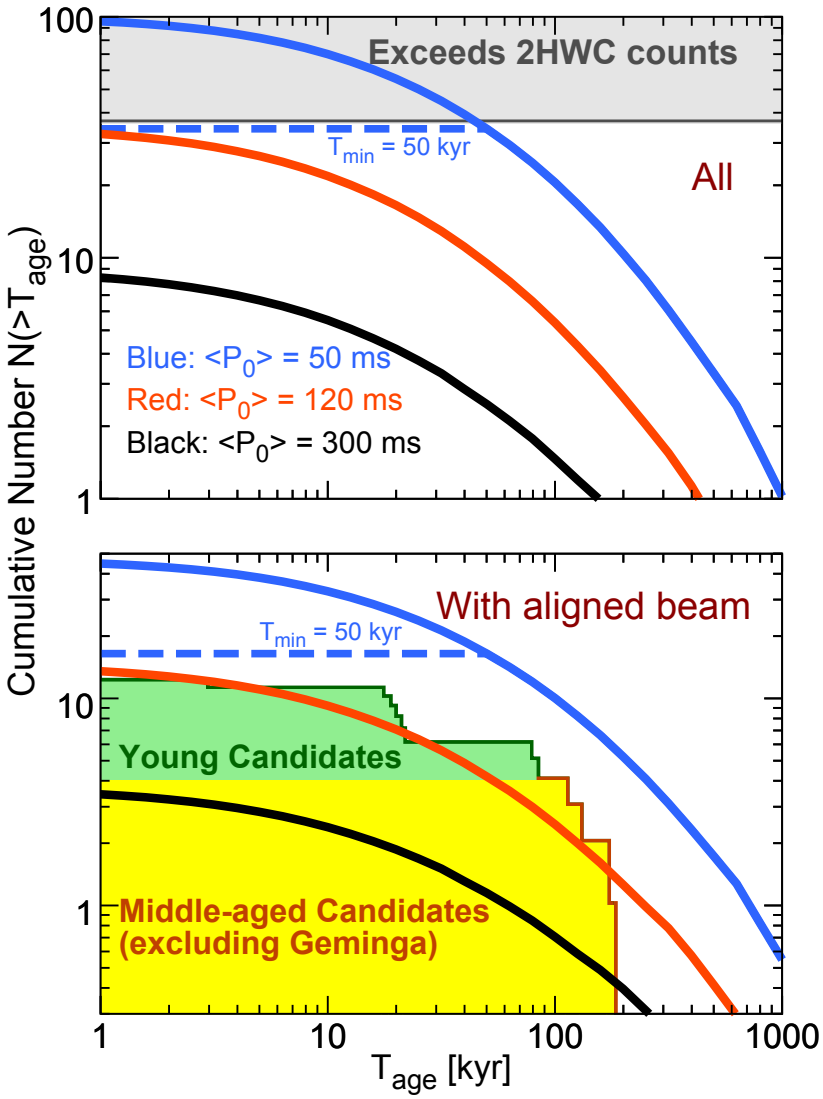

Figure 2.4. Predicted numbers of TeV halos in the 2HWC catalog for all sources (top) and sources with radio beams aligned towards Earth (bottom), for different choices of $\langle P_0 \rangle$ and $T_{\rm min}$. Unmarked curves have $T_{\rm min} = 0$. In the bottom panel, the cumulative histogram for TeV halo candidates is also shown, separated into young and middle-aged candidates following Linden et al. (2017).

and find that our parameters allow us to vary the predicted number of detected halos by about one order of magnitude.

This variation translates into a constraint on the value of $T_{\rm min}$, a timescale that is needed for a typical pulsar to develop a TeV halo. If typical pulsars are born with relatively large spin periods (e.g., $\langle P_0 \rangle = 300$ ms), TeV halos produce about 10 sources in models where $T_{\rm min} = 0$. In this case, the lower bound of $T_{\rm min}$ is not strongly constrained by 2HWC data. On the other hand, if we utilize our minimum value of $\langle P_0 \rangle = 50$ ms, TeV halos produce about 100 sources in models where $T_{\rm min} = 0$. Because this exceeds the total number of 2HWC sources, this would require a simultaneous constraint of $T_{\rm min} \gtrsim 50$ kyr. In the reminder of the section, we adopt $T_{\rm min} = 50$ kyr for the case of $\langle P_0 \rangle = 50$ ms as the most optimistic case, which predicts that most of the 39 sources in the 2HWC catalog are TeV halos. Models with $\langle P_0 \rangle = 120$ ms provide a critical case, approximately saturating the number of detectable

TeV halos in models with $T_{\rm min}$ =0. Thus, in this case, the value of $T_{\rm min}$ is not strongly constrained at this point, but may be better constrained if future observations indicate that several 2HWC sources are not TeV halos.

To produce at least two detectable TeV halos, we need to set $T_{\rm min} \lesssim 300$ kyr for $\langle P_0 \rangle = 120$ms. This constraint is not strong, because such a large value of $T_{\rm min}$ is already disfavored by the observations of Monogem (110 kyr) and Geminga (340 kyr). On the other hand, for $\langle P_0 \rangle = 300$ms, we can constrain $T_{\rm min} \lesssim 70$ kyr.

In Fig. 2.4 (bottom), we show model predictions for the expected number of TeV halos in the 2HWC catalog that have radio beams aligned with Earth, compared with the age distribution of these TeV halo candidates. We first focus on middle-aged pulsars (>100 kyr). The $\langle P_0 \rangle = 50$ ms model predicts ∼9 sources, which slightly exceeds the number of TeV halo candidate systems identified in Linden et al. (2017). This model is allowed, but if future observations rule out the TeV halo nature of several of these systems, it would be in tension with the data.

On the other hand, models with $\langle P_0 \rangle = 300$ ms produce $\lesssim 1$ middle-aged TeV halo with a radio beam directed towards Earth, which approximately saturates the lower limit produced by the identification of Monogem. This model is allowed, but if future observations confirm the TeV halo origin of candidate sources, it would be disfavored. Intriguingly, though we adopted models with $\langle P_0 \rangle = 50$ ms and $\langle P_0 \rangle = 300$ ms based on previous pulsar studies (Faucher-Giguère & Kaspi, 2006; Watters & Romani, 2011), they coincidentally also serve as reasonable estimates for the largest and smallest values allowed by the 2HWC data. The firm interpretation of existing 2HWC observations could potentially rule out either model.

We additionally show an intermediate case, with $\langle P_0 \rangle = 120$ ms, which predicts the observation of ~ 2 middle-aged TeV halos with radio beams oriented towards Earth. This model matches current observations well, and is likely remain consistent regardless of the interpretation of the 2HWC candidate sources.

Expanding our analysis to include all TeV halos with aligned radio beams regardless of the TeV halo age (including young sources), we find that the interpretations become trickier because models predict fairly similar TeV halo number counts. Models with $\langle P_0 \rangle = 300$ ms produce ~ 3 TeV halos in case that $T_{\rm min} = 0$. Meanwhile, models with $\langle P_0 \rangle = 50$ ms predict approximately ∼15 sources for $T_{\rm min} = 50$ kyr. Our intermediate model with $\langle P_0 \rangle = 120$ ms also predicts the observation of ∼15 sources for $T_{\rm min} = 0$. However, the age distribution of observed TeV halos differs markedly between models with and without a firm value of $T_{\rm min}$. Thus, future observations that correlate TeV halo activity with pulsars of known ages can more clearly distinguish between models of TeV halo formation, even in light of degeneracies between $\langle P_0 \rangle$ and $T_{\rm min}$.

In Fig. 2.5, we show the cumulative flux distribution of all TeV halos within the HAWC field of view. The 50-ms model with no $T_{\rm min}$ produces ∼20 sources that have γ-ray fluxes larger than that of Geminga, while the 2HWC catalogue contains 5–12 such potential sources (depending on source extension), so the prediction is somewhat too high. Furthermore, this model predicts a few sources that are at least an order of magnitude brighter than Geminga, while no such source is reported, so the prediction is again somewhat too high, though consistent with Poisson fluctuations. Therefore, while this model is not ruled out by the flux distribution, it is in slight tension. All of the other models are consistent with data.

Due to the steep slope at the bright end of the luminosity function (Fig. 2.3), nearby sources are expected to dominate the source count. Indeed, in our estimate, about 50% of observable sources are located within $\simeq 3$ kpc from Earth. This suggests that many observed TeV halos might have large angular sizes, indicating the importance of HAWC, which is suited for detecting extended sources.

2.4.2 Diffuse TeV Gamma-Ray Emission Measurements with Milagro

Milagro measured the diffuse Galactic γ-ray flux above 3.5 TeV, finding $\phi(>3.5\ \mathrm{TeV}) = (6.8\pm1.5\pm2.2)\times10^{-11}\ \mathrm{cm}^{-2}\ \mathrm{s}^{-1}\ \mathrm{sr}^{-1}$ within a region spanning $40^\circ < l < 100^\circ$ and $|b| < 5^\circ$ (Atkins et al., 2005). We constrain our model by requiring that unresolved TeV halos do not overproduce this flux. Due to the hard TeV halo spectrum, alternative diffuse emission measurements at lower energies by ARGO-YBJ (Bartoli et al., 2015) or a higher energy in a smaller region analyzed by Milagro (Abdo et al., 2008) give comparable constraints.

To estimate the contribution from TeV halos to this emission, we include contributions from unresolved TeV halos with fluxes below that of Geminga. We also include the contribution from electrons and positrons that escape from unresolved TeV halos and provide a diffuse emission component that fills the interstellar medium. We remove contributions from any individual halo with a γ-ray flux exceeding Geminga because such a source would be detected by Milagro (Linden & Buckman, 2018). Because the number of such sources is small ($\sim$1 or fewer) and particles lose a significant fraction of their energy in the halo region, their contribution to the diffuse emission is not important. This treatment also allows us to remove unrealistically bright individual halos predicted for the $T_{\rm min} = 0$ model, as seen in Fig. 2.3.

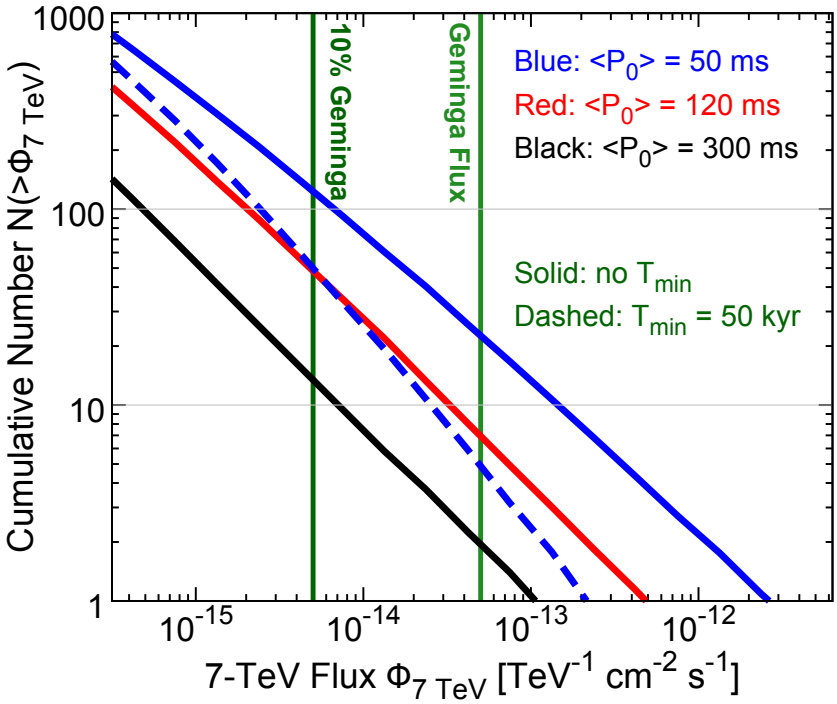

Figure 2.5. Cumulative number distribution of the differential γ-ray flux at an energy of 7 TeV for all TeV halos within the HAWC field of view, as labeled. The 2HWC sensitivity is approximately equal to 10% of the Geminga flux.

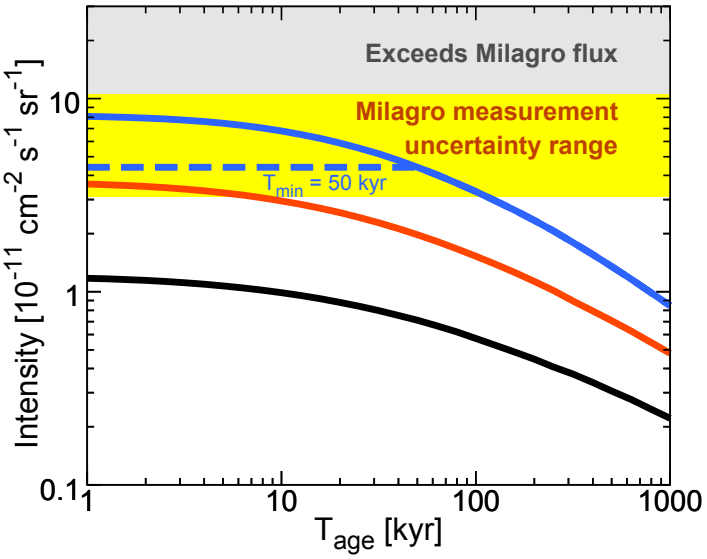

Figure 2.6. Cumulative contribution to the diffuse Galactic γ-ray flux from unresolved TeV halos with ages above $T_{\rm age}$, compared to the measurement by Milagro above 3.5 TeV. Solid unmarked curves have $T_{\rm min} = 0$. Line colors have same meaning as Fig. 2.4.

Note that we show our model predictions in cumulative contributions from pulsars above 1 kyr. Thus, the results for $T_{\rm min} = 0$ are identical for any model $T_{\rm min} \leq 1$ kyr, and are not affected by these unrealistically bright halos that only occur for $T_{\rm min} \simeq 0$. We have verified that the number of sources that contribute is large enough that the result is not subject to statistical fluctuations.

In Fig. 2.6, we show that the current diffuse measurement does not strongly constrain our models. However, we stress that having a more precise measurement in the future could provide complementary constraints to future source surveys.

The diffuse TeV γ-rays are particularly important, because, as first shown in Prodanović et al. (2007), the Milagro measurements (Atkins et al., 2005) of the diffuse flux from the Milky Way plane is significantly higher than expected from extrapolations of the GeV data (the "TeV excess"). In Linden & Buckman (2018), it was shown that TeV halos could provide an explanation of this long-standing mystery. Our results also show that unresolved TeV halos could significantly contribute to the diffuse TeV γ-ray flux. We note that the diffuse emission is dominated by bright sources (Fig. 2.3). The predicted contribution for $\langle P_0 \rangle = 300$ ms is smaller than that estimated by Linden & Buckman (2018), which adopted a harder electron spectrum of $\alpha = 1.7$ and $E_{\rm cut} = 100$ TeV. In other words, a better determination of the average electron injection spectrum could increase the predicted flux from unresolved TeV halos, producing tighter constraints on $\langle P_0 \rangle$ and $T_{\rm min}$. Interestingly, in the case of $\langle P_0 \rangle = 50$ ms or 120 ms, unresolved TeV halos can explain a significant fraction of the Milagro diffuse data without changing the spectral shape from that of our best-fit Geminga model.

2.4.3 Summary of Allowed Models and Uncertainties

Our results are primarily affected by the P_0 distribution, and the 2HWC source count allows us to constrain 50 ms $\lesssim \langle P_0 \rangle \lesssim$ 300 ms. Both the 50-ms and 300-ms models are barely allowed, and further investigations of TeV halo candidates will place stronger constraints on $\langle P_0 \rangle$. This indicates that TeV halo observations can provide an important new probe of the P_0 distribution, which is difficult to constrain by pulsar statistics.

2HWC data require $T_{\rm min} \gtrsim 50$ kyr for $\langle P_0 \rangle = 50$ ms and $T_{\rm min} \lesssim 70$ kyr for $\langle P_0 \rangle = 300$ ms. The value of $T_{\rm min}$ is not well constrained for $\langle P_0 \rangle \gtrsim$120 ms, but the firm identification of TeV halos around Geminga and Monogem suggest $T_{\rm min} \lesssim$100–300 kyr. Further observations are needed to better constrain this parameter. We stress that 50 kyr is not a strict minimum age for a TeV halo. Rather, we found that, operating under the assumption that the initial spin period of pulsars has an average $\langle P_0 \rangle = 50$ ms, this minimum age was required to ensure that the TeV halo number was consistent with data. However, the true initial period may have a larger mean, which would eliminate the need for such a cutoff. Alternatively, there may be significant variations between individual objects that are not taken into account in this model. Furthermore, our calculations have several uncertainties noted below, which could relieve the constraint on $T_{\rm min}$ for the $\langle P_0 \rangle = 50$ ms model.

We have fixed the distribution of B_0 to follow a lognormal distribution with $\langle \log_{10} B_0 \rangle = 12.65$ and $\sigma_{\log_{10} B_0} = 0.55$. Other studies that examined the magnetic field evolution of pulsars find best-fit mean values that are about 2–4 times larger (Popov et al., 2010; Gullón et al., 2014). In these models, the larger magnetic field causes pulsars to spin down faster, producing a smaller spin-down power for pulsars with ages exceeding ∼1 kyr. Adopting an alternative model with $\langle \log_{10} B_0 \rangle = 13.10$ and $\sigma_{\log_{10} B_0} = 0.65$ as derived in Gullón et al. (2014), we find the predicted number of detectable TeV halos are reduced by a factor of ∼ 2. This increases the tension between $\langle P_0 \rangle = 300$ ms and current HAWC observations, but relieves some tension between $\langle P_0 \rangle = 50$ ms and the HAWC data. In particular, for these stronger magnetic fields, $\langle P_0 \rangle = 50$ ms models become consistent with HAWC upper limits for much smaller values of $T_{\rm min} \gtrsim$10 kyr. Further examinations of the B_0 distribution will also be important for the study of TeV halo populations.

We also note that throughout this section we focus on "Geminga-like" TeV halos. We can also adopt different models to take into account deviations from this assumption. We first study the effect of variations in the γ-ray efficiencies. There might be nearly an order of magnitude variation among individual sources, as noted in Sec. 2.2. The primary effect of such a dispersion would be to smooth out the falling number-count distribution (Fig 2.3), and increase the number of detectable sources. We examine alternative models where γ-ray fluxes are multiplied by a factor of 10^x, where x is a random variable drawn from a normal distribution with mean 0 and variance 1. We find that the number of detectable sources is increased by a factor of ∼2. In this case, $\langle P_0 \rangle = 50$ ms model would require $T_{\rm min}$ to be significantly larger than 100 kyr, inconsistent with TeV halo observations around Monogem. Further studies of the variation between sources are necessary to better quantify this point.

Finally, we study the possibility that pulsars younger than $T_{\rm min}$ produce TeV halos with different properties. In particular, at early ages, TeV halos may have smaller γ-ray efficiencies,

Table 2.2. The most important uncertainties in the number of TeV halos that are discussed in this work. For each uncertainty, we note an alternative model, and roughly indicate the effect that such a model would have on the predicted TeV halo source count.

Name of Uncertainty	Default	Alternative	Effect
pulsar population			
P_0 distribution	Gaussian	Uniform	**increase**, $\times 2$
B_0 distribution	$\langle \log_{10} B_0 \rangle = 12.65$	$\langle \log_{10} B_0 \rangle = 13.10$	**decrease**, $\times 0.5$
γ-ray efficiency			
$\dot{E}$ dependence	$L_\gamma \propto \dot{E}$	$L_\gamma \propto \dot{E}^{0.8}$	**decrease**, $\times 0.5$
		$L_\gamma \propto \dot{E}^{1.2}$	**increase**, $\times 2$
age dependence	$L_\gamma/\dot{E} = \text{const.}$	$L_\gamma/\dot{E} \propto (T_{\rm age})^{0.5}$	**decrease**, $\times 0.3$
		$L_\gamma/\dot{E} \propto (T_{\rm age})^{-0.5}$	**increase**, $\times 3$
source-to-source scatter	none	$\log_{10}(L_\gamma/\dot{E}) \sim N(1, 0.5^2)$ (lognormal, $\sigma = 0.5$)	**increase**, $\times 2$

because most of the injected energy should be lost to synchrotron emission and there may be less particle energy escaping into the TeV halos, as discussed in Sec. 2.2. Throughout this work, this effect is simply treated by sharply cutting off contributions from pulsars younger than $T_{\rm min}$, but one could alternatively assume a smooth changes in the γ-ray efficiencies. This could lead to a detectable population that does not exceed 2HWC constraints. To be more quantitative on this point, we examine alternative models where the γ-ray fluxes are smoothly reduced by a factor of $(T_{\rm age}/340\ {\rm kyr})^\beta$ for pulsars younger than Geminga. This replaces the sharp cutoff ($T_{\rm min}$) in our standard formalism. We find that the $\langle P_0 \rangle = 50$ ms model does not produce too many TeV halos for $\beta \gtrsim 0.7$. Further studies are needed to more thoroughly examine this parameter space.

In Table 2.2, we show each major uncertainty, mention an alternative model, and roughly indicate the net effect of this model on the predicted number of TeV halo sources. In addition to models mentioned above, we further test several different scenarios, which are explained in Appendix A.2. The exact effect of different uncertainties depends on the standard model that we use for comparison, so we adopt a constant default model of $\langle P_0 \rangle = 120$ ms and $T_{\rm min} = 10$ kyr in all cases, and show their age dependence in Fig. A.2 in Appendix A.2.

All of the uncertainties noted above could change the number of detectable sources by a factor of $\sim$2. While these changes are important, they are subdominant to the effect of variations in the P_0 distribution, and support our assertion that the P_0 distribution dominates the uncertainty in our models. Note that different B_0 distributions may lead to smaller number counts, while source variations may increase the number of detectable systems, implying that our default case occupies a reasonable middle value. More TeV halo observations would allow us to better examine these models, and place stronger constraints on pulsar properties.

2.5 Future Directions

Upcoming surveys have great power to detect TeV halos. In Sec. 2.5.1, we quantitatively assess the prospects for Galactic source searches with HAWC and CTA. In Sec. 2.5.2, we do the same for extragalactic searches with CTA. In Sec. 2.5.3, we show that detailed morphological studies of existing H.E.S.S. sources could potentially identify many TeV halos.

2.5.1 Extended Source Survey with HAWC and CTA

We begin by outlining methods to identify TeV halos. One straightforward way to claim that TeV emission is powered by a pulsar is to detect the radio beam from the pulsed emission or to find a compact PWN at the center of the γ-ray source. We may also detect a TeV halo component in a composite (TeV halo + PWN) system by examining if its γ-ray emission can be fit by two morphological components rather than one. In the case of bow-shock pulsars, we can more clearly discriminate TeV halos from PWN, whose size is clearly determined by the stand-off radius (Bykov et al., 2017).

In some cases we may be able to detect extended emission around PWNe in other wavelengths, from synchrotron radiation produced by the same electrons and positrons that escape the compact PWN and produce TeV halo emission. Interestingly, Uchiyama et al. (2009) and Bamba et al. (2010) potentially detected such emission in X-rays, suggesting the potential for identifying TeV halos in multi-wavelength observations.

In Fig. 2.7, we show expectations for the TeV halo population that could be uncovered by HAWC observations. We assume a 10-yr sensitivity that is improved by a factor of $\sqrt{5}$ compared to the quoted sensitivity of the 2HWC catalog, following the same declination dependence. This corresponds to a sensitivity that is approximately 4% of the Geminga flux for sources residing in optimal sky positions. These predictions are conservative, because HAWC has recently installed an upgrade and increased the instrumented area (Joshi et al., 2017), an effect which is not included in our calculation.

The 10-yr HAWC survey promises to discover a significant TeV halo population. Even in the pessimistic case of $\langle P_0 \rangle = 300$ ms, we expect that $\sim$20 sources (including 4 already found) will be detected for $T_{\rm min} = 0$. In the most optimistic case (e.g., $\langle P_0 \rangle = 50$ ms and $T_{\rm min} = 50$ kyr), HAWC would be expected to detect $\sim$80 TeV halos. We note that these cases are nearly ruled out by existing TeV halo observations (Sec. 2.4.1). Our intermediate case ($\langle P_0 \rangle = 120$ ms) predicts $\sim$70 sources if $T_{\rm min} = 0$, though this model prediction is only barely allowed from the 2HWC source count (see Fig 2.4). Such a large number of sources would allow us to significantly improve our constraints on the spectral, morphological, and evolutionary properties of TeV halos.

We stress that our predictions are based on the Geminga-like assumption provided in Eq. (2.3), combined with standard models of pulsar population synthesis established by previous studies (e.g., Faucher-Giguère & Kaspi, 2006; Bates et al., 2014). If HAWC detects a significantly smaller number of TeV halos, it would indicate that Eq. (2.3) cannot be applied to all pulsars, and that the observed Geminga-like halos must have unusually large TeV γ-ray efficiencies. Conversely, if significantly more sources are observed than predicted, it would indicate that observed sources have relatively dim halos, compared to the average population. Either result would substantially enhance our understanding of these systems.

In Fig. 2.8, we show our prediction for the Galactic longitude distribution of detected TeV halos (top) and the diffuse flux from unresolved TeV halos (bottom) for our intermediate case of $\langle P_0 \rangle = 120$ ms. In addition to 10-yr HAWC observations, we make a prediction for hypothetical HAWC-like telescope that uniformly observes the sky with a sensitivity that is 3% of the Geminga flux. We also show the predicted contribution from TeV halos

to the Milagro diffuse measurement, which probed the region within $30° < l < 110°$ and $136° < l < 216°$ (Atkins et al., 2005; Abdo et al., 2008), and also to the HAWC diffuse measurement, for the region that falls fairly within the field of view. The source count (top panel) shows the sizeable impact of a HAWC-like water Cherenkov telescope at the Southern hemisphere, like the Southern Gamma-Ray Survey Observatory (Mostafa & HAWC Collaboration, 2017; Schoorlemmer et al., 2017; Mostafa et al., 2017); it would allow us to probe a region at the edge or outside the HAWC field of view, where we expect a significant number of detectable TeV halos. It also demonstrates that the effect of source confusion is not large; we expect at most ∼4 sources over $\Delta l = 5°$, which means that the typical intersource spacing is large compared to the angular resolution ($\sim 0.1°$ in radius) and the typical source size (also $\sim 0.1°$ with significant variations).

In Fig. 2.8 (bottom), we show that HAWC measurements will greatly improve our understanding of the diffuse TeV flux. In particular, in the region of $40° < l < 100°$, where the diffuse TeV excess was first identified, our predictions indicate that more than half of the diffuse emission from TeV halos will be resolved into individual sources by future HAWC

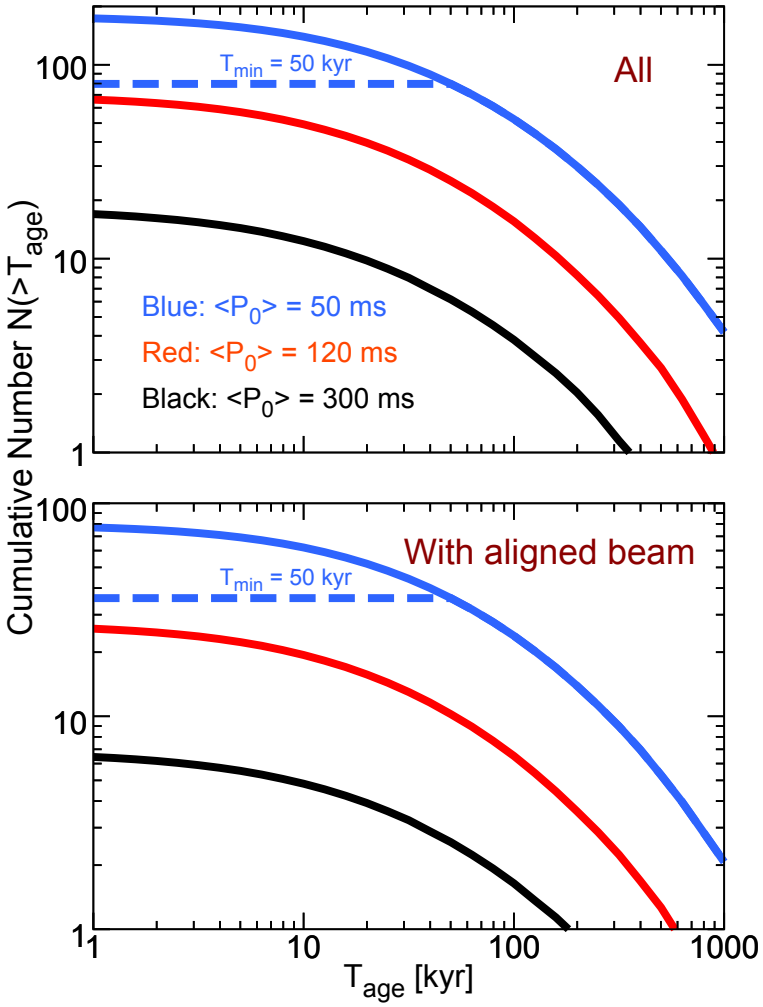

Figure 2.7. Same as Fig. 2.4, but using 10 years of HAWC observations. Solid unmarked curves have $T_{\rm min} = 0$.

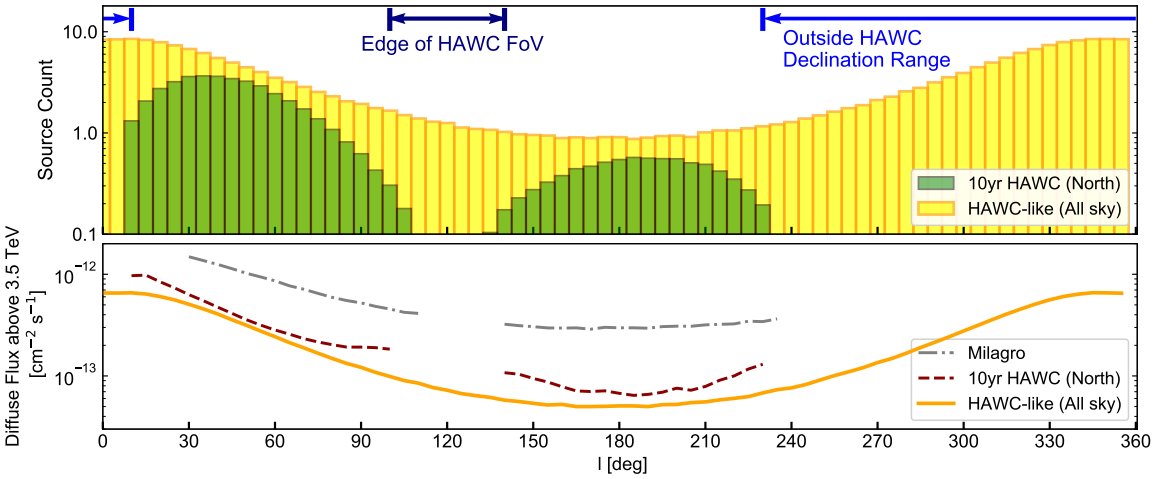

Figure 2.8. The prediction for the Galactic latitude distribution of the TeV halo number (top) and the diffuse γ-ray flux from unresolved TeV halos (bottom) from $|b| < 5^\circ$ in bins of $\Delta l = 5^\circ$. All results utilize a model with $\langle P_0 \rangle = 120$ ms and $T_{\rm min} = 1$ kyr. A "HAWC-like" 10 year sensitivity is modeled as a theoretical instrument with a sensitivity of 3% of the Geminga flux across the entire sky.

surveys. Apart from shedding light on the nature of the diffuse TeV emission, this would also put constraints on the population of unresolved sources that contribute to the remaining diffuse flux.

We also make a prediction for the future Galactic Plane survey with CTA (Acharya et al., 2017). We assume that CTA will observe from $l = 0^\circ$ to 360° and $|b| < 3^\circ$ with a sensitivity of 3 mCrab, where 1 Crab is defined as a γ-ray flux above 1 TeV of 2.26×10^{-11} cm^{-2}s^{-1}, and 3 mCrab corresponds to 2% of the Geminga flux (defined as $F^{\mathcal{G}}_{\rm TeV}$ in Sec. 2.3). We assume a PSF size of $\theta_{\rm PSF} = 0.05^\circ$ to take into account the degradation of the sensitivity for extended sources. Because the PSF of CTA is smaller, this effect is more important compared to HAWC observations.

Even in the pessimistic case of $\langle P_0 \rangle = 300$ ms, we predict that ~30 TeV halos could be detected. In the case of $\langle P_0 \rangle = 50$ ms with $T_{\rm min} = 50$ kyr, we predict that about 160 TeV halos could be detected. Our intermediate model, $\langle P_0 \rangle = 120$ ms, also predicts ~150 for $T_{\rm min} = 0$. These detections will be highly complementary to HAWC observations. HAWC is located in the Northern hemisphere, while CTA is expected have better sensitivity in the Southern hemisphere. Moreover, while HAWC is suited for spatially extended sources, CTA can find more distant and dimmer sources. In our prediction for HAWC, the 10–90% containment fraction of TeV halo distances corresponds to roughly 1–10 kpc. In contrast, for CTA, the 10–90% containment window spans from 3–15 kpc. Together, these observations can map out much of the Galaxy in TeV halos. This also indicates that another water Cherenkov telescope at the Southern hemisphere would be critical for detecting nearby sources throughout the Galactic Plane.

2.5.2 Extragalactic Survey with CTA

Milky Way TeV halo searches must deal with large angular source size and distance uncertainties. One way to avoid these issues is to search for extragalactic sources. A good target is the Large Magellanic Cloud (LMC), which is nearby and face-on, and which will also be extensively observed by the CTA as part of its Key Scientific Program (Acharya et al., 2017). CTA observations are expected to achieve an integrated energy flux sensitivity of 3 $\times$ 10^{-14} erg cm^{-2} s^{-1} above 1 TeV. The collaboration expects to uncover $\sim$10 sources that are primarily SNRs, without including TeV halos.

We estimate the number of TeV halos that can be detected in the Large Magellanic Cloud (LMC) by the CTA survey. We adopt a standard distance of 50 kpc, and count the number of halos with luminosities exceeding 9 $\times$ 10^{33} erg s^{-1} above 1 TeV. The birth rate of pulsars in the LMC is normalized to be 0.005 yr^{-1}, which is the lower value obtained by a previous study of LMC pulsar population modelling (Ridley & Lorimer, 2010). Though the interstellar infrared radiation field in the LMC is weaker compared to the Milky Way (Israel et al., 2010), the predicted TeV halo flux is reduced only by a factor of 1.3 even if we set $\rho_{\rm IR} = 0$, due to the contribution from the cosmic microwave background photons. Since this modification is degenerate with a number of uncertainties, we do not take this into account in what follows.

In Fig. 2.9, we show that CTA will likely detect at least $\sim$1, and potentially $\sim$30, extragalactic TeV halos in the LMC, substantially increasing the total number of sources detected with this survey. These observations will provide more important information than the source count alone, shedding insight into the brightest TeV halos in a region without significant distance uncertainties. Thus, CTA observations will provide complementary constraints to HAWC Milky Way observations. The differentiation of extragalactic TeV halos from PWNe will be challenging, because both will appear pointlike even with the unparalleled angular resolution of CTA. The best path forward will be to employ followup radio observations of

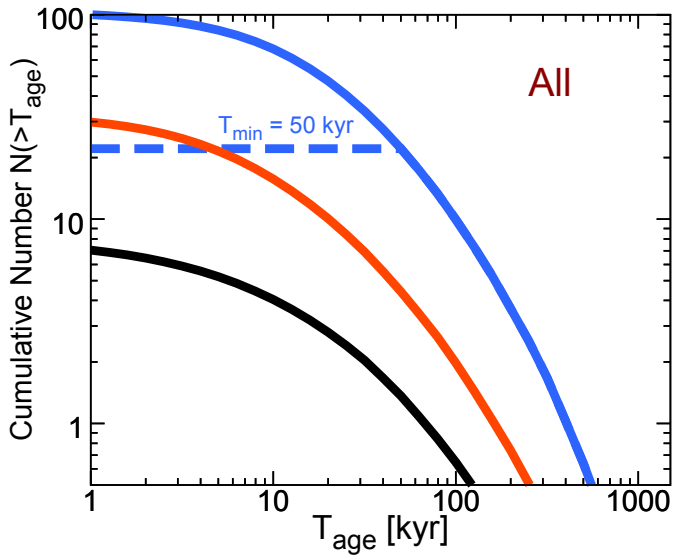

Figure 2.9. Same as the upper panel of Fig. 2.7, but for the LMC survey with CTA. Curves have $T_{\rm min} = 0$ unless marked.

synchrotron counterparts to further examine the emission morphology. Because the size of halos are poorly understood, there may also be a possibility that we could observe TeV halos extended beyond a radius of ~ 100 pc, which could be detected as extended sources even in the LMC.

We note that the observed radio pulsars in the LMC appear to have a strikingly different distribution of spindown powers compared to expectations from pulsar evolution (Fig. 2.3). In particular, current observations detect two very bright ($\dot{E} > 10^{38}$ erg s^{-1}) pulsars, while the 11 other detected pulsars have low $\dot{E}$ ($\dot{E} < 6 \times 10^{34}$ erg s^{-1}). There are no pulsars in between these ranges (Manchester et al., 2005). This is most likely due to the combination of selection effects, weak correlations between $\dot{E}$ and radio luminosity (Szary et al., 2014a), and the randomness of pulse radiation beamed toward us. Future pulsar surveys may enable us to better examine the pulsar population in the LMC. Since TeV halo emissions are expected to be more isotropic and may better correlate with $\dot{E}$ than radio pulse emissions, they could provide complementary information regarding the population of bright pulsars, potentially resolving this tension, or confirming it. In the latter case, it would demand significant modifications to the theory of pulsar formation and evolution.

Finally, we note that we might also be able to observe a similar number of TeV halos in the Small Magellanic Cloud, because it has a distance and pulsar formation rate comparable to the LMC (Ridley & Lorimer, 2010). This would potentially provide information regarding the evolution of TeV halos in low metallicity environments.

2.5.3 Followup Study for H.E.S.S. Sources

So far, we have focused on the existing survey catalog by HAWC, which is suited for extended source surveys. However, existing source catalogs from imaging air Cherenkov telescopes should also contain as-yet identified TeV halos.

Here we focus on the H.E.S.S. Galactic Plane Survey (HGPS) catalog, which has detected 78 sources in total, 42 of which are associated with ATNF pulsars (Abdalla et al., 2018a). Five of these tentative pulsar associations are known to be either an SNR or a binary, as well as the Arc and Galactic Center, while the remaining 37 sources are categorized as firmly identified PWN (including composite system), candidate PWN, or unidentified sources. We examine how many of these sources could be interpreted as TeV halos.

We make a prediction following the methodology for the CTA Galactic Plane survey in Sec. 2.5.1. We include sources between Galactic longitudes spanning from $l = 250°$ to $65°$ and latitude $|b| < 3°$. The sensitivity of HGPS is non-uniform across the Galactic Plane. Since our goal is not to make precise estimates of the H.E.S.S. sensitivity, we simply assume a sensitivity of 1% Crab for point sources and utilize a PSF of $\theta_{\rm PSF} = 0.08°$. We further assume that any source of $\theta_{\rm size} > 0.7°$ is not observed, because HGPS is not able to detect such an extended source. This removes the contribution from any halos within about 700 pc of Earth.

In Fig. 2.10 (top), we show that 10–50 sources in the HGPS catalog could be TeV halos. This indicates that detailed morphological studies of HGPS sources could uncover many TeV halos in this catalog. The definitive identification of these sources would be important in constraining particle transport due to the unparalleled angular resolution of H.E.S.S..

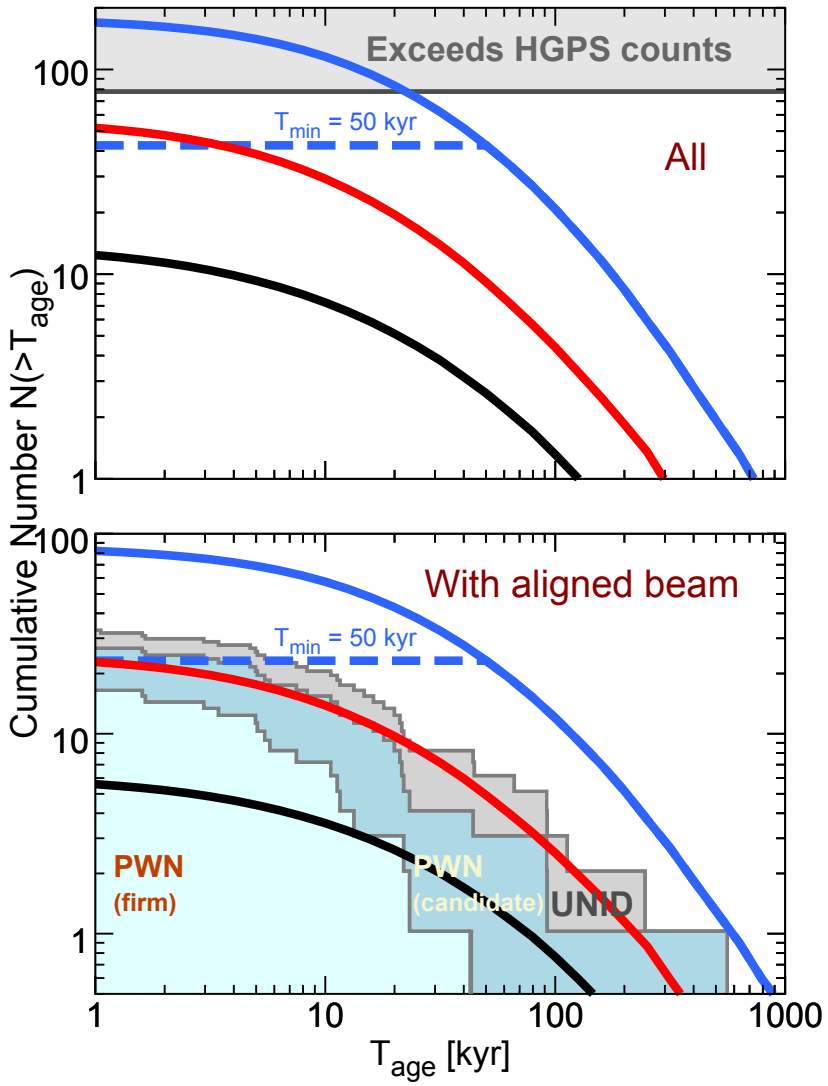

Figure 2.10. Same as Fig. 2.4, but for the H.E.S.S. Galactic Plane Survey (HGPS). In the bottom panel, the histogram of HGPS sources associated with ATNF pulsars is also shown, divided into three classes following Abdalla et al. (2018a,b). Note that from all unidentified sources in HGPS we only plot those associated with radio pulsars.

In Fig. 2.10 (bottom), we compare the predicted number of TeV halos to the observed number of radio pulsar associations. Our model predicts that, among the 37 sources associated with ATNF pulsars, ∼6–20 sources could be TeV halos. Interestingly, the shape of our predicted age distribution matches observed data well. Because our predictions are based on the assumption that the γ-ray flux is proportional to $\dot{E}$, this agreement suggests that these HGPS sources are powered by pulsar activity, either PWNe or TeV halos, rather than SNR.

2.6 Conclusions

TeV halos are a new class of γ-ray sources (Linden et al., 2017; Abdo et al., 2009b; Abeysekara et al., 2017a; Aharonian et al., 1997; Yüksel et al., 2009; Linden & Buckman, 2018; Hooper et al., 2018; Evoli et al., 2018; Hooper & Linden, 2018c; Riviere et al., 2017; Brisbois et al.,

2018). They are bright, have hard spectra, and are spatially extended. They are powered by electrons and positrons that escaped from the PWNe, but which remain confined in a region where diffusion is strongly suppressed. Empirical arguments suggest TeV halos are common around pulsars. However, among many candidate sources, only four TeV halos have been confirmed so far. The rest are likely undetected due to the diminishing sensitivity of TeV instruments to extended γ-ray sources.

In this work, for the first time, we theoretically quantify the role of future surveys to detect more TeV halos. We also study new implications for pulsar physics and existing γ-ray sources. We use standard methods for pulsar population synthesis and focus on a model where the TeV halo luminosity is calculated based on Geminga observations. Our analysis produced three main results.

- **TeV halos could be the most important source class in future TeV γ-ray surveys.** We predict, utilizing the range of models that are consistent with current datasets, that HAWC will eventually detect $\sim$20–80 TeV halos, and future Galactic surveys by CTA will also find $\sim$30–160 halos. Further, CTA can potentially detect $\sim$10 TeV halos in the LMC and SMC. This indicates that TeV halos could be the dominant source class in the TeV γ-ray sky. Such a large number of sources would allow us to examine their properties and evolution in great detail.
- **Further studies of unidentified TeV sources and "TeV PWN" are needed.** We find that the HGPS catalog might contain $\sim$10–50 TeV halos, which are currently classified as either unidentified sources or PWNe. These results have three implications. First, imaging air Cherenkov telescopes like H.E.S.S., MAGIC and VERITAS can also play an important role in studying TeV halos. In particular, their high angular resolution would be critical in examining particle transport inside the halo. Second, it might be important for modelling of "TeV PWN" to take into account the emission from TeV halo regions. Third, X-ray and radio observations of "TeV PWN" may find many extended halos around compact PWNe. This synchrotron emission counterpart could help to identify TeV halos.
- **TeV halos observations can constrain pulsar properties.** Our predictions are primarily affected by the distribution of the initial spindown period, which is not well constrained by pulsar population studies. In other words, TeV halo observations can provide complementary constraints to existing radio surveys. Current 2HWC data allow 50 ms $\lesssim \langle P_0 \rangle \lesssim$ 300 ms, and further studies will place tighter constraints.

We finally note that TeV halo observations may unlock new opportunities to study astrophysics.

- TeV halo observations would allow us to detect pulsars with radio emission not aligned toward Earth and hence which have been missed in previous blind searches (Linden et al., 2017). Further, the angular size of halos could provide useful distance estimations for Galactic pulsars. Thus, many observations of TeV halos could allow us to map out pulsars in the Galaxy, including misaligned systems. This new method would work as an independent and complementary method compared to radio observations. In this regard, the Southern Gamma-Ray Survey Observatory would play an important role in

detecting TeV halos across the Galactic Plane, especially in the inner Galaxy. In addition, next-generation telescopes like LHASSO (Di Sciascio & LHAASO Collaboration, 2016) can find more TeV halos.

- TeV halo observations would substantially improve our understanding of total galactic γ-ray emission. Usually, galactic γ-ray emission is assumed to be dominated by hadronic processes induced by diffusing protons and nuclei, especially in the GeV energy range. The bright and hard-spectrum emission from TeV halos suggests that leptonic emission mechanisms may be important for the diffuse emission in the TeV energy range. This has two implications for the cosmic background emission. First, the hard spectrum of TeV halo emission might make ordinary galaxies more important for TeV γ-ray background than expected only from hadronic emission, which falls off steeply. Second, the leptonic nature of TeV halo emission may make star-forming galaxies less important for the TeV neutrino background than expected from the assumption that all TeV galactic γ-ray emission is hadronic. In particular, predicting neutrino flux from galaxies by simply extrapolating their γ-ray flux could result in a substantial overestimate.
- TeV halos could help pinpoint the sources of IceCube neutrinos in our Galaxy. A promising way to search for neutrino emitters is to look into γ-ray source catalogs. However, if most γ-ray sources are TeV halos, there is less room for hadronic sources. This has both positive and negative implications for neutrino astronomy. It is unfortunate, since we can only expect high-energy neutrinos from a small fraction of identifiable γ-ray sources. On the other hand, if we can identify TeV halos in γ-ray source catalogs, we can ignore their neutrino contributions and reduce the trials factor in IceCube neutrino cross-correlations.
- Existing TeV halo observations indicate that pulsars contribute to the cosmic-ray electron and positron flux. However, future observations are necessary to understand the exact degree they contribute, which classes of systems are important, and the constraints which can be put on residual contributions by exotic physics such as dark matter annihilation. In particular, follow up observations of TeV halos with GeV γ-rays and other wavelengths can provide important complementary information capable of constraining the pulsar contribution to the positron excess, which is seen in GeV energy range.

2.7 Note Added

At the time this work was carried out, 2HWC was the latest source catalog published by HAWC. Very recently, HAWC released a new catalog, 3HWC, which makes use of 1523 days of data and reports 65 sources (Albert et al., 2020). Detailed investigation of these sources are still ongoing, and results from this new catalog does not modify our discussion presented in this Chapter at this point. However, it is intriguing to note that they identified eight old (>100 kyr) pulsars that are potentially associated with TeV halos. If these associations are confirmed, it may start to constrain models of the pulsar initial spin.

The existence of extended halo around Geminga has been also confirmed in the GeV band

(Di Mauro et al., 2019). The GeV counterpart is even more extended than the TeV halo, likely due to the longer cooling time of GeV electrons.

The interpretation of extended "TeV PWN" and the connection to TeV halos still remain under debate. In particular, while Geminga, Monogem, and several other relatively old pulsars exhibit a halo feature that are clearly distinct from the PWN, much remain unknown for younger systems. On one hand, Giacinti et al. (2020) argued that halos can be formed only around old pulsars that have already escaped from the parent SNR and that particles in the halo should not dominate the energetics. They thus argued that the contributions of TeV halos to the source counts and diffuse Galactic emission should be small. On the other hand, Di Mauro et al. (2020) analyzed the H.E.S.S. data and argued that many TeV sources associated with young pulsars have similar morphological feature that can be interpreted as halos. They further estimated the number of TeV halos detected by H.E.S.S., HAWC and CTA, and reached similar conclusions to ours.

In our work, we have defined TeV halos in maximally observation-based way. Our analysis have quantified the power of future observations to detect TeV halos, allowing us to study the properties and evolution of PWNe and TeV halos.

Chapter 3

Radio-SFR Correlation Modified by Millisecond Pulsars

This chapter is based on the paper "Millisecond Pulsars Modify the Radio-SFR Correlation in Quiescent Galaxies" by Sudoh T., Linden T., Beacom J. F., (2020), preprint (arXiv:2005.08982)

3.1 Introduction to this Chapter

The radio–far-infrared (FIR) correlation is a cornerstone in our understanding of star-formation and cosmic-ray physics. Throughout their brief lives, massive stars produce bright radiation that is absorbed by interstellar dust and re-emitted in the FIR. In their violent deaths, these stars produce shocks that accelerate charged particles to GeV and higher energies. These cosmic rays lose energy via hadronic, inverse-Compton, and synchrotron interactions, producing a bright nonthermal radio flux, among other emissions. The close correlation between nonthermal radio and FIR emission has been found over a wide range of galactic masses and star-formation rates (SFRs) (van der Kruit, 1973b,a; Harwit & Pacini, 1975; Dickey & Salpeter, 1984; Rickard & Harvey, 1984; Helou et al., 1985; de Jong et al., 1985; Hummel et al., 1988; Condon, 1992; Yun et al., 2001; Appleton et al., 2004; Jarvis et al., 2010; Magnelli et al., 2015; Qiu et al., 2017; Tabatabaei et al., 2017; Shao et al., 2018; Read et al., 2018; Filho et al., 2019; Solarz et al., 2019). A similar correlation has been found between the γ-ray and FIR fluxes, providing additional support for the cosmic-ray origin of the radio emission (Ackermann et al., 2012; Linden, 2017; Ajello et al., 2020).

The increasingly high precision of radio and infrared measurements has isolated several confounding variables, including environmental effects (Murphy et al., 2009) and active galactic nuclei (AGN) contributions (Condon et al., 2002; Morić et al., 2010), and produced resolved analyses of the radio-FIR correlation within galaxies (Beck & Golla, 1988; Murphy et al., 2006; Paladino et al., 2006; Murphy et al., 2008; Heesen et al., 2014, 2019). Intriguingly, observations have detected dispersion in the radio-FIR correlation in the least luminous star-forming galaxies (SFGs). Early studies of low-luminosity galaxies found that both the FIR (due to ineffective dust absorption) and radio (due to ineffective cosmic-ray trapping) fluxes fall below predictions based on calorimetric models (which require that both ultraviolet photons and cosmic rays lose all their energy in the galaxy), implying the breakdown of calorimetry.

Thus, a "conspiracy" of factors should exist to maintain the radio-FIR correlation over such a large dynamic range (Bell, 2003; Lacki et al., 2010).

Because the FIR flux may not always trace the SFR accurately, many studies have included optical and UV measurements to better probe the physical correlation between star formation and nonthermal emission (e.g., Hodge et al., 2008; Brown et al., 2017; Davies et al., 2017; Hindson et al., 2018; Calistro Rivera et al., 2017; Gürkan et al., 2018; Wang et al., 2019). The radio-SFR correlation is expressed as $L_{\rm r} \propto {\rm SFR}^{\alpha}$, where $L_{\rm r}$ is the radio luminosity, and α is the power-law index. Recent observations find α exceeding unity (e.g., Hodge et al., 2008; Brown et al., 2017; Davies et al., 2017; Calistro Rivera et al., 2017; Wang et al., 2019), which can be attributed to increasing cosmic-ray confinement and synchrotron radiation efficiency in rapidly star-forming systems (e.g., Niklas & Beck, 1997; Schleicher & Beck, 2016).

In these studies, the radio flux has been attributed to supernova remnants (SNRs) and normal pulsars, both of which trace recent star formation. However, recent γ-ray observations suggest that recycled, millisecond pulsars (MSPs) can efficiently convert their power to cosmic-ray electrons and positrons (Hooper & Linden, 2018c), possibly supplying additional power to the galactic nonthermal emission. Unlike SNRs and normal pulsars, MSPs first evolve through long-lived low-mass X-ray binary (LMXB) phases (Fragos et al., 2013) and then slowly spin down over $\sim$ 1–10 Gyr timescales (Corbet, 1984; Tauris & van den Heuvel, 2006). Thus, the MSP luminosity depends on the integrated SFR over the last $\sim$1–10 Gyr, and can be important for massive quiescent galaxies.

Interestingly, this result coincides with a recent observations by Gürkan et al. (2018) (hereafter, G18), which found excess radio emission in galaxies with low star-formation rates compared to expectations from the radio-SFR correlation. Splitting their galaxy catalog into two components, they found that the trend is most pronounced in galaxies with total stellar masses that exceed $10^{9.5}$ $M_{\odot}$, indicating that galaxy mass may play an important role in determining the total radio luminosity. While several effects, including contributions from AGN, pulsars, or Type-Ia SN were briefly mentioned, there is, at present, no clear explanation for this observation.

Here, we show that radio emission from MSPs may significantly contribute to (and even dominate) the radio luminosity of high-mass/low-SFR galaxies. We also produce the first quantitative fit to LOFAR data using models that include MSPs, finding that our model formally improves the fit by much greater than 5σ, though systematic errors dominate. The Chapter is outlined as follows. In Sec. 3.2, we present theoretical estimates for the radio flux from SNRs, normal pulsars, and MSPs. In Sec. 3.3, we explain our methodology for fitting the LOFAR data. In Sec. 3.4, we show the results of our analysis, and, in Sec. 3.5, we discuss the implications of our results.

3.2 Theoretical Models for Radio Emission from SNRs and MSPs

In ordinary galaxies, the dominant source of the diffuse nonthermal radio flux is due to the synchrotron emission of relativistic electrons in weak ($\sim \mu$G) galactic magnetic fields. Here we consider production within discrete sources. In Secs. 3.2.1–3.2.4, we estimate the radio emission from each source class, showing that electrons from MSPs can be important in quiescent galaxies. In Sec. 3.2.5, we discuss the conversion of this electron power into

synchrotron emission and summarize our radio emission model. In Sec. 3.2.6, we qualitatively describe the expected modification of the radio-SFR correlation by MSPs.

3.2.1 Supernova Remnants (Primary)

Core-collapse supernovae inject $\sim 10^{51}$ erg of kinetic energy into the ISM, a subdominant fraction of which (roughly $\eta_e^{\rm SN} \sim 10^{-3}$) is used to accelerate ambient electrons to relativistic energies (Tatischeff, 2009; Park et al., 2015; Sarbadhicary et al., 2017). To calculate the SNR flux in an SFG, we assume an SFR-dependent core-collapse supernova rate of 0.015ψ yr^{-1} (Lopez et al., 2018), where ψ is the galactic SFR in $M_\odot$ yr^{-1}. This produces a steady-state electron injection power of:

$$Q_e^{\rm SN,\ prim.} = 5 \times 10^{38} \psi \left(\frac{\eta_e^{\rm SN}}{10^{-3}} \right) \text{ erg s}^{-1}. \tag{3.1}$$

3.2.2 Supernova Remnants (Secondary)

SNRs also produce a significant population of nonthermal protons, which carry a much larger fraction ($\eta_p^{\rm SN} \sim 0.1$) of the supernova kinetic energy. These protons can subsequently interact with the interstellar medium to produce pions, which promptly decay to produce secondary particles, including electrons and positrons (hereafter electrons). The fraction of proton power transferred to pions is denoted f_{pp}, and depends on the mass, density, and diffusion properties of the specific galaxy. In the Milky Way, measurements of γ-ray emission indicate f_{pp} is approximately 0.03 (Strong et al., 2010).

In each collision, approximately 1/6 of the initial proton energy is converted into relativistic electrons, while the rest is converted primarily into secondary protons, neutrinos and γ-rays. Therefore, the total electron power produced via these "secondary" electrons is:

$$Q_e^{\rm SN,\ sec.} = 8 \times 10^{37} \psi \left(\frac{f_{pp}}{10^{-2}} \right) \left(\frac{\eta_p^{\rm SN}}{0.1} \right) \text{ erg s}^{-1}. \tag{3.2}$$

Thus, the conversion of SNR power to electron power has a total efficiency $\frac{1}{6}\eta_p^{\rm SN} f_{pp}$. If this exceeds $\eta_e^{\rm SN}$, then synchrotron emission from secondary electrons dominates the galactic synchrotron emission. Because $\eta_p^{\rm SN}$ is unlikely to significantly vary between galaxies, the efficiency f_{pp} determines the dominance of primary or secondary electrons. The efficiency f_{pp} is higher for galaxies that can confine cosmic rays longer, and which have higher collision rates between cosmic rays and dense interstellar gas. It is generally expected that f_{pp} eventually approaches unity (the calorimetric limit) in the strong magnetic fields and high densities of the most intensely star-forming galaxies (Thompson et al., 2007; Lacki et al., 2010).

This transition is consistent with γ-ray observations of intensely star-forming galaxies, which indicate that the γ-ray–FIR correlation exceeds unity, with $L_\gamma \propto L_{\rm IR}^{1.18}$ (Linden, 2017). This suggests that f_{pp} scales as $\sim \psi^{0.18}$. The value of f_{pp} is also estimated for nearby galaxies: it is $\sim$1% for the Small Magellanic Cloud (Lopez et al., 2018), on the order of 10% for nearby starbursts M82 and NGC253 (Lacki et al., 2011), and may reach unity for ultraluminous infrared galaxies like Arp220 (Griffin et al., 2016). This indicates that secondary electrons are generally subdominant for quiescent galaxies, but can dominate in starburst sources (Lacki et al., 2010; Lacki & Beck, 2013).

In the following, we assume a scaling between f_{pp} and ψ:

$$f_{pp} = \alpha_{pp}\psi^{\beta_{pp}}. \tag{3.3}$$

3.2.3 Normal Pulsars

Neutron stars are born as the remnants of core-collapse supernovae, with a rotational energy on the order of $10^{48}(P_0/150\text{ ms})^{-2}$ erg, where P_0 is the initial rotational period of the pulsar. Over their lifetimes, these pulsars spin down, and their rotational energy is released as a relativistic wind of magnetized e^+e^- plasma (the pulsar wind). This interacts with the ambient medium to create a shock where e^+e^- are accelerated to very high energies to produce a pulsar wind nebula (PWN). Assuming that the pulsar production rate is equivalent to the supernova rate, we obtain a steady-state electron power:

$$Q_e^{\rm PSR} = 5\times10^{37}\psi\left(\frac{P_0}{150\text{ ms}}\right)^{-2}\left(\frac{\eta_e^{\rm PSR}}{0.1}\right)\text{ erg s}^{-1}. \tag{3.4}$$

From a comparison of Eq. (3.4) to Eq. (3.1), the pulsar contribution is subdominant to the primary electron flux from supernovae. However, there are multiple uncertainties (most importantly in $\eta_e^{\rm PSR}$ and P_0) that may affect this conclusion. In particular, the average value of $(P_0)^{-2}$ is relatively unconstrained yet, which induces significant uncertainties in this estimate[*1].

It is important to note that the comparison between SNR and pulsar energetics is also energy-dependent. PWNe typically have a flat radio spectrum ($d\ln F_\nu/d\ln\nu \simeq -0.2$) (Gaensler & Slane, 2006; Reynolds et al., 2017). This indicates that radio-emitting electrons have a hard spectrum ($d\ln N_e/d\ln E_e > -2$), i.e., that most of the energy is contained in higher-energy electrons that typically radiate X-rays. In contrast, SNRs are energetically dominated by low-energy electrons ($d\ln N_e/d\ln E_e < -2$) that typically produce radio emission. Since our study focuses on LOFAR observations at 150 MHz, SNR contributions are likely more dominant in our study, compared to studies conducted at GHz frequencies. However, because we study only the integrated radio flux at a single frequency, our model cannot, in principle, differentiate these components.

Radio pulsars also directly produce pulsed and beamed radio emission. However, the fraction of the power carried by this emission is negligible, $\sim 10^{-4}$ (Szary et al., 2014b).

3.2.4 Recycled/Millisecond Pulsars (MSPs)

The time dependence of MSP cosmic-ray injection is different from every other source of galactic cosmic-rays. While emission from core-collapse SNe and normal pulsars (Eqs. 3.1, 3.2, and 3.4) depends on the current star-formation rate (ψ), MSPs first evolve through long stellar-binary and LMXB phases, and inject cosmic-rays only after a significant time lag. Moreover, MSPs continue to accelerate nonthermal electrons over a long spin-down timescale, with a spin-down power that is relatively constant over $\sim 10(P_0/5\text{ ms})^2(B_p/10^{8.5}\text{ G})^{-2}$ Gyr, where B_p is the magnetic field strength (Lorimer,

[*1] See discussions in the previous Chapter

2013; Gonthier et al., 2018). Thus, the cosmic-ray injection from MSPs traces the average star-formation rate ($\bar{\psi}$) over the last ∼10 Gyrs. Indeed, MSPs are important sources of γ-ray emission from globular clusters (Abdo et al., 2009a; Hooper & Linden, 2016) and the Galactic bulge (Gonthier et al., 2018; Macias et al., 2019), which indicates that they can power old stellar systems.

While $\bar{\psi}$ is not typically known for most galaxies, the total stellar mass (M_*) serves as an excellent tracer of star-formation over long timescales. Indeed, stellar mass is commonly employed as a tracer for the total population of low-mass X-ray binaries (LMXBs), which are the primary progenitors of MSPs (Gilfanov, 2004; Lehmer et al., 2010; Boroson et al., 2011; Fragos et al., 2013). We assume that the total power from MSPs ($Q^{\rm MSP}$) also correlates with the mass.

Because there are significant uncertainties in the transition from the LMXB to MSP phase (and thus their relative rates), we normalize the MSP population using γ-ray observations of Milky Way MSPs. Recent work by Eckner et al. (2018) attempted to address the effect of incompleteness in the observation of dim MSPs, and estimated the total luminosity of galactic MSPs to fall between $(0.5-3)\times10^{38}$ erg s^{-1}, which is consistent with previous studies (Winter et al., 2016; Ploeg et al., 2017; Bartels et al., 2018a) (see, however, Bartels et al. (2018b), which finds a smaller value). Here, we normalize the total luminosity as $L_{38}^{\rm MW} = L_{\rm MSP}^{\rm MW}/10^{38}$ erg s^{-1}. The stellar mass in the Milky Way disk is $5\times10^{10}\ M_\odot$ (Licquia & Newman, 2015), which suggests the following relation:

$$Q_{\rm total}^{\rm MSP} = 2\times10^{38} L_{38}^{\rm MW}\left(\frac{M_*}{10^{10}M_\odot}\right)\left(\frac{\eta_\gamma}{0.1}\right)^{-1}\ {\rm erg\ s^{-1}}, \tag{3.5}$$

where η_γ is the conversion efficiency from spindown power to γ-ray luminosity, estimated to be $\sim 10\%$ (Abdo et al., 2013).

These estimates do not include a contribution from galactic globular clusters, which might enhance the total γ-ray luminosity from the galaxy. We also note that the Milky Way value may not be typical. Studies of the LMXB population by Gilfanov (2004) found that, while LMXBs are expected to trace stellar mass, the LMXB population of the Milky Way is roughly 2.5 times smaller than a chosen population of nearby Milky Way analogs. In particular, morphological analyses of the M31 galactic bulge indicate that the MSP population of M31 may be up to a factor of 4 larger than expectations based on Milky Way models (Ackermann et al., 2017; Eckner et al., 2018).

The power and spectrum of electrons produced by MSPs are highly uncertain, both theoretically and observationally. As in the case of normal pulsars, a substantial relativistic electron population is accelerated within the strong electric and magnetic fields of the pulsar magnetosphere. Notably, despite magnetic field strengths that are several orders of magnitude smaller than normal pulsars, the γ-ray spectrum of MSPs and normal pulsars is almost identical, indicating that they may also accelerate similar electron populations. However, unlike normal pulsars, MSPs rarely produce bright PWNe (Stappers et al., 2003; Hui & Becker, 2006; Lee et al., 2018), and thus the relativistic electrons may not be subsequently accelerated by a termination shock. This also indicates that electron energy losses due to the adiabatic expansion of the nebula and synchrotron cooling inside it are much less important for MSPs, allowing a larger fraction of the injected power to be released into the ISM. Thus, it is likely

that the ISM electron spectrum produced by MSPs differs substantially from that produced by normal pulsars.

The conversion efficiency $\eta_e^{\rm MSP}$ is uncertain, and a wide range of values from a few percent to 90% have been tested in the literature. To date, the most stringent constraints on $\eta_e^{\rm MSP}$ come from observations at TeV scales. A recent study of the globular cluster M15 by the MAGIC collaboration suggests an efficiency less than 30% (MAGIC Collaboration, 2019) for a power-law injection, though it should be noted that frequent stellar interactions in the cluster may significantly suppress the particle production by MSPs (Cheng et al., 2010). Observational studies of TeV emission around Galactic MSPs suggests that the value of $\eta_e^{\rm MSP}$ might be ∼10% (Hooper & Linden, 2018c). Importantly, neither of these observations can strongly constrain the efficiency at the GeV scales that are most important for 150 MHz radio observations.

The lack of PWNe around MSPs makes it difficult to constrain their nonthermal electron spectra. Previous studies of nonthermal electron production in MSPs have used a diverse set of models with a wide range of parameters (Bednarek & Sitarek, 2007; Cheng et al., 2010; Harding & Muslimov, 2011; Kisaka & Kawanaka, 2012; Venter et al., 2015; Yuan & Ioka, 2015; Petrović et al., 2015; Bednarek et al., 2016; Song et al., 2019; Ndiyavala et al., 2019; Bykov et al., 2019). For our analysis, which uses radio emission at only one frequency (150 MHz), changes in the electron spectrum and the electron acceleration efficiency are degenerate. Thus, we absorb the uncertainty in the MSP spectral shape into the parameter $\eta_e^{\rm MSP}$, writing the total electron power from MSPs as

$$Q_e^{\rm MSP} = 2\times10^{37} L_{38}^{\rm MW} \left(\frac{M_*}{10^{10} M_\odot}\right) \left(\frac{\eta_e^{\rm MSP}}{\eta_\gamma}\right) \ {\rm erg\ s^{-1}}. \tag{3.6}$$

While the contribution of MSPs is sub-dominant in typical galaxies, it becomes important whenever

$$L_{38}^{\rm MW} \left(\frac{\eta_e^{\rm MSP}}{\eta_\gamma}\right) \left(\frac{M_*}{10^{10} M_\odot}\right) \left(\frac{\psi}{1\ {\rm M_\odot\ yr^{-1}}}\right)^{-1} \gtrsim 30. \tag{3.7}$$

For galaxies with low specific SFR (sSFR; SFR/Mass), the contribution of MSPs can be dominant. Intriguingly, this is the region ($M_* > 10^{9.5}$ M$_\odot$ and $\psi < 10^{-2}$ M$_\odot$ yr^{-1}) where LOFAR has identified a radio excess.

3.2.5 Modeling the Synchrotron Luminosity in SFGs

In previous subsections, we developed quantitative models for the total electron power from each source class, but thus far we have only qualitatively discussed the production of synchrotron radiation from these populations. There are three effects at play. The first is the energy dependence of the electron spectrum, which affects the fraction of the synchrotron power that is emitted at 150 MHz. The critical frequency for synchrotron radiation is given by

$$\nu_c = 80 \left(\frac{E_e}{\rm GeV}\right)^2 \left(\frac{B}{6\ \mu{\rm G}}\right) \ {\rm MHz}, \tag{3.8}$$

which indicates that GeV-scale electrons are most efficient at producing the 150 MHz radio emission studied here. The fraction of the total electron power that is stored in 150 MHz emitting electrons, χ_{150}, strongly depends on the spectrum injected by sources.

The second effect pertains to competitive electron energy-loss mechanisms, including inverse-Compton scattering, bremsstrahlung, and ionization. The relative contribution of each component can be evaluated from their cooling timescales (Atoyan et al., 1995):

$$\begin{aligned} t_{\rm syn} &= 2.6\times10^8\ {\rm yr}\ \nu_{150}^{-1/2}\left(\frac{B}{6\ \mu{\rm G}}\right)^{-3/2}, \\ t_{\rm IC} &= 2.3\times10^8\ {\rm yr}\ \nu_{150}^{-1/2}\left(\frac{B}{6\ \mu{\rm G}}\right)^{1/2}\left(\frac{w_{\rm ISRF}}{1\ {\rm eV\ cm^{-3}}}\right)^{-1}, \\ t_{\rm brems} &= 1.1\times10^8\ {\rm yr}\left(\frac{n_{\rm gas}}{0.3\ {\rm cm^{-3}}}\right)^{-1}, \\ t_{\rm ion} &= 4.8\times10^8\ {\rm yr}\ \nu_{150}^{1/2}\left(\frac{B}{6\ \mu{\rm G}}\right)^{-1/2}\left(\frac{n_{\rm gas}}{0.3\ {\rm cm^{-3}}}\right)^{-1}, \end{aligned} \tag{3.9}$$

where ν_{150} is the observation frequency in the unit of 150 MHz and the assigned galactic properties correspond to their average value over the cosmic-ray confinement volume. Also, we assume that inverse-Compton scattering proceeds in the Thomson regime, which is valid for GeV-scale electrons. The total cooling time, $t_{\rm cool}$, is estimated as

$$\frac{1}{t_{\rm cool}} = \frac{1}{t_{\rm syn}} + \frac{1}{t_{\rm IC}} + \frac{1}{t_{\rm brems}} + \frac{1}{t_{\rm ion}}. \tag{3.10}$$

The relative contribution of each cooling process depends on the electron energy, as well as $n_{\rm gas}$, B, and $w_{\rm ISRF}$. If we adopt typical Milky Way parameters, e.g., $n_{\rm gas} \simeq 0.3\ {\rm cm^{-3}}$, $B \simeq 6\ \mu{\rm G}$, and $w_{\rm ISRF} \simeq 1\ {\rm eV\ cm^{-3}}$, then the electrons that produce 150 MHz radio emission cool primarily via bremsstrahlung. In many galaxies, the magnetic field in synchrotron-emitting regions is found to be $B \simeq 10\ \mu{\rm G}$ under the assumption of cosmic rays and magnetic field equipartition (Beck et al., 2019) (see, however, an arguments against equipartition models in starburst galaxies by Thompson et al., 2006), suggesting that synchrotron losses are important. Our focus on quiescent galaxies may motivate adopting target densities more consistent with massive elliptical galaxies that have lower gas densities, $\sim 10^{-2}\ {\rm cm^{-3}}$ (Mathews & Brighenti, 2003), so then bremsstrahlung and ionization losses may become unimportant. However, the magnetic fields of these galaxies are not tightly constrained.

The third effect pertains to cosmic-ray escape, which competes with each energy-loss process. In the Milky Way, measurements of radioactive cosmic-ray nuclei indicate that GeV-scale cosmic rays are confined over a timescale of $t_{\rm esc} \sim 10^8$ yr (Evoli et al., 2020; Morlino & Amato, 2020), which indicates that GeV leptons lose most of their energy, although there are alternative models that suggest much shorter escape times (Cowsik & Madziwa-Nussinov, 2016; Lipari, 2017). We note that in small galaxies that do not efficiently confine cosmic-rays within their bulk, self-confinement near sources may be important (Fujita et al., 2010, 2011; Malkov et al., 2013; Nava et al., 2016; D'Angelo et al., 2018; Evoli et al., 2018; Fang et al., 2019).

The competition between cooling and escape sets the lifetime of cosmic-rays in galaxies to be:

$$\frac{1}{t_{\rm life}} = \frac{1}{t_{\rm esc}} + \frac{1}{t_{\rm cool}}, \tag{3.11}$$

which is related to the conversion efficiency of the injected electron power to the synchrotron radiation as

$$f_{\rm syn} = \frac{t_{\rm life}}{t_{\rm syn}}, \tag{3.12}$$

which depends on the cosmic-ray confinement time, magnetic field strength, and radiation/gas densities. Most naively, $f_{\rm syn}$ is expected to be higher for more massive galaxies that confine cosmic rays for longer times. In the following, we assume a scaling between $f_{\rm syn}$ and M_*:

$$f_{\rm syn} = \alpha_{\rm syn} \left(\frac{M_*}{10^{10}\ M_\odot} \right)^{\beta_{\rm syn}} . \tag{3.13}$$

In steady state, the radio luminosity of an SFG is the product of the injection rate of nonthermal electrons (Q_e) and $f_{\rm syn}$. The total 150 MHz luminosity can be expressed as the sum of contributions from different source classes:

$$L_{150} = f_{\rm syn} \sum_s \chi^s_{150} Q^s_e, \tag{3.14}$$

where s denotes the source class, Q^s_e is a function of ψ and M_* (Eqs. 3.1–3.2, 3.4, 3.6), and χ^s_{150} depends on the source electron spectrum and the galactic magnetic field.

Combining Eqs. (3.1)–(3.4), (3.6) and (3.13)–(3.14), we represent the components of the radio luminosity with the following functional forms:

$$\begin{aligned} L_{150} &\propto M_*^{\beta_{\rm syn}} \psi \ : \text{ SNR primary (and normal pulsars)} \\ L_{150} &\propto M_*^{\beta_{\rm syn}} \psi^{1+\beta_{pp}} \ : \text{ SNR secondary} \\ L_{150} &\propto M_*^{1+\beta_{\rm syn}} \ : \text{ MSP} \end{aligned} \tag{3.15}$$

In Sec. 3.4, we use these to fit the LOFAR data and constrain the free parameters in our model.

Finally, we note that low-frequency radio emission can be affected by free-free absorption by ionized gas. For typical galactic densities, the 150 MHz radio emission is not affected (Israel & Mahoney, 1990; Hummel, 1991; Basu et al., 2015; Marvil et al., 2015; Chyży et al., 2018). However, in dense starburst galaxies, this can significantly reduce the 150 MHz luminosity (Torres, 2004; Clemens et al., 2010). We do not include this effect in the model for simplicity.

3.2.6 A Schematic Illustration of the Effect of MSPs on the Radio-SFR Correlation

In this section, we qualitatively describe the expected modification of the radio-SFR correlation induced by MSPs. In Fig. 3.1 (top) we show the expected modification to the radio-SFR correlation in a scenario which includes MSP contributions. Specifically, the figure depicts the sum of two source terms, from SNR (Eq. 3.1) and MSP (Eq. 3.6), with scatter that mimics source-to-source variation in $f_{\rm syn}$ (Eq. 3.12). Note that we ignore the dependence of $f_{\rm syn}$ on ψ and M_* here.

This figure highlights two aspects of our model. First, the effect of MSPs should be pronounced only in massive and low-SFR galaxies, as quantified in Eq. (3.7). Therefore, MSP contributions can be clearly seen by splitting the sample into mass bins. Second, there should be source-to-source scatter due to galactic variations in the properties that affect the cooling of high-energy electrons (see Eq. 3.9). However, theoretical modelling of the luminosity variation would require knowledge of the dispersion in the physical parameters of quiescent galaxies, which is largely unconstrained by observations.

Since the radio-SFR plot hides the masses of each galaxy, it may be useful to plot luminosities and SFRs scaled by stellar masses. Figure 3.1 (bottom) illustrates a schematic expectation for luminosity/M_* - SFR/M_* plane. As the injection by MSPs is proportional to M_*, we would expect a plateau in this plane, if we ignore the dependence of $f_{\rm syn}$ on mass and SFR. In addition, in this projection the transition point from SNR to MSP domination is uniquely determined by the efficiency $\eta_e^{\rm MSP}$ (see Eq. 3.7) without any degeneracy with the radiation efficiency $f_{\rm syn}$. Therefore, this plot would be useful to assess the contribution of MSPs to the galactic radio emission.

3.3 Data Analysis

In this section, we develop a method for comparing our models with the LOFAR data. First, in Sec. 3.3.1, we briefly describe the dataset used in this work, and then in Sec. 3.3.2, we introduce our fitting methodology.

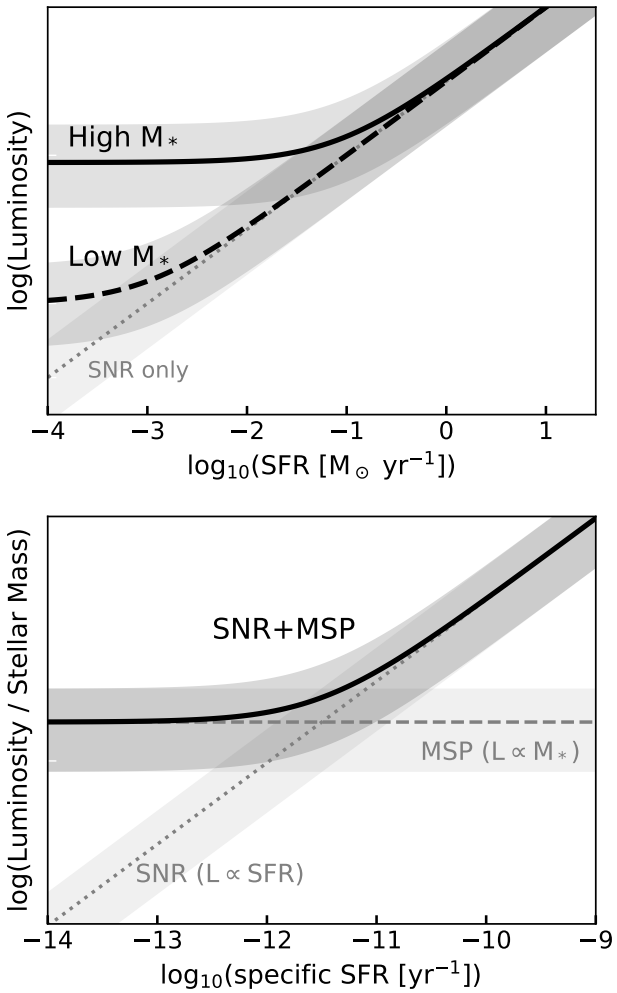

Figure 3.1. A schematic illustration of how MSPs can modify the radio-SFR correlation. While the radio-SFR correlation is dominated by the SNR in active galaxies, MSPs can dominate the flux of quiescent galaxies. This trend is particularly true for high-mass galaxies.

3.3.1 Dataset

We utilize the flux densities, SFRs, and stellar masses of 15088 galaxies analyzed by G18. We refer the reader to Gürkan et al. (2018) for critical information regarding search strategies, catalog choices, and instrumental systematics, but summarize the key features here. G18 obtained flux density measurements for these sources from the HATLAS/NGP field survey, spanning the redshift range $0 < z < 0.6$, and then utilized a multi-step process to isolate SFGs.

First, they identified radio-loud AGN by utilizing the radio source catalog constructed by (Best & Heckman, 2012). Then, they divided the remaining sources into SFGs, Composite Systems, Seyferts, LINERs, and Ambiguous sources, utilizing a modified BPT-diagram focused on four emission lines: [NII]λ6584, [SII]λ6717, Hβ, OIIIλ5007, and Hα. The necessity of a clear detection for each emission line sets a flux threshold that weights the sample toward systems observed at $z \lesssim 0.25$. They fit multi-wavelength photometric data with the MAGPHYS code to derive SFRs (averaged over the last 100 Myr) and the galactic stellar mass. Sources with bad MAGPHYS fits were removed from the analysis. In the end, 3907 SFGs were analyzed by Gürkan et al. (2018), and we use the same population in the following.

We note that 6370 of 15088 sources analyzed by G18 cannot be classified by BPT-diagram due to the lack of clearly detected emission lines. Because these sources can be contaminated by AGN emission, we do not use these unclassified sources in the main analysis. However, G18 find that they typically have low SFRs and high masses, where we expect that the contribution from MSP can be important. In Appendix B.4, we use these unclassified sources later to test the robustness of our results.

3.3.2 Model Comparison

To examine the role that MSPs play in the production of 150 MHz radio emission, we produce several models utilizing the source classes described in Secs. 3.2.1 through 3.2.4. First, we follow G18 and utilize a straightforward model for the radio-SFR correlation:

$$L^{\rm model} = \alpha \psi^{\beta}, \tag{3.16}$$

where β is the index of the correlation, α is a normalization factor, and $L^{\rm model}$ is the expected 150 MHz radio luminosity. For an alternative model, we add a mass-dependent term.

$$L^{\rm model} = \alpha \psi^{\beta} M_*^{\gamma}. \tag{3.17}$$

In addition to these two empirical models, we construct two physically motivated models based on the source classes discussed in Secs. 3.2.1 through 3.2.4. The first has only terms depending on the prompt SFR, and thus has a functional form:

$$L^{\rm model} = (a_1 \psi + a_2 \psi^{\beta_{pp}}) M_*^{\beta_{\rm syn}}, \tag{3.18}$$

In the second, we add a contribution from MSPs including a mass-dependent component:

$$L^{\rm model} = [a_1 \psi + a_2 \psi^{\beta_{pp}} + a_3 M_*] M_*^{\beta_{\rm syn}}. \tag{3.19}$$

To reduce the number of free parameters, we fix $\beta_{pp} = 0.18$ based on γ-ray observations, noting that this choice does not affect our conclusions.

Finally, multiple confounding variables may also affect the radio flux in any given galaxy, including variations in $f_{\rm syn}$, additional sources (e.g., sub-dominant AGN activity), or additional sinks (e.g., dense gas). Thus, we introduce an intrinsic dispersion into our model. Specifically, we assume a probability distribution for the radio luminosity that follows a Gaussian distribution defined as:

$$P_i(L) = \frac{1}{\sqrt{2\pi\sigma^2}} \exp\left(-\frac{|L - L^{\rm model}|^2}{2\sigma^2}\right), \tag{3.20}$$

where we define σ to be a combination of the measured uncertainty for each source and a modeling error. Quantitatively, we set $\sigma^2 = (cL^{\rm model})^2 + L_{\rm err}^2$, where c is a free parameter that accounts for the intrinsic model variation and $L_{\rm err}$ is the 1σ measurement error. We obtain best-fit parameters by minimizing the negative of the log-likelihood, $-\ln\mathcal{L} = -\sum_i \log(P_i)$, where the summation is taken for all sample SFGs. We utilize the IMINUIT code (James & Roos, 1975) to find the best-fit model and calculate the error matrix for each model parameter. To calculate the best-fit parameters and likelihood values, we use the units $[10^{23}$ W Hz$^{-1}]$ for the radio luminosity and $[10^{10}$ M$_\odot]$ for the stellar mass. Notice that while this affects the total quoted likelihood, it does not affect the difference of the log-likelihood values, ΔLG($\mathcal{L}$), among different models.

Many studies of the radio-FIR correlation have analyzed the logarithmic correlation between each luminosity, using logarithmic error bars that relate to the fractional flux of the signal. Here, however, we utilize the true luminosity, because about 20% of the SFGs in our study have best-fit luminosities that are negative (possibly due to instrumental or systematic issues). If a full likelihood profile were available for the measured radio luminosity of each source, either choice should give the same final results. However, as G18 quote only 1σ error bars, the choice of calculating likelihood profiles in linear or logarithmic space can affect the final answer. In Appendix B.1, we analyze the data by utilizing a fit to the log-luminosity and analyzing only sources with positive luminosity, where we use

$$P_i(L) = \frac{1}{\sqrt{2\pi\sigma^2_{\log_{10} L}}} \exp\left(-\frac{|\log_{10}(L) - \log_{10}(L^{\rm model})|^2}{2\sigma^2_{\log_{10} L}}\right), \tag{3.21}$$

where $\sigma_{\log_{10} L}$ is a parameter that accounts for the dispersion. We find that our results are unchanged.

Finally, in our best-fit models, we find that 11 sources have a value of $-\ln\mathcal{L}$ larger than 50, representing a 7σ rejection of our models for these sources. In each case, this stems from a source that is significantly brighter than our model prediction. Because alternative methods of producing bright radio emission (such as undetected AGN and galaxy interactions) may be present, we remove such sources from our fit so that they do not bias the relationship. In Appendix B.2, we include these sources and show that this treatment does not alter our conclusions.

3.4 Results

In this section, we present the results of our analysis. In Sec. 3.4.1, we fit the data with empirical power-law models, showing that the inclusion of a mass dependence is significantly preferred. In Sec. 3.4.2, we analyze physically-motivated models and show that the inclusion of MSPs significantly improves the fit to sources in low-SFR and high-mass regime. In Sec. 3.4.3, we discuss the viability of MSP scenario based on the best-fit parameters. Finally, in Sec. 3.4.4, we discuss important uncertainties in our results.

3.4.1 Testing the Simple Scaling Models

We first analyze and compare our simple scaling models (Eqs. 3.16 and 3.17) with the LOFAR data. The goal of this portion of the analysis is to determine whether total galaxy mass plays an important role in determining the observed radio luminosity.

Figure 3.2 shows the correlation between the radio luminosity and SFR, splitting our results into four mass bins. The orange points and error bars show the measured radio fluxes and uncertainties for individual SFGs in our sample. The SFR and stellar mass for each SFG are determined from MAGPHYS fits (da Cunha et al., 2008; Gürkan et al., 2018). The gray and blue points correspond to the *predicted best-fit* values for these same SFGs, based on our models (theoretical uncertainties are discussed below).

This analysis shows that a simple scaling between the SFR and the observed radio luminosity (Eq. 3.16) systematically underpredicts the radio luminosity in galaxies with star-formation rates smaller than $\sim 0.1 M_\odot$ yr^{-1}. Adding a dependence on mass (Eq. 3.17) adds a large scatter to the radio-SFR correlation and improves the fit.

We note that our likelihood function includes a significant dispersion (see Eq. 3.20) that is not represented on this plot. This implies that it would be possible for the model with only ψ-scaling to provide an equally good fit to the LOFAR data, even though the $\psi + M_*$ model appears to better match the data in the figure. This could happen in a scenario where the dispersion in the LOFAR data is not related to the galactic mass. We examine this scenario as follows.

In Table 3.1, we calculate the mass dependence in the LOFAR data by comparing the log-likelihood fits of each model. We find that the addition of a mass-dependent term improves the quality of fit to the radio data by $\Delta\mathrm{LG}(\mathcal{L}) = 838$. If we restrict our analysis to only quiescent galaxies (132 have sSFR less than 10^{-11} yr^{-1}), we still improve the fit to the data by $\Delta\mathrm{LG}(\mathcal{L})$ = 212. This is notable, because this cut includes only 3% of the galaxy counts (and is often biased towards galaxies with the largest radio uncertainties), but contributes nearly 25% of the total improvement to the log-likelihood. This indicates that the mass dependence of the radio-SFR correlation is most pronounced in galaxies with the lowest current SFRs.

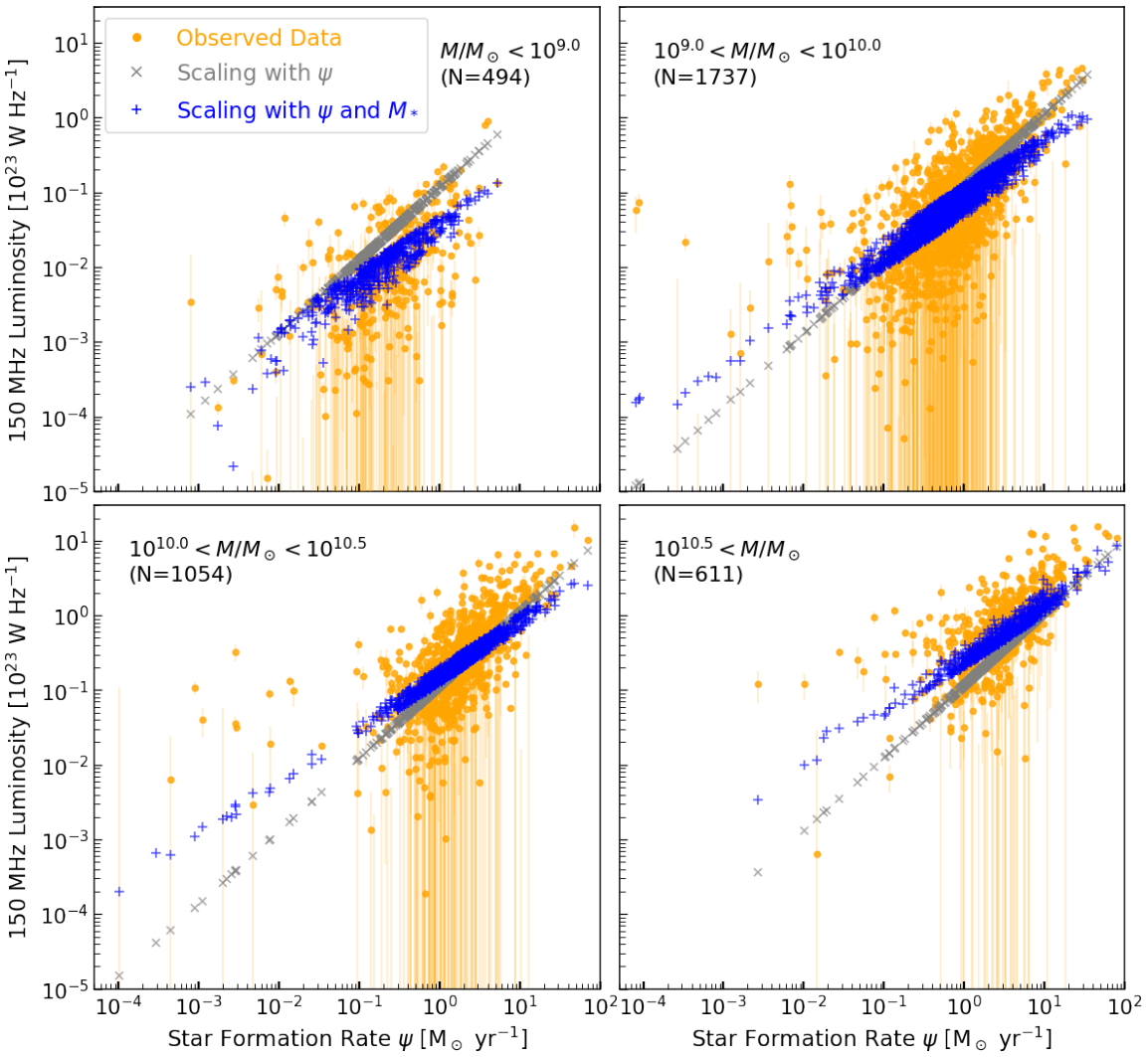

Figure 3.2. The 150 MHz luminosity distribution of SFGs as a function of SFR (this and M_* for each source are derived with MAGPHYS). The sample is split into four mass bins as labeled. Orange (circle) points show the observed LOFAR 150 MHz luminosities and 1σ errorbars. Gray (cross) and blue (plus sign) points are the best-fit luminosities predicted by the scaling relations (Eqs. 3.16 and 3.17). The model with mass dependence (blue) fits better than prediction by SFR alone (gray), though neither can sufficiently explain low-SFR bright sources.

Table 3.1. Values of $-\ln\mathcal{L}$ for different models. We show the sum of all SFGs (middle) and of low-sSFR SFGs ($< 10^{-11}$ yr^{-1}, right).

	All Sources ($N = 3896$)	Low sSFR ($N = 132$)
Scaling (ψ; Eq. 3.16)	-391.4	258.4
Scaling (ψ and M; Eq. 3.17)	-1229.4	46.6
Model (SNR only; Eq. 3.18)	-894.5	209.5
Model (SNR + MSP; Eq. 3.19)	-1419.1	-69.3

Table 3.2. Best-fit parameters for our simple scaling models. In parentheses, we show the best-fit values obtained in G18.

	α	β	γ	c
ψ	0.115	0.976	-	1.51
	(0.115)	(1.07)	-	-
ψ and M_*	0.124	0.702	0.422	1.41
	(0.135)	(0.77)	(0.43)	-

These results are consistent with those of G18, which also found a correlation between luminosity and stellar mass (see their Fig. 9). However, our results indicate that even in models that include a mass-dependent term, the predictions of scaling models tend to underestimate the radio luminosity of quiescent galaxies in a systematic fashion.

In Table 3.2, we show the best-fit parameters for both simple scaling models. In our default model, we obtain $\beta = 0.98$, close to the value of unity predicted from the radio-SFR correlation. In our mass-dependent model, β drops to 0.70, an indication that there is degeneracy between the mass and star-formation rate, as expected. The model dispersion, c, is found to be $\sim$1.5 for both models, which suggests that the data has an intrinsic variation that spans a factor of $\sim$5 at the $\sim 3\sigma$ level. This provides additional evidence that simple scaling models cannot explain bright low-SFR sources. The best-fit parameters derived in our work are similar to those in G18.

3.4.2 Testing the Physical Models

Figure 3.3 compares the two physical models for radio emission, described in Eqs. (3.18) and (3.19), with observations. Compared to our simple scaling models, the SNR-only model (light blue, squares) has two additional degrees of freedom, including separate contributions from primary and secondary electrons (with different ψ-dependences), as well as a slight mass dependence relating to the efficiency of synchrotron production. However, this model is still incapable of explaining the bright radio emission from low-SFR sources, implying that the mass-dependent changes in the synchrotron prodcution efficiency are unlikely to explain the observed trend in the data.

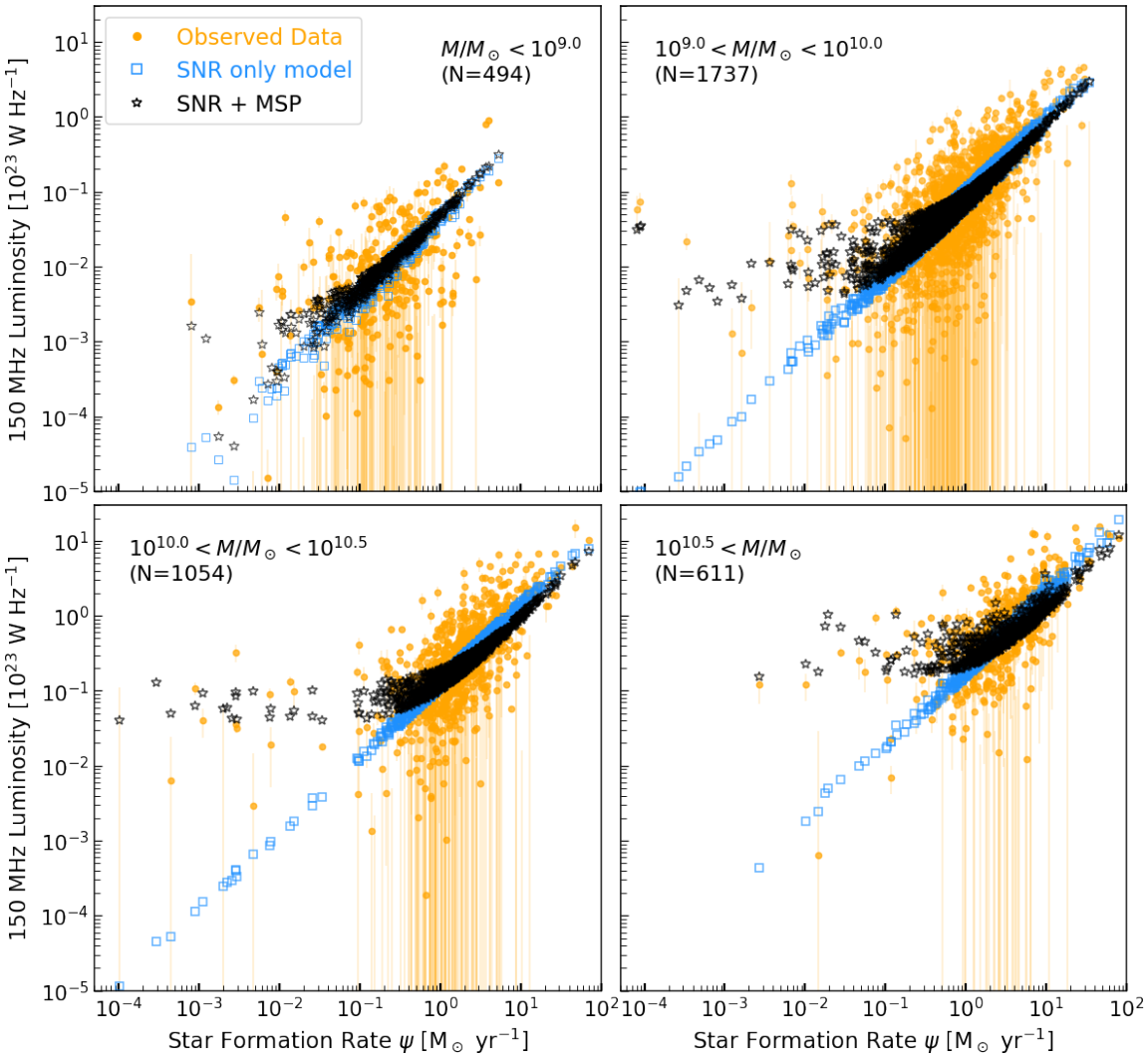

Figure 3.3. Same as Fig. 3.2, but for two physically-motivated models (Eqs. 3.18 and 3.19). Light blue (square) points show the model that only includes SNR contribution, which cannot fit the low-SFR data. Black (star) points show the predictions when MSPs are included, which significantly improves the fit to the LOFAR data.

Table 3.3. Best-fit parameters for our models.

	a_1	a_2	a_3	$\beta_{\rm syn}$	c
SNR only	0.110	2.00e-10	-	0.285	1.46
SNR+MSP	0.035	0.031	0.036	0.106	1.39

Our final model includes a contribution from MSPs, with a total flux that depends exclusively on the total galactic mass (black, star). Intriguingly, this significantly improves our fit to the radio data, particularly among the population of quiescent galaxies. In Table 3.1, we find that this model improves the log-likelihood fit by 525, producing a significant preference for this model compared to the SNR-only model. Restricting our analysis to only galaxies with low sSFR ($< 10^{-11}$ yr^{-1}), we still find a log-likelihood improvement of 279, corresponding to significant detection even among only the 132 least luminous sources.

We note that our physical SNR-only model provide a worse fit (by a log-likelihood of $\sim$306) than our simple scaling model that depends on ψ and M_*, even though the SNR model has an extra degree of freedom. This is due to the fact that the scaling model prefers a power of ψ that is smaller than one. Such a scenario is incompatible with the assumption of our SNR-only model, because the power of ψ is fixed to either 1.0 or 1.18 for primary (secondary) components. This indicates that star-formation-driven sources (with an input power that is at least linearly dependent on ψ) are unlikely to drive the radio excess in quiescent galaxies. Additional factors, such as a competitive energy-loss process (like a cosmic-ray escape component that depends strongly on ψ) would be necessary to explain this data. However, this is not observed in bright SFGs, where the radio-FIR relation is found to be steeper than linear.

In Table 3.3, we list best-fit parameters for our physical models. The normalization for the secondary term, a_2, is found to be unphysically small for the SNR-only model. This can be understood based on the preference of our scaling model (with ψ and M_*) for a best-fit value $\beta < 1$. Among the two terms that scale as ψ and $\psi^{1.18}$, the best-fit model would only require the first term. This result indicates that our standard SNR model may be unable to provide a good fit to the data. Interestingly, we note that the SNR+MSP model predicts a value of a_2 that is physically reasonable.

We should note that there are also sources that are significantly less luminous than our model predictions. However, our models would also predict significant dispersion in the radio luminosity of individual SFGs, which may explain these sources.

In particular, in some systems $f_{\rm syn}$ may be small due to either efficient escape, a strong radiation field, a high gas density, or a weak magnetic field, all of which can lower the synchrotron signal. In addition, free-free absorption may significantly reduce the radio flux in galaxies with high gas densities. Some LOFAR sources even have radio luminosities that are negative, a clear indication of systematic or instrumental effects that are not included in our model. We also note that, contrary to very dim sources, bright sources are difficult to explain solely by a variation in $f_{\rm syn}$, because it cannot exceed 100%.

To examine the overall fit to the data, we calculate the chi-squared statistic, $\chi^2 = \sum_i |L_{i,\rm model} - L_i|^2/\sigma_i^2$, where the summention runs for all sources and σ_i^2 is the sum of $(cL_{i,\rm model})^2$ and $L_{i,\rm err}^2$. We find $\chi^2 = 5141$ for our MSP+SNR model (sample size

3896), whereas $\chi^2 = 6002$ for the SNR-only case, the null hypothesis. This goodness-of-fit is dominated by the many points at high SFR, where we expect that the SNR-only model should sufficiently fit the data. To examine the goodness-of-fit for low specific-SFR sources, we re-calculate χ^2 using only the 132 sources that have ψ/M_* less than 10^{-11} yr^{-1}. For our MSP+SNR model, the χ^2 is 205, whereas it is 1063 for the SNR-only null hypothesis. These fit still have $\chi^2/d.o.f$ larger than 1, which indicates that the fit still is not perfect. However, such a deviation should be expected based on the simplicity of our model. Our aim is to point out that adding mass-dependent term would significantly improve the fit — and the large $\Delta\chi^2$ obtained from the addition of such a term indicates that a mass-dependent term is likely the most important parameter that can be added to model radio-emission from low-specific-SFR sources.

3.4.3 Interpretation of Results

In the previous section, we have shown that the LOFAR data strongly prefers a physical model that includes at least one emission term that depends only on the galaxy mass. In Sec. 3.2.4, we noted that a model including MSP-accelerated electrons would predict such a feature. This does not, however, prove that MSPs are the physical source of the excess radio emission. In this section, we show that such a scenario is possible, and, in fact, that current data suggests that MSPs can power bright radio emission with an intensity that is consistent with the excess.

Combining Eqs. (3.6, 3.14, 3.13) and the third term in Eq. (3.19), we can write the MSP radio intensity as:

$$a_3 = \frac{4}{3}\chi_{150}^{\rm MSP}\alpha_{\rm syn}\eta_e^{\rm MSP}L_{38}^{\rm MW}, \tag{3.22}$$

where a_3 is best-fit parameter of the MSP contribution in Eq. (3.1), $\chi_{150}^{\rm MSP}$ is the ratio of the 150 MHz-emitting electron power to the total electron power, and the factor 4/3 arises from the conversion from W Hz^{-1} to erg s^{-1} at 150 MHz. We note that the electron power in the 150 MHz window is calculated over $\Delta \ln E_e = 0.5$, as the luminosity is calculated by integrating the flux density over $\Delta \ln \nu = 1$.

The radio spectral index of galaxies is approximately $F_\nu \propto \nu^{-0.7}$ near GHz frequencies and flattens to $F_\nu \propto \nu^{-0.5}$ near 100 MHz, which is likely caused by cooling and propagation effects (Israel & Mahoney, 1990; Hummel, 1991; Basu et al., 2015; Marvil et al., 2015; Chyży et al., 2018). This translates to a steady-state differential electron spectrum of $E_e^{-2.4}$ above a few GeV and $E_e^{-2.0}$ below that. Adopting this spectral shape for electrons, we obtain $\chi_{150}^{\rm MSP} \sim 0.1$, a value that only weakly depends on the spectral break and minimum electron energy.

The efficiency of synchrotron emission, $\alpha_{\rm syn}$, may also depend on galaxy properties (see Eq. 3.13). For simplicity, we adopt typical Milky Way parameters to estimate the energy-loss timescales. We also assume that massive galaxies are calorimetric to cosmic-ray leptons, as is the case in the Milky Way (Strong et al., 2010). Under these assumptions, we obtain $\alpha_{\rm syn} \sim 0.2$, which gives us:

$$\eta_e^{\rm MSP} \simeq 1(L_{38}^{\rm MW})^{-1}. \tag{3.23}$$

Thus, we find that the best-fit normalization of the MSP contribution ($a_3 = 0.036$) does not violate the total power of the MSP population. However, since $L_{38}^{\rm MW} \sim 1$, this relation implies that our model does require the majority ($\eta_e^{\rm MSP} \sim 1$) of the MSP spindown power to be injected into electrons. This might initially appear worrisome, as some previous estimates have utilized efficiencies of $\eta_e^{\rm MSP} \sim \eta_\gamma \sim 0.1$. However, there has (to date) been no study validating these assumptions.

Additionally, there are a number of uncertainties in our modeling that may significantly affect this result. Most importantly, the energetics of galactic MSPs are unknown. In this study, we normalize the total γ-ray luminosity of MSPs to Milky Way observations. However, our MSP models are expected to dominate only in galaxies with low-SFRs and high masses, which may have different star formation histories than the Milky Way. Notably, if we instead normalized our results to M31, which has properties more consistent with quiescent galaxies (a larger stellar mass and a smaller SFR, see, e.g., Yin et al., 2009; Sick et al., 2015), the necessary MSP efficiency would decrease by up to a factor of ∼4. Also, because the γ-ray emission from MSP magnetosphere may be beamed, only some fraction of Galactic MSPs, f_b, can be observed from the Earth. Although f_b is often assumed to be unity for γ-ray pulsars, the actual value could be smaller by a factor of ∼2 (Johnson et al., 2014), which would decrease the efficiency $\eta_e^{\rm MSP}$ by a factor of $1/f_b$. These (among other) uncertainties could lower the necessary efficiencies to the ∼10% level.

In addition to observational uncertainties that may make the MSP efficiency smaller than our model prediction, we note that a large MSP e^+e^- efficiency is consistent with our understanding of pulsar physics. Observations indicate that roughly 10% of the MSP spin-down power is converted into γ-ray emission within the magnetosphere, a negligible fraction of the total spin-down power is converted to radio, and the remaining power is carried primarily by e^+e^- pairs, the magnetic field, and possibly ions. Although we lack knowledge concerning the energetics of the MSP pulsar wind, it is established for young pulsars that more than ∼90% of the spindown power is converted to pulsar-wind electrons that power the PWNe (Coroniti, 1990).

Observationally, the constraints on GeV-scale MSP emission are not strong. Yuan & Ioka (2015) found that e^+e^- efficiencies up to 90% can be reconciled with MSP models of the galactic center excess. Intriguingly, studies of GeV emission from the Galactic bulge by Ajello et al. (2016) find that the inverse-Compton flux exceeds standard predictions, requiring a bright new source of energetic electrons. At the TeV scale, a stacking analysis of 24 MSPs observed at TeV energies by the HAWC telescope provided 2.6–3.2σ evidence of TeV MSP emission, a result which would require a high efficiency for TeV e^+e^- pair production from MSPs (Hooper & Linden, 2018c). We note that observations of globular clusters in VHE γ-rays suggest efficiencies below ∼ 10% (Bednarek et al., 2016; MAGIC Collaboration, 2019). However, this result assumes particularly optimistic models for particle propagation within globular clusters (a Bohmian diffusion model), which has yet to be verified. Extrapolating this result to GeV energies also depends sensitively on spectral assumptions.

In light of these points, we conclude that MSPs can be efficient e^+e^- accelerators. The necessity of a ∼ 100% e^+e^- efficiency may stretch current modeling. However, multiple uncertainties in our models may significantly lower the efficiency necessary to fit the radio excess. Furthermore, no observation rules out efficiencies as high as ∼90%.

3.4.4 Testing the Robustness of MSP Models

We have shown that MSP-based models explain the flattening trend observed and detailed by G18. Here we note several systematic uncertainties that could affect the plateau detected by G18. We stress that while our models were fit to the G18, the qualitative hypothesis that MSPs contribute to the radio-SFR correlation does not necessarily require a flattening of the data at the level observed by G18.

In particular, we note that the accurate determination of the SFR and radio flux in the dimmest quiescent galaxies pushes the limits of current observational data. One worrisome point concerns any potential flux-sensitivity limit in the radio data. Such a limit could induce a plateau-like feature by excluding a vast sea of "missing" galaxies with smaller radio fluxes. However, the methodology applied by G18 specifically accounts for such a scenario — reporting the best-fit flux (including negative best-fit fluxes) for all galaxies that are determined to be SFGs via multi-wavelength photometric fits. We note two other facts that diminish the risk of such a systematic error. On the observational side, the large redshift range of SFG studies would smear out simple flux-sensitivity limits. On the theoretical side, we note that our model predicts the existence of very dim radio galaxies, due to the significant dispersion induced by variations in the magnetic field, ISRF, and interstellar gas densities in each galaxy.

While systematic uncertainties in the radio luminosity are likely controlled by the analysis methods of G18, a more pressing concern may be the accurate determination of the star-formation rate. Because only a small number of quiescent galaxies are classified as SFGs in the G18 sample (and spectral-line classification of SFG samples may depend on the SFR of the galaxy), a systematic bias that shifts some galaxies to abnormally low-SFRs independent of their radio flux may be interpreted as a plateau feature in the radio-SFR correlation. We stress that in G18, SFRs and masses are derived by MAGPHYS fit based on multiwavelength photometric data from SDSS u-band to submillimeter wavelength. However, the sensitive dependence of our results on this fit deserves further investigation.

A complete re-analysis of the SFRs in quiescent SFGs lies beyond the scope of this theoretical work. Here, we test the results by replacing the SFRs and masses with those contained in the GSWLC-2 catalog of Salim et al. (2018) (hereafter S18, see also Salim et al., 2016). The galactic properties in this catalog are derived by SED fitting to the UV, optical and mid-IR data with the CIGALE code (Noll et al., 2009). We refer the reader to Salim et al. (2016, 2018) for detail, but stress that one notable difference from G18 is that S18 includes short-wavelength UV radiation, which may produce more accurate measurements for quiescent galaxies. S18 produces three separate catalogs, shallow, medium, and deep UV imaging surveys, and we use the medium (GSWLC-M2), which is recommended for quiescent galaxies.

We cross-correlate the catalog of S18 with G18, noting that only 1094 out of 3907 SFGs in G18 are included in the S18 catalog because GSWLC-M2 does not cover all SDSS targets. This is potentially a significant concern — as important selection effects in the join-observation probability of the catalogs may affect our results, and are difficult to quantitatively assess. Keeping this in mind, we repeat our analysis, utilizing the radio luminosities and source classifications of G18 but utilize the SFRs and masses determined by S18. In

Appendix B.3, we detail our analysis procedure.

We obtain a somewhat concerning result, which is that S18 systematically derives higher SFRs for the low-SFR galaxies observed by G18. This potentially suggests that the choice of methods for SFR measurements can have a significant impact.

In Fig. 3.4, we show the radio-SFR correlation for our combined G18/S18 analysis, finding that the plateau feature produced in the G18 SFR calculation has disappeared, and a mass-dependent term (such as that from MSPs) is no longer statistically preferred. This is potentially worrisome, as it suggests the possibility that observations by G18 could be explained by systematic uncertainties in SFR measurements.

One possibility to explain this discrepancy is that the classification of "SFG" sources by G18, which selects only a small fraction of the sources with low-SFRs, systematically biased the catalog towards sources that will have larger SFRs in S18. To test this possibility, we repeat cross-correlated study using radio luminosities from G18, but SFR measurements from S18. However, we loosen the restriction that the galaxy in question is labeled a SFG by G18, and instead also include "unclassified" sources from G18. This increases our total population to 10277 sources, and adds a large population of sources that have low SFRs in both the G18 and S18 analyses. However, it potentially contaminates our result with galaxies that are

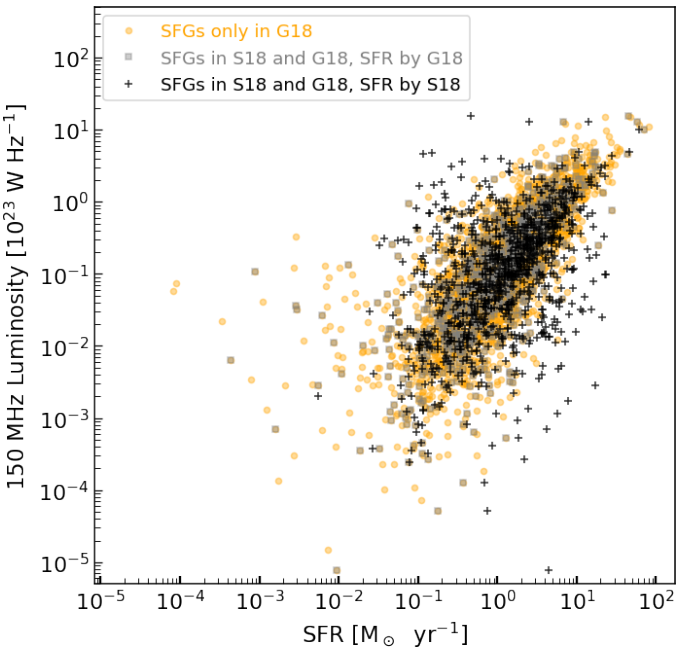

Figure 3.4. Comparison of the radio-SFR correlation for two different SFR estimations. We note that the SFR estimates of S18 significantly decrease the significance of the plateau feature observed in the radio-SFR correlation by G18.

radio bright due to low-luminosity AGN.

In Appendix B.4, we detail this analysis, finding that this cross-correlation improves both the global and low-SFR agreement between G18 and S18. In this case, we find strong evidence in this dataset for a mass-dependent term compatible with our MSP hypothesis even in the dataset by S18. We caution however, that AGN contaminated sources may also produce such a feature.

We thus conclude that a careful analysis of low-SFR galaxies is necessary in order to verify the contribution of MSPs to the radio emission in low-SFRs. Utilizing the results of the detailed study completed by G18, we find strong evidence in the data to support such a feature. The significance of this result decreases significantly if the results of S18 are instead used to calculate the SFRs of quiescent galaxies — although the convolution of these studies make it difficult to interpret these results. One possible explanation may be systematic effects stemming from the interplay between the SFG-classification of galaxies in G18, and their total SFR utilizing the methods of S18. Futher analysis is thus necessary to confirm the plateau feature of G18 which is best fit by MSPs in our study.

We stress that a significant MSP contribution to the nonthermal radio luminosity is independently motivated by potential HAWC observations of γ-ray emission from MSPs (Hooper & Linden, 2018c). Our main point is that the contributions from MSPs should be present, and future radio observations will be important to constrain the population of cosmic-ray electrons produced by MSPs.

3.5 Discussion and Conclusions

In this Chapter, we propose that MSPs can significantly contribute to the radio flux in quiescent galaxies, dominating the low-end tail of the radio-SFR correlation. We show that models including an MSP contribution significantly improve the fit to LOFAR radio data, explaining the observed excess in low-SFR, high-mass galaxies. We show that the energetics of our model are consistent with current observations and models of MSP activity. Finally, we discuss systematic uncertainties and future directions to test our model. Our results have several implications.

3.5.1 Radio-SFR (Radio-FIR) Correlation

Previous studies of the radio-FIR correlation have found a striking continuation of power-law behavior over many orders of magnitude in galactic star-formation rate (e.g., Helou et al., 1985; Condon, 1992; Yun et al., 2001; Bell, 2003)) This has been attributed to a variety of factors, the sum of which has been labeled a “conspiracy” in the low-SFR behavior of the relationship. LOFAR data, on the other hand, appear to provide evidence for a break in that relationship among high-mass, low-SFR galaxies, and our interpretation offers yet another complicating factor that may shift this relationship from its linear functional form. Our model predicts that future observations of the radio-SFR correlation by LOFAR, as well as next-generation telescopes like SKA, will more clearly identify excess radio emission in high-mass galaxies that do not host AGN.

The tightness of the radio-FIR correlation has raised an expectation that the radio contin-

uum emission can serve as a robust SFR tracer that is not affected by dust extinction. Our analysis suggests that the extrapolation of radio-SFR correlation to low sSFR sources may be insecure, and that future studies of radio emission in low-SFR galaxies should include MSP contributions. Alternatively, more detailed studies of the time-evolution of the MSP population and how it contributes to the galactic radio luminosity may allow radio measurements to inform measurements of star-formation histories in quiescent galaxies.

Finally, the LOFAR data have also been used to perform direct studies of the radio-FIR correlation in 150 MHz band (Read et al., 2018). Based on our results, one would expect excess radio emission for sources that have low FIR luminosity. This is not clearly seen in the data (though the uncertainties in the FIR luminosities for these sources are large). We speculate that this suggests another "conspiracy" in the radio-FIR correlation. For massive galaxies, the radio luminosity is enhanced due to MSPs, and the FIR is also enhanced by the heating of interstellar dust by old stellar populations. Indeed, multiple studies have shown that intermediate and old stellar populations can produce significant IR emission even for galaxies with little star formation (Salim et al., 2009; Calzetti et al., 2010). This new conspiracy might be important for future studies.

3.5.2 Bright Radio/γ-ray Emission from the Bulge of Disk Galaxies

Although AGN have been removed from the LOFAR sample using BPT-diagram diagnostics, potential radio contributions from relatively-dim supermassive black holes cannot be ruled out. This scenario is particularly troubling, because supermassive black hole masses have been found to correlate with the total galaxy mass (Magorrian et al., 1998), providing an alternative explanation for the mass dependence detected in our model (see also G18).

However, nearby, spatially resolved galaxies provide an excellent opportunity to differentiate these scenarios and study the contribution of MSPs to galactic radio emission. If the radio flux is dominantly from AGN, we would expect emission only from the galactic core, and would potentially expect variable emission. On the other hand, MSPs emission would be more extended (although it can be significantly enhanced in the bulge region) and should show no variability.

In addition, observations indicate that LMXBs and MSPs are highly overabundant in dense regions, such as globular clusters, compared to their average formation rate throughout the Milky Way plane (Grindlay, 1984). Therefore, cross-correlating diffuse radio emission with globular clusters may provide evidence for an MSP origin of the radio excess.

Intriguingly, there are several nearby galaxies that host large LMXB populations and also have bright diffuse radio excesses, most notably M31 (Voss & Gilfanov, 2007; Ackermann et al., 2017; McDaniel et al., 2019). Notably, McDaniel et al. (2019) determined the M31 bulge to be powered by an electron flux of $\sim 10^{39}$ erg s^{-1}, while SNRs are expected to injection only $\sim 5 \times 10^{37}$ erg s^{-1}. Utilizing a $M_* = 4 \times 10^{10}$ $M_\odot$ stellar mass for the M31 bulge (Eckner et al., 2018), our model predicts that MSPs inject an electron flux of $\sim 8\eta_e^{\rm MSP} \times 10^{38}$ erg s^{-1}, explaining the majority of the electron power.

3.5.3 Implications for γ-ray and Cosmic-Ray Astrophysics

Finally, our results suggest that MSPs may efficiently convert a large fraction of their spin-down power into GeV-scale e^+e^- pairs. Because MSPs do not include compact pulsar wind nebulae, these e^+e^- pairs must escape into the ISM, where they subsequently cool via a combination of synchrotron (producing radio emission) and inverse-Compton scattering/bremsstrahlung (producing γ-ray emission). The ratio of these components depends sensitively on the galactic environment.

Recent observations have found a bright excess in GeV γ-ray emission from the Galactic center of the Milky Way galaxy (Goodenough & Hooper, 2009; Daylan et al., 2016). The most convincing explanations for this excess consist of dark matter annihilation (Goodenough & Hooper, 2009; Daylan et al., 2016) or the production of GeV γ-ray emission within MSP magnetospheres (Abazajian, 2011; Bartels et al., 2016; Lee et al., 2016). Our model predicts that any such MSP population will be accompanied by a bright inverse-Compton emission in the Milky Way bulge.

The impact of such a scenario on the interpretation of the Galactic center excess is unclear. At GeV energies, there is some evidence for excess inverse-Compton emission in the Milky Way bulge. In particular, models by the Fermi-LAT collaboration required that the normalization of the inverse-Compton scattering emission from the inner regions of the Milky Way was brighter than standard Galprop predictions (which, notably, do not include any cosmic-ray injection in the Galactic center region) (Ajello et al., 2016). Alternative models that do include significant hadronic cosmic-ray injection near the Galactic center include more modest enhancements to the leptonic emission (Carlson et al., 2016).

Our results suggest that GeV-scale e^+e^- from MSPs can significantly contribute to the background γ-ray emission from the Galactic center, a scenario which may be compatible with MSP models for the Galactic center excess. On the contrary, if the MSP-induced ICS emission continues to TeV energies, the lack of bright TeV emission within the Galactic bulge would place a strong constraint on the contribution of beamed MSP emission to the Galactic center excess at GeV energies (Hooper & Linden, 2018c). If MSPs do produce bright TeV γ-rays via inverse-Compton scattering, a number of Milky Way MSPs are expected to be local and powerful enough to be seen by current and future TeV telescopes such as HAWC and CTA.

As an efficient e^+e^- accelerator, MSPs may produce a substantial contribution to the local e^+e^- flux, potentially contributing to the positron excess observed by PAMELA and AMS-02 (Adriani et al., 2010; Aguilar et al., 2013). While some recent analyses, (e.g., Venter et al., 2015) argued that single MSPs explain only a few-percent of the excess, these results assumed electron production efficiencies of only a few percent. On the other hand, Kisaka & Kawanaka (2012) used an efficiency of 50% from spindown power to e^+e^- pairs and found that MSPs can significantly contribute to the observed cosmic-ray electron and positron flux. As our analysis provides additional evidence supporting high e^+e^- efficiencies in MSPs, it supports scenarios where MSPs significantly contribute to the positron excess.

Finally, even in low-SFR galaxies that are supposed to have little astrophysical emission, e^+e^- pairs from MSPs may produce bright radio and γ-ray emission. This can be an addi-

tional source of background emission for indirect searches of dark matters. In this context, the contribution from MSPs are evaluated in Winter et al. (2016), but they only consider direct γ-ray emission from the magnetosphere. Our results suggest that pulsar-wind e^+e^- could significantly contribute to the background emission, potentially making additional factor of confusion for future dark-matter searches. Due to the small size of dwarf galaxies, the lumninosity of such a component might depend on the ability of MSPs to self-confine their own cosmic-ray electron population.

Chapter 4

Micorquasar SS433: Extreme Particle Accelerator Uncovered by Multi-wavelength Study

This chapter is based on the paper "Multiwavelength Emission from Galactic Jets: The Case of the Microquasar SS433" by Sudoh T., Khangulyan D., Inoue Y., 2020, published in the Astrophysical Journal, Volume 889, Issue 2, id.146, 10 pp.

4.1 Introduction to this Chapter

Microquasar SS433 is a binary system consisting of a compact object (most likely a black hole) and a supergiant star (e.g., Hillwig et al., 2004; Hillwig & Gies, 2008; Kubota et al., 2010; Cherepashchuk et al., 2019), which is believed to feed a super-critical accretion disk (e.g., Begelman et al., 2006; Medvedev & Fabrika, 2010; Cherepashchuk et al., 2013). Thanks to its relative proximity (5.5 kpc, Blundell & Bowler, 2004; Lockman et al., 2007) and a number of unique features, this object has been intensively studied for decades, though many aspects remain mysterious (see Fabrika, 2004, for a review). A particularly striking feature is a pair of jets, which are launched almost perpendicular to the line of sight and show periodic precession and nodding motion (Abell & Margon, 1979; Fabian & Rees, 1979). They are mildly relativistic ($v = 0.26c$, where c is the speed of light) and have plenty of power ($\sim 10^{39}$ erg s^{-1}) (e.g., Marshall et al., 2002; Brinkmann et al., 2005). The jets interact with the surrounding nebula W50, believed to be a supernova remnant (e.g., Dubner et al., 1998; Green, 2004).

Recently, the HAWC collaboration has reported the detection of $\gtrsim 25$ TeV γ-rays from the jets of SS433 (Abeysekara et al., 2018). The locations of the γ-ray emission are ~ 30 pc away from the binary both in the eastern and western side and coincide with nonthermal X-ray emitting regions (Watson et al., 1983; Yamauchi et al., 1994; Brinkmann et al., 1996; Safi-Harb & Ögelman, 1997; Safi-Harb & Petre, 1999). This indicates that these regions are plausible sites for the acceleration of high-energy particles. SS433/W50 has also been detected with Fermi (Bordas et al., 2015, 2017; Xing et al., 2019; Rasul et al., 2019; Sun et al., 2019), though the origin of the HE γ-ray emission remains unclear. Imaging atmospheric Cherenkov

telescopes have not yet detected this system either from the jets nor from the binary in the VHE regime (Kar, 2017; Ahnen et al., 2018).

Multi-wavelength emission from the jets of SS433 provides us with valuable opportunities to study the acceleration of particles in astrophysical jets in great detail. There are a number of theoretical studies on the nonthermal emission in microquasars (e.g., Atoyan & Aharonian, 1999; Heinz & Sunyaev, 2002; Romero et al., 2003; Bosch-Ramon et al., 2006; Gupta et al., 2006; Orellana et al., 2007; Reynoso et al., 2008; Perucho & Bosch-Ramon, 2008; Romero & Vila, 2008; Bordas et al., 2009; Vila & Romero, 2010; Pepe et al., 2015; Molina & Bosch-Ramon, 2018; Khangulyan et al., 2018a; Reynoso & Carulli, 2019). The detection of TeV γ-rays from SS433 provides new important constraints on emission models. However, there are only a few studies that utilize new observational data, and the results remain somewhat controversial. Abeysekara et al. (2018) focused on the eastern region and concluded that the radio, X-ray and VHE data can be well-fit with leptonic models. On the other hand, Xing et al. (2019) studied the western region and argued that leptonic models have difficulties in explaining the radio and X-ray data simultaneously. Because both papers adopt simple models, where particles are continuously injected throughout the source lifetime (30 kyr) and cooled only via radiative loss, a new theoretical study with more detailed physical consideration is needed to uncover the origin of the emissions from the jets of SS433.

Here, we study the nonthermal emission from the SS433 jets in the light of recent multi-wavelength observations. We aim to assess the validity of leptonic models, to examine the efficiency of particle acceleration and processes responsible for that, and to study prospects for future observations. Going beyond prior work noted above, we consider the spatial distribution of emission along the jet and include adiabatic loss due to the jet expansion.

In Fig. 4.1, we schematically show how an astrophysical jet and the emission sites can be modeled. Galactic and extragalactic jets often contain multiple compact emitting regions ("knots"), which may appear distinct due to various reasons. For example, an X-ray knot may correspond to the region with a locally enhanced magnetic field. In the case of SS433, the jets are launched to both eastern and western sides, each of which contains multiple X-ray knots, and in Fig. 4.1 we only show one side of the jet. We mainly analyze the emission from the innermost knots ("e1" and "w1") to compare results with Abeysekara et al. (2018) and Xing et al. (2019), but also address the emission of different regions qualitatively. Also, we consider the case where the acceleration site matches the onset of the innermost knot. We only study leptonic emission, since hadronic emission is already disfavored as the dominant source of TeV γ-rays from SS433 (Abeysekara et al., 2018). However, the inferred electron acceleration efficiency can also have implications for the production of high-energy protons.

In Sec. 4.2, we present a general model for the particle evolution and emission in relativistic jets. In Sec. 4.3, we briefly review the observational properties of SS433. In Sec. 4.4, we compare our model predictions with the multi-wavelength data from the two X-ray knots. In Sec. 4.5, we study the morphology of the emission regions. In Sec. 4.6, we note limitations to our results. In Sec. 4.7, we summarize our results and discuss further implications.

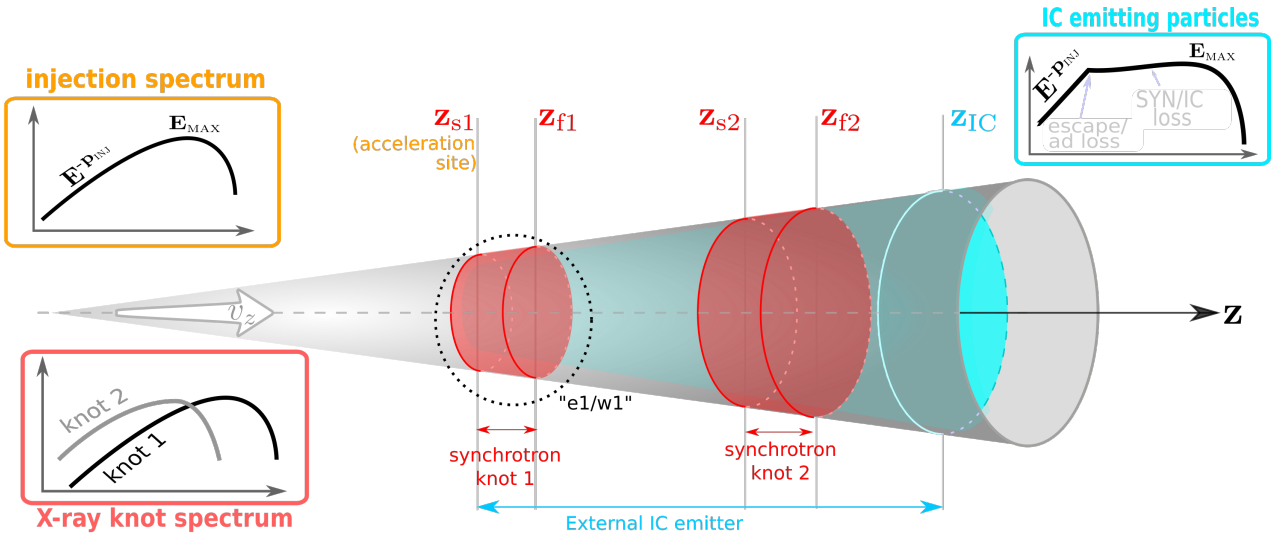

Figure 4.1. Schematic illustration of our model for the jet, emission regions, and expected energy distributions of particles. (This figure is modified from the published version to illustrate a specific case of our model of SS433 knots. In the published version, we show more general cases where the acceleration site is different from the onset of the X-ray knot.)

4.2 Physical Conditions in Relativistic Jet

4.2.1 Energetics

Let us consider a relativistic jet of total power $L_{\rm jet}$. The jet radius depends on the coordinate on the jet axis, denoted as z: $R = R(z)$. The jet energy flux is

$$L_{\rm jet} = \pi R^2(z) w \Gamma^2 v_z, \tag{4.1}$$

where w is the plasma enthalpy per unit volume, v_z is the jet velocity, and $\Gamma = \left[1 - (v_z/c)^2\right]^{-\frac{1}{2}}$ is the bulk Lorentz factor. The enthalpy is carried by protons, leptons and magnetic fields. We assume that the jet power is distributed by dimensionless fractions η_p, η_e, and η_B for each component, such that $\eta_p + \eta_e + \eta_B = 1$. The proton contribution determines the mass flux:

$$\dot{M}_{\rm jet} = \pi R^2(z) n_p m_p \Gamma v_z. \tag{4.2}$$

The magnetic field is necessary for the acceleration of particles and the production of synchrotron radiation. Its energy is carried as the Poynting flux:

$$L_B = \frac{v_z \Gamma^2 R^2(z) B^2(z)}{4}, \tag{4.3}$$

where B is the strength of the magnetic field in the plasma co-moving frame, and we assume that it is perpendicular to the jet velocity in the above expression for simplicity. From this, we can express B as

$$B(z) = \frac{2}{\Gamma R(z)} \sqrt{\frac{\eta_B L_{\rm jet}}{v_z}}. \tag{4.4}$$

4.2.2 Particle Acceleration

The process responsible for the acceleration of nonthermal particles in the microquasar jet is not certain. We characterize it by an efficiency $\eta_{\rm acc}(>1)$. The time required for a particle to gain energy E is

$$t_{\rm acc} = \eta_{\rm acc} \frac{r_L}{c}, \tag{4.5}$$

where $r_L = E/(eB)$ is the relativistic gyroradius.

The confinement of particles in the acceleration region implies the following condition:

$$R(z) > \sqrt{6 t_{\rm acc} D}, \tag{4.6}$$

where D is the particle diffusion coefficient and we assume a three dimensional case. This is similar to the Hillas criterion ($r_L < R$, Hillas, 1984). We introduce a parameter $\eta_g(>1)$, known as gyro-factor, and characterize the spatial diffusion as $D = \eta_g D_{\rm Bohm}$, where $D_{\rm Bohm} = c r_L/3$ is the Bohm diffusion coefficient. Combining above equations, we obtain

$$R(z) B(z) > \frac{E}{e} \sqrt{2 \eta_{\rm acc} \eta_g}, \tag{4.7}$$

which constrains the maximum energy of particles that can be confined in the jet during the acceleration process:

$$E < E_{\rm max}^{\rm con} = \frac{e}{\Gamma}\sqrt{\frac{2\eta_B L_{\rm jet}}{v_z \eta_{\rm acc}\eta_g}}. \tag{4.8}$$

The confinement condition is not the only constraint, as the particle acceleration is also limited by energy losses. In this work we consider emission from electrons. Thus, in the highest-energy regime, the synchrotron cooling may provide the dominant loss mechanism, where the energy loss timescale is

$$t_{\rm syn} = \frac{3(m_e c^2)^2}{4c\sigma_T E}\left(\frac{B^2}{8\pi}\right)^{-1}, \tag{4.9}$$

where σ_T is the Thomson cross section and m_e is the electron mass. The acceleration is possible while it proceeds on a shorter timescale than cooling, $t_{\rm acc} < t_{\rm syn}$, which sets the maximum energy of particles:

$$E < E_{\rm max}^{\rm syn} = m_e c^2 \sqrt{\frac{6\pi e}{\sigma_T \eta_{\rm acc} B}}\,. \tag{4.10}$$

The magnetic field used above should be evaluated in the acceleration site, which can in principle differ from that in the emission region.

4.2.3 Particle Cooling

Accelerated particles are subject to energy losses due to adiabatic and radiative cooling. The adiabatic loss rate due to the expansion of the jet is

$$\dot{\gamma}_{\rm ad} = \frac{\gamma}{3}\frac{d\ln\rho}{dt} = -\frac{2}{3}\frac{\Gamma v_z}{R(z)}\frac{\partial R}{\partial z}\gamma, \tag{4.11}$$

where ρ is number density of matter in the jet, and we assume that the jet speed v_z is constant (thus ρR^2 is also constant).

The radiative losses for high-energy electrons are dominated by the synchrotron emission and IC scattering. The synchrotron loss rate is

$$\dot{\gamma}_{\rm syn} = -\frac{4c\sigma_T\gamma^2}{3m_e c^2}\left(\frac{B_{\rm eff}^2}{8\pi}\right), \tag{4.12}$$

where the magnetic field $B_{\rm eff}$ corresponds to the averaged effective field strength. If the magnetic field strength is constant, B, and the pitch angles between the particle velocity and the magnetic field are random, we should use $B_{\rm eff}^2 = 2B^2/3$. In more general cases, the field strength may have spatial variation within the emission region probably due to magnetic turbulence (Bykov et al., 2012; Kelner et al., 2013). Then, the magnetic field distribution function is needed to obtain $B_{\rm eff}$.

To describe the IC losses we need to consider the contributions from all relevant photon fields. A precise treatment requires integration over photon energy and angular distribution, which can be complex. Fortunately, the photon energy distribution is often described by a black-body like spectrum, where the photon field is defined by its temperature T and energy

density $u_{\rm rad}$ or, equivalently, by the dilution coefficient:

$$\kappa = \frac{15\hbar^3 c^3 u_{\rm rad}}{\pi^2 k_B^4 T^4}, \tag{4.13}$$

where k_B is the Boltzmann constant and $\hbar = h/(2\pi)$ is the Dirac constant. If the bulk Lorentz factor is small and the target photon is black-body like, the simple approximate description obtained by Khangulyan et al. (2014) is applicable for the energy losses including the Klein-Nishina effect:

$$\dot{\gamma}_{\rm ic} = -\frac{3\sigma_T k_B^2 T^2 mc^2 \kappa}{4\pi^2\hbar^3 c} G_{\rm iso}^{(0)}\left(4\gamma\frac{k_B T}{mc^2}\right) g_{\rm iso}\left(4\gamma\frac{k_B T}{mc^2}\right), \tag{4.14}$$

where the function $G_{\rm iso}^{(0)}(u)$ and $g_{\rm iso}(u)$ are given in their Eq. (38) and (20) respectively. In more general cases, when the bulk Lorentz factor is large or the photon direction deviates from isotropic, we need to perform integration over the photon angular distribution.

4.2.4 Particle Evolution

The distribution of nonthermal particles in the jet can be described with the energy-spatial density, n, as $dN = nd\gamma dz$, where dN is the number of particles. The density is described by the transport equation:

$$\begin{aligned}\frac{\partial}{\partial t}n(\gamma,t,z) + v_z\frac{\partial}{\partial z}n(\gamma,t,z) + \frac{\partial}{\partial\gamma}[\dot{\gamma}_{\rm cool}(\gamma,t,z)n(\gamma,t,z)] \\ = \dot{q}_{\rm inj}(\gamma,t,z),\end{aligned} \tag{4.15}$$

where $\dot{q}_{\rm inj}dz$ is the rate of particle injection in the jet segment $(z, z+dz)$. In this equation and hereafter in this Chapter, we ignore relativistic effects because the jet velocity of SS433 is only mildly relativistic ($\Gamma \simeq 1.04$).

We assume that nonthermal particles are accelerated at a specific coordinate $z = z_{\rm acc}$:

$$\dot{q}_{\rm inj}(\gamma,t,z) = \dot{q}_0(\gamma,t)\delta_D(z - z_{\rm acc}) \tag{4.16}$$

where δ_D is the Dirac function. For simplicity, we consider the case where the cooling rate $\dot{\gamma}_{\rm cool}$ depends only on γ. Then, the solution of the transport equation is obtained analytically:

$$n(\gamma,z,t) = \frac{\dot{\gamma}_{\rm cool}(\gamma')}{v_z\dot{\gamma}_{\rm cool}(\gamma)}\dot{q}_0(\gamma',t')\mathcal{H}(z - z_{\rm acc}), \tag{4.17}$$

where $t' = t - (z - z_{\rm acc})/v_z$, $\mathcal{H}$ is the Heaviside function and γ' is an energy parameter determined by

$$z - z_{\rm acc} = v_z\int_\gamma^{\gamma'}\frac{d\gamma''}{-\dot{\gamma}_{\rm cool}(\gamma'')}. \tag{4.18}$$

To calculate the total emission from a specific region along the jet, we integrate the particle distribution over the emitting region ($z_s<z<z_f$):

$$\frac{dN}{d\gamma} = \int_{z_s}^{z_f} dz\, n(\gamma,z,t). \tag{4.19}$$

Assuming a steady injection ($\partial\dot{q}_0/\partial t = 0$), we obtain

$$\frac{dN}{d\gamma} = \frac{1}{v_z\dot{\gamma}_{\rm cool}(\gamma)}\int_{z_s}^{z_f} dz\dot{\gamma}_{\rm cool}(\gamma')\dot{q}_0(\gamma'), \tag{4.20}$$

where γ' is determined by $z_{\rm acc}$, z, and γ via Eq. (4.18). Since we focus on compact knots much smaller than the jet length, $(z_f - z_s) \ll z_f$, we assume that the change in radius is also small, $R(z_f) - R(z_s) \ll R(z_f)$, and evaluate $\dot{\gamma}_{\rm ad}$ and $B(z)$ at $z_I = (z_s + z_f)/2$ to omit the z dependence. Also, we assume that the onset of emission region matches the acceleration site, i.e., $z_{\rm acc} = z_s$.

We assume that particles are accelerated to a power-law energy distribution above $\gamma > \gamma_{\rm min}$ with an exponential cutoff:

$$\dot{q}_0(\gamma) \propto \gamma^{-p_{\rm inj}} \exp\left(-\gamma/\gamma_{\rm max}\right)\mathcal{H}(\gamma - \gamma_{\rm min}), \tag{4.21}$$

where $\gamma_{\rm max}$ is defined from either Eq.(4.8) or (4.10).

The power carried by relativistic electrons, $\eta_e L_{\rm jet}$, defines the normalization for the energy distribution:

$$\int_{\gamma_{\rm min}}^{\gamma_{\rm max}} \dot{q}_0(\gamma)\gamma d\gamma = \frac{\eta_e L_{\rm jet}}{m_e c^2}. \tag{4.22}$$

The value of $\gamma_{\rm min}$ is theoretically related to the energy scale where thermal particles are injected into the acceleration processes. This is extensively studied but still contains large uncertainties (Amano & Hoshino, 2012). We assume a minimum electron energy of 1 GeV. Smaller values of $\gamma_{\rm min}$ would increase the total electron energy required in the spectral fitting but do not alter the shape in the energy range of interest.

Once the electron distribution is determined, we calculate the spectral energy distribution from synchrotron and IC radiation in jet frame, taking into account Klein-Nishina effect (e.g., Blumenthal & Gould, 1970; Aharonian et al., 2010; Khangulyan et al., 2014). In more general cases when the bulk Lorentz factor is large, we need to apply relativistic transformations to obtain the spectral energy distribution in the observer frame.

4.2.5 Qualitative Description of the Particle Spectrum

If the particle cooling time is shorter than the advection time, $t_{\rm adv} = (z_f - z_s)/v_z$, the particle spectrum is described by the standard formula (fast cooling regime):

$$\frac{dN}{d\gamma} \simeq \frac{1}{\dot{\gamma}(\gamma)} \int_{\gamma}^{\infty} d\gamma' \dot{q}(\gamma'). \tag{4.23}$$

For a power-law injection with $p_{\rm inj} \simeq 2$, this expression reduces to $dN/d\gamma \simeq \dot{q}(\gamma) t_{\rm cool}$. In this regime, the electron energy distribution has a break, at which the particle power-law index is changed by 1, caused by the transition from the synchrotron/Thomson to adiabatic cooling (or un-cooled). This is qualitatively shown in Fig. 4.1 labeled as "IC emitting particles."

If we consider emission from compact knots, the advection time may be shorter than the cooling time (slow cooling regime). The particle spectrum is described by

$$\frac{dN}{d\gamma} \simeq \dot{q}(\gamma) t_{\rm adv}, \tag{4.24}$$

which has a shape similar to the injection spectrum. This is qualitatively shown in Fig. 4.1 labeled as "knot 1." In knots further away from the acceleration site, the particle number per unit energy per unit volume remains unchanged at lower energies. However, the cutoff

energy in the spectrum may be reduced due to the cooling; this can be directly seen from Eq. (4.18). This is qualitatively shown in Fig. 4.1 labeled as "knot 2."

4.2.6 Knot Size

Observations in radio, optical, or X-ray often reveal knots in Galactic and extragalactic jets. In general, their size may be determined by either of the following factors: (i) nonthermal cooling; (ii) size of the jet region with an enhanced magnetic field; (iii) size of the region where the acceleration takes place or time elapsed since the onset of the acceleration process.

If the knot size is determined by the particle cooling, the energy requirements for the acceleration process are minimal and the spectral slopes are typical ones for the fast cooling regime. If the particle acceleration occurs at a specific location in the jet, advective particle transport determines the knot size, s, as $s \simeq \Gamma v_z t_{\rm cool}(E)$. If synchrotron losses are dominant, the cooling time depends on the particle energy, $t_{\rm cool} \propto 1/E$. The synchrotron emission frequency ω and particle energy relate as $E \propto \sqrt{\omega/B}$, and thus the knot size should depend on the photon frequency as $s \propto 1/\sqrt{\omega}$. If adiabatic losses dominate the particle cooling, the knot size does not depend on the particle energy. Adiabatic cooling generally does not produce compact knots, except for specific hydrodynamic structures of the jet. For example, for a constant velocity jet and conical or parabolic shape, it operates on a scale comparable to the jet length.

The synchrotron emissivity is sensitive to the magnetic field strength. If some portion of the jet has an enhanced magnetic field, it may appear as a compact, bright spot. This may result in different morphology for the synchrotron and IC emission (see Fig. 4.1).

The acceleration does not necessarily proceed at a specific point in the laboratory frame, and may be associated with a fluid element. In this case, the knot size depends on the size of the acceleration site and the typical diffusion length, $\lambda_{\rm D}$. Because the diffusion length $\lambda_{\rm D} \propto \sqrt{t}$, the size of the knot should have a weaker dependence on the photon frequency as compared to the synchrotron cooling scenario.

There can also be a possibility that the acceleration has started recently and the knot size is limited by the advection distance since the moment of onset of the acceleration. This would produce a gradual increase in the knot size with time. However, this may be difficult to observe on a reasonable timescale.

4.3 Application to SS433

4.3.1 Properties of SS433 Jets

Observations of the jets of SS433 provide necessary parameters for the formalism presented in Sec. 4.2. We adopt a distance of $d = 5.5$ kpc, which is obtained from deep radio imaging (Blundell & Bowler, 2004). Long-term observations and kinematic modelings of the Doppler-shifted emission lines place tight constraints on the jet precession model. They yield a jet speed of $v_z = 0.26c$ (Margon & Anderson, 1989; Eikenberry et al., 2001), or equivalently, $\Gamma = 1.04$.

Models of the jet emission indicate that the mass-loss rate at the jet base is $\dot{M}_{\rm jet} \gtrsim$

$10^{-7} M_\odot$ yr^{-1}, which leads to the estimates for the kinetic energy without rest mass energy, $(\Gamma - 1)\dot{M}_{\rm jet} c^2$, which typically fall within $\sim (0.2 - 5) \times 10^{39}$ erg s^{-1}. (e.g., Kotani et al., 1996; Brinkmann & Kawai, 2000; Marshall et al., 2002; Brinkmann et al., 2005; Medvedev & Fabrika, 2010; Waisberg et al., 2019). Because estimates for the total jet power $L_{\rm jet}$ have uncertainties, instead of using η_e and η_B, we will leave $L_e (= \eta_e L_{\rm jet})$ and $L_B (= \eta_B L_{\rm jet})$ as free parameters. We adopt the jet kinetic energy of 10^{39} erg s^{-1} at the jet base, and assume that part of this is dissipated to L_e and L_B, i.e., we keep $L_e + L_B < 10^{39}$ erg s^{-1}.

We assume a conical jet, and parametrize the radius with the opening angle α_j as $R(z) = z\alpha_j$. We adopt a radius of $R(z_I) = 6$ pc, comparable to the size of X-ray emission (Safi-Harb & Ögelman, 1997). With this parameterization, Eq. (4.11) reduces to

$$-\dot{\gamma}_{\rm ad} = \frac{2}{3}\frac{\Gamma v_z}{z}\gamma. \tag{4.25}$$

The photon field is also a necessary ingredient as a target for the IC scattering. As we focus on the knot region away from the binary, the diffuse Galactic photons dominate over the radiation from the central object and synchrotron self-Compton component. We adopt a radiation field composed of the cosmic microwave background $(T, u_{\rm rad})$=(2.7 K, 0.26 eV cm^{-3}), far-infrared (30 K, 0.3 eV cm^{-3}), optical/near-infrared (5000 K, 0.6 eV cm^{-3}) and ultraviolet (20000 K, 0.1 eV cm^{-3}) photons (Porter et al., 2017b; Popescu et al., 2017).

4.3.2 Multi-wavelength Observations Toward X-ray Knots

The jets from SS433 have been intensively studied with multi-wavelength observations. Based on *ROSAT* and *ASCA* X-ray data, Safi-Harb & Ögelman (1997) defined distinct circular regions to east (e1, e2, e3) and west (w1, w2) from the binary. Combining *RXTE* data, the emission from e1 is fit with a single power law of $\Gamma_{\rm ph} = 1.43 \pm 0.1$ (Safi-Harb & Petre, 1999), while e2 is a broken power-law spectrum of $\Gamma_{\rm ph,1} = 1.6^{+0.2}_{-0.3}$ and $\Gamma_{\rm ph,2} = 2.6^{+0.6}_{-0.3}$ with a break at $E_b = 3.0^{+0.6}_{-0.5}$ keV (Safi-Harb & Ögelman, 1997). The eastern jet is also observed with *XMM-Newton* by Brinkmann et al. (2007). They found $\Gamma_{\rm ph} = 2.17 \pm 0.02$ for the brightest region in the eastern jet and $\Gamma_{\rm ph} = 1.85 \pm 0.06$ for a region closer to the binary. These regions are not identical to e2 and e1, though they overlap. It should be noted that the derived Galactic column density in Safi-Harb & Ögelman (1997) is $N_{\rm H} = 1.2^{+0.8}_{-0.5} \times 10^{21}$ cm^{-2} for e2, while it is $N_{\rm H} = 5.6^{+0.1}_{-0.1} \times 10^{21}$ cm^{-2} in Brinkmann et al. (2007). This may cause differences in the derived photon index.

In the VHE regime, the H.E.S.S., MAGIC, and VERITAS collaborations placed upper limits on the flux from knots (e1, e2, w1, w2) and termination region (e3) (Kar, 2017; Ahnen et al., 2018) following the definitions in Safi-Harb & Ögelman (1997). The HAWC collaboration reported the detection of VHE photons ($\gtrsim 25$ TeV) from regions that coincide with X-ray knots. The eastern emission is seemingly radiated from a region spanning over e1 and e2, and the western component is likely centered at w1, though both are not yet well localized.

In the radio band, fluxes from the knot regions are uncertain. The termination region (e3) is prominent in radio images and well-correlated with X-ray intensity maps. However, the knots, e1, e2, and w1, are not resolved in the 2.7 GHz map by the Effelsberg telescope (Geldzahler et al., 1980) nor in the recent 150 MHz map by LOFAR (Broderick et al., 2018). This suggests that the contribution from X-ray knots to the observed radio intensity may be

sub-dominant, and the radio fluxes should be treated as upper limits. Radio spectral index measurements would provide useful constraints on the spectral shape of nonthermal electrons. Downes et al. (1986) produced a radio spectral index map utilizing 1.7, 2.7 and 4.75 GHz data. However, the X-ray knots are not well localized also in this map.

In contrast to other wavelengths, recent results in the HE regime are controversial. Bordas et al. (2015) suggests that emission from nonthermal protons accelerated in the jet termination shock best explains the emission detected with Fermi/LAT. The analysis by Xing et al. (2019) suggests a one-sided jet morphology toward the w1 region. While these papers indicate no signature of time variation, Rasul et al. (2019) reports $\sim 3\sigma$ evidence for temporal modulation of the γ-ray emission with the precession period of the jet, which would indicate core origin (see also Molina & Bosch-Ramon, 2018). Sun et al. (2019) suggests that the morphology of the GeV emission is consistent with originating from the radio nebula W50. The spectrum and morphology are somewhat different from each other. Thus, it is difficult at this point to clearly define the HE γ-ray flux from the X-ray knots.

Further observations are needed to quantify the multi-wavelength properties of the X-ray knots better. Here, we constrain our model parameters by using the same dataset for radio, X-ray and VHE emission as in Abeysekara et al. (2018) and Xing et al. (2019), aiming at comparing model predictions with them. We also compare our model spectra with the GeV data from Bordas et al. (2017); Xing et al. (2019); Rasul et al. (2019); Sun et al. (2019), which are not used in the model fitting.

We adopt the definition of e1 as a circular region of radius $3.5'$ centered at $24'$ east from SS433, and w1 a circle of radius $3.75'$ centered at $19'$ west. These translate into parameter (z_s, z_f) as (32 pc, 44 pc) for e1 and (24 pc, 36 pc) for w1 in Eq. (4.19). We note that the *XMM-Newton* data used in Abeysekara et al. (2018) are taken from a slightly larger region (a circle of $6'$ radius centered at e1), which we do not take into account here.

4.4 Nonthermal Leptonic Emission from Nonthermal Knots in SS433 Jets

In Fig. 4.2, we show the spectral energy distribution for the e1 and w1 region. Our leptonic models explain the radio, X-ray and VHE data. For the GeV data, our predictions in the HE regime are far below the data for both regions. This indicates that it is difficult to explain the GeV data simultaneously with other wavelength data in the framework of our leptonic models from knot regions. Thus, most GeV photons should be produced in different regions or by different mechanisms.

In Table 4.1, we list the required parameters for the fit. The slope $p_{\rm inj}$ is determined from the radio and X-ray data, while L_B and L_e are derived by combining them with the HAWC data. The derived magnetic field strengths are 16 μG and 9 μG for e1 and w1, respectively.

The mechanism responsible for the maximum energy cannot be determined from this fit. We temporarily focus on the case where it is limited by synchrotron losses (Eq. 4.10). Then, the magnetic field and acceleration efficiency, $\eta_{\rm acc}$, define the maximum electron energy:

$$E_{e,\rm max}^{\rm syn} = 1.5 \text{ PeV} \left(\frac{\eta_{\rm acc}}{10^2}\right)^{-\frac{1}{2}} \left(\frac{B}{16\ \mu\text{G}}\right)^{-\frac{1}{2}}. \tag{4.26}$$

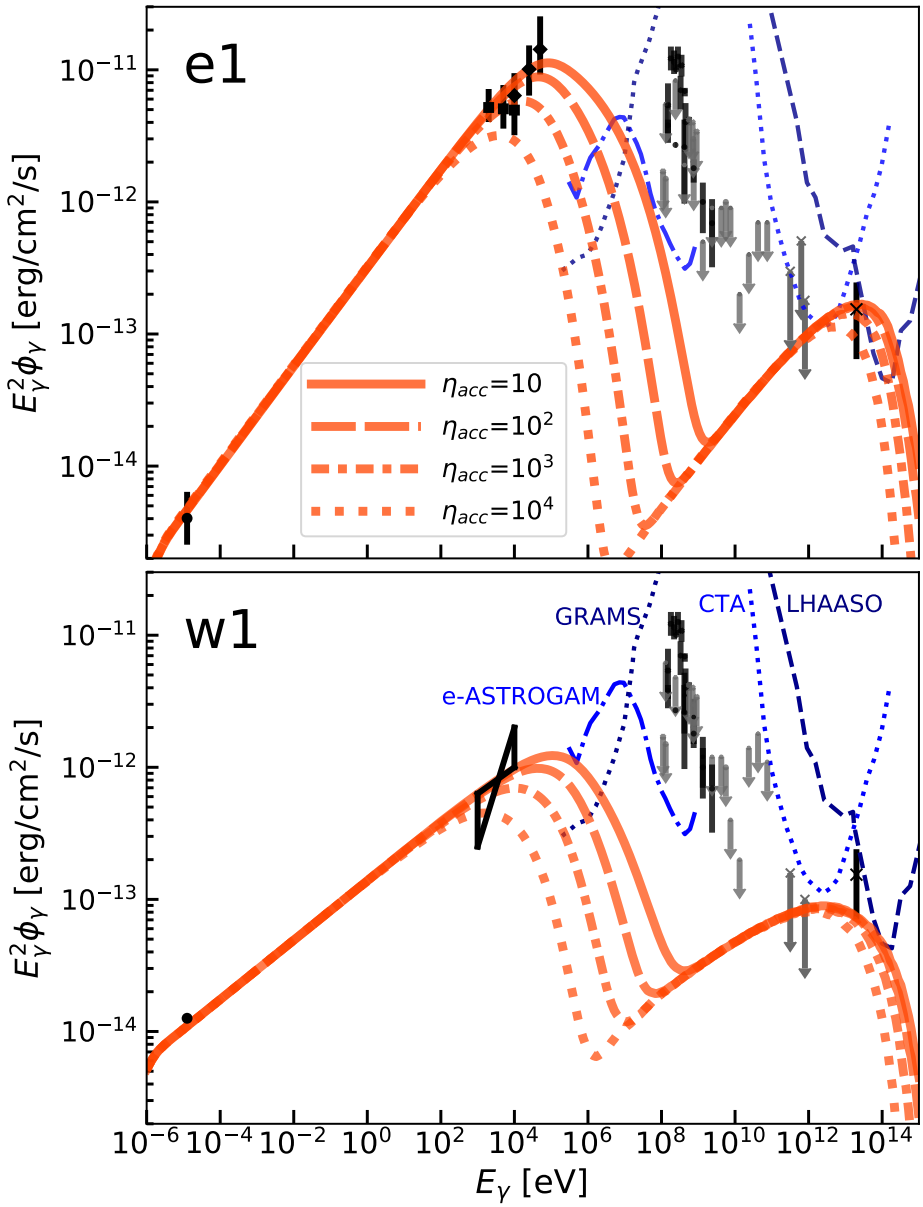

Figure 4.2. Broad-band spectral energy distribution of the e1 (top) and w1 (bottom) region. Orange curves are model predictions for different choices of $\eta_{\rm acc}$, as labelled. Black and gray points are observational data and upper limits, respectively, from Geldzahler et al. (1980) (radio), Brinkmann et al. (2007); Safi-Harb & Ögelman (1997); Safi-Harb & Petre (1999) (X-ray), Bordas et al. (2017); Xing et al. (2019); Rasul et al. (2019); Sun et al. (2019) (HE), Ahnen et al. (2018); Kar (2017); Abeysekara et al. (2018) (VHE). Expected sensitivities are also shown for CTA (North, 50 h; Acharya et al., 2017), LHAASO (1 yr; Bai et al., 2019), *e-ASTROGAM* (3 yr; De Angelis et al., 2017) and *GRAMS* (3 yr; Aramaki et al., 2020).

In our model, the hard X-ray data require $\eta_{\rm acc} \lesssim 10^2$ for both regions. Although our model does not specify the acceleration processes, it would be helpful to interpret $\eta_{\rm acc}$ in the framework of two representative scenarios. First, we consider diffusive shock acceleration. In this mechanism, particles gain energy as they cycle upstream and downstream across the shock front. The acceleration timescale in a parallel shock is given by $t_{\rm acc}^{\rm DSA} \simeq 10D/v_{\rm sh}^2$ (e.g., Bell, 2013). This translates into the efficiency in Eq. (4.5) as

$$\eta_{\rm acc}^{\rm DSA} \simeq \frac{10\eta_g}{3(v_{\rm sh}/c)^2} \simeq 10^2 \left(\frac{\eta_g}{2}\right)\left(\frac{v_{\rm sh}}{0.26c}\right)^{-2}. \tag{4.27}$$

Thus, our results suggest that the diffusion coefficient may satisfy $\eta_g \lesssim 2$, indicating strong particle confinement close to the Bohm limit. Such a high particle acceleration efficiency is known to be achieved in young supernova remnants (e.g., Stage et al., 2006; Uchiyama et al., 2007; Tsuji et al., 2019), while it is thought to be much more inefficient in extragalactic black hole jets (e.g., Araudo et al., 2015; Inoue & Tanaka, 2016; Tanada et al., 2019a) possibly due to the inefficiency of the diffusive shock acceleration mechanism in the relativistic regime (Bell et al., 2018).

Second, we consider the stochastic acceleration. In this mechanism, particles gain energy as they are resonantly scattered by magnetohydrodynamic turbulence (e.g., Dermer & Menon, 2009). Assuming that the smallest turbulence wavenumber is equal to R^{-1}, the timescale for acceleration is given by

$$t_{\rm acc}^{\rm S} \simeq \frac{1}{\kappa_B}\left(\frac{v_A}{c}\right)^{-2}\left(\frac{r_L}{R}\right)^{2-q} t_{\rm dyn}, \tag{4.28}$$

where κ_B is the ratio of the strength of turbulent field compared to the background field, $t_{\rm dyn} = R/c$ is the dynamical timescale and q describes the spectrum of the turbulence. This expression is derived under quasi-linear approximation ($\kappa_B \ll 1$), but has a wider applicability (O'Sullivan et al., 2009). The Alfven velocity $v_A = B/\sqrt{4\pi m_p n_p}$ can be expressed in the form of

$$\frac{v_A}{c} = \sqrt{\frac{L_B}{\Gamma \dot{M} c^2}} \tag{4.29}$$

Combining the above equations and assuming the Kolmogorov-type spectrum ($q = 5/3$), we have

$$\eta_{\rm acc}^{\rm S} \simeq \frac{10^3}{\kappa_B}\left(\frac{\dot{M}}{10^{-7} M_\odot\ {\rm yr}^{-1}}\right)\left(\frac{L_B}{10^{38}\ {\rm erg\ s}^{-1}}\right)^{-1}. \tag{4.30}$$

for $R = 6$ pc and $E = 1$ PeV. Thus, the stochastic acceleration is likely insufficient to reach the high efficiency of $\eta_{\rm acc} < 10^2$, though it is not firmly ruled out due to simplifications in this estimate.

So far we have focused on the case where electron energy is limited by the synchrotron loss. If escape is efficient, the confinement limit should be dominant for electrons when

Table 4.1. Model parameters

Region	$p_{\rm inj}$	L_e [10^{39} erg s^{-1}]	L_B [10^{39} erg s^{-1}]
e1	2.25	0.02	0.18
w1	2.55	0.08	0.06

$E^{\rm con}_{e,\rm max} < E^{\rm syn}_{e,\rm max}$, or,

$$\eta_g > 20 \left(\frac{R}{6\ \rm pc}\right)^2 \left(\frac{B}{16\ \mu\rm G}\right)^3. \tag{4.31}$$

In this case, our results constrain the product $\eta_{\rm acc}\eta_g$ to $\eta_{\rm acc}\eta_g \lesssim 10^3$. Combining this with Eq. (4.31), we obtain $\eta_{\rm acc} \lesssim 10^2$.

The acceleration of leptons may imply the presence of nonthermal protons because they have a larger Larmor radius and are more easily injected into the acceleration processes. Synchrotron losses are inefficient for protons, and the maximum energy is limited by confinement:

$$E^{\rm con}_{p,\rm max} = 5\ \rm PeV \left(\frac{\eta_{\rm acc}\eta_g}{10^2}\right)^{-\frac{1}{2}} \left(\frac{L_B}{10^{38}\ \rm erg\ s^{-1}}\right)^{\frac{1}{2}}. \tag{4.32}$$

If we assume that the same acceleration process is at work both for electrons and protons, we can apply the same value of $\eta_{\rm acc}$. Then, the constraint $\eta_{\rm acc} \lesssim 10^2$ formally suggests that SS433 can accelerate protons beyond a PeV, if the Bohm factor η_g is sufficiently small.

As noted in Sec. 4.3.2, the radio flux may be dominated by other components. If we treat the radio data as upper limits, the parameter $p_{\rm inj}$ can become as small as 1.9. The spectral turnover and cutoff predicted in our model and constraints on $\eta_{\rm acc}$ remain unchanged because they are derived from the hard X-ray data and determined by the timescales of synchrotron cooling $t_{\rm syn}$ and transport $t_{\rm adv}$.

4.4.1 Comparison with Previous Studies

We now compare our results with other recent studies. Our model spectra are significantly different from results by Abeysekara et al. (2018) (e1) and Xing et al. (2019) (w1). They require a hard spectrum of $p_{\rm inj} = 1.9$ for electrons, while we derive $p_{\rm inj} = 2.25$ and 2.55 for e1 and w1, respectively. The main differences are twofold. First, they calculate the evolution of particles for $t_{\rm lifetime} \simeq$30 kyr assuming continuous injection throughout the source lifetime. Thus, their spectra show cooling breaks in the electron spectra at $E_e = 2\ (B/16\ \mu\rm G)^{-2}(t_{\rm lifetime}/30\ \rm kyr)^{-1}$ TeV, and require a hard $p_{\rm inj}$. In contrast, we integrate the particle spectrum from z_s and z_f (Eq. 4.19), and the effective lifetime is set by $t_{\rm adv} \simeq (z_f - z_s)/v_z \simeq$150 yr. Second, while they only include radiative losses, we also consider adiabatic loss. In Fig. 4.3, we compare energy loss timescales for different processes. Adiabatic losses dominate below 100 TeV, significantly limiting the total electron energy. Note that we employ a simple case of a conical jet to evaluate the adiabatic loss. The jets may be collimated by surrounding material and keep nearly cylindrical ($\partial R/\partial z = 0$), experiencing no adiabatic loss. In our calculation, since the effect of particle transport is dominant over that of adiabatic cooling ($t_{\rm adv} < t_{\rm ad}$), the results remain unchanged for different modeling of jet expansion, as long as we focus on the emission from the synchrotron knots.

4.4.2 Prospects for Future Observations

We examine expectations for future observations. The hard X-ray (10–100 keV) observations will be most critical. *NuSTAR* can provide a better determination of the spectrum from both regions in this regime. In the MeV–GeV band, planned telescopes such as *GRAMS* (Aramaki

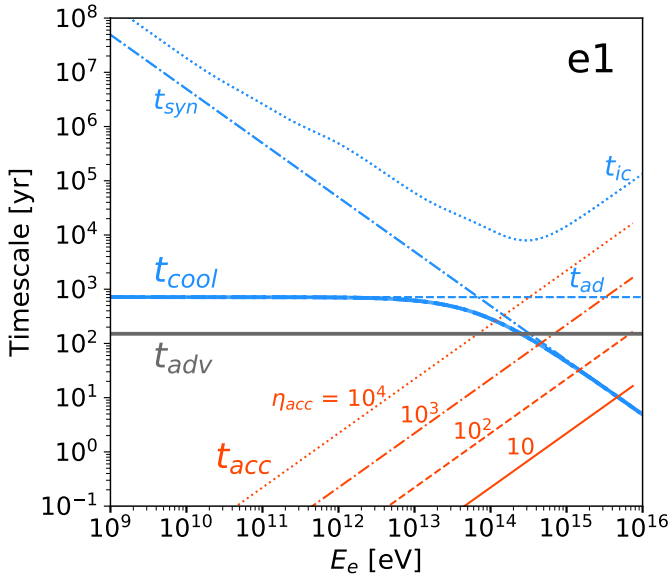

Figure 4.3. Cooling timescales ($t = \gamma/|\dot{\gamma}|$) for different processes for the e1 region, as marked. For comparison, timescales of confinement and acceleration are also shown.

et al., 2020), *e-ASTROGAM* (De Angelis et al., 2017), and AMEGO (McEnery et al., 2019) will be able to study the highest energy synchrotron photons, though the localization of emitting region would be difficult for their expected angular resolutions. Our models predict that these observations would detect spectral turnover and cutoff (Fig. 4.2), placing strong constraints on physical properties and acceleration processes. In the VHE regime, our results indicate that CTA and LHAASO observations might be able to detect γ-rays from both regions (Acharya et al., 2017; Bai et al., 2019).

4.5 Morphology of Emission Regions

The location of emission sites is an important ingredient in our model. In this section, we examine explanations for the size of X-ray knots and briefly discuss uncertainties due to different morphology of the X-ray and IC emission.

4.5.1 X-ray Knot Size in SS433 Jets

The X-ray images in the $\sim$ 1–10 keV range show a clear feature of knots with a size comparable to the e1 region, $s^{\rm X} \simeq$ 5–10 pc (Safi-Harb & Ögelman, 1997). The typical energy of electrons responsible for the X-ray emission at 1 keV is 30 $(B/15\,\mu{\rm G})^{-1/2}$ TeV, and the synchrotron cooling time for these electrons is 1.5 $(B/15\,\mu{\rm G})^{-3/2}$ kyr. The advection length during that is

$$s^{\rm X}_{\rm syn} = 120 \left(\frac{B}{15\,\mu{\rm G}}\right)^{-\frac{3}{2}} \left(\frac{v_z}{0.26c}\right) {\rm pc}\,. \tag{4.33}$$

Thus, with our standard value of $v_z = 0.26c$, the X-ray knot size cannot be explained by the synchrotron cooling. Below, we will examine several possible physical processes that may determine the X-ray knot size.

Synchrotron Cooling: Unlikely. The knot length may be explained by the synchrotron cooling if we adopt a velocity smaller than $0.26c$, but the spectrum places tight constraints; the emitting particles should be in the fast-cooling regime, where photon spectrum would be $\Gamma_{\rm ph} = 2$ (for an E_e^{-2} injection). This contradicts with the hard X-ray spectrum of $\Gamma_{\rm ph} \simeq 1.5$. Thus, synchrotron cooling cannot be responsible for determining the X-ray knot size, unless the electrons are injected with an extremely hard spectrum of $\simeq E_e^{-1}$.

Adiabatic Cooling: Possible for a non-conical jet. If the jet is conical, the adiabatic cooling operates on a scale of the jet length, and the knot size would be $s_{\rm ad} \simeq 3z/2 \simeq 60$ pc, much larger than observed. However, it may experience local expansion or compression due to the pressure from the surrounding material, producing standing coherent waves (called the Mach disk) or more complicated hydrodynamical structures. If the jet has a structure that enhances the adiabatic cooling rate locally, the X-ray knot size could be explained.

Enhanced Magnetic Field: Possible. The magnetic field in the jets may not be distributed uniformly, but have local amplifications probably due to the local compression of the jet or plasma instabilities. The size of the X-ray knot may correspond to the region with an enhanced magnetic field, probably due to turbulence.

Very recent acceleration: Unlikely. There is a theoretical possibility that acceleration has started very recently, Δt years ago, and advection determines the size of knots. We cannot rule out the possibility that Δt is close to $t_{\rm adv}$, but this requires a coincidence. There could also be a possibility that the acceleration takes place in an extended region, rather than at a specific location in the jet, and $\Delta t \ll t_{\rm adv}$. However, if this is the case, the injection power required to produce the observed X-ray luminosity would be much larger than in other scenarios. The dissipation of such a large amount of power would have to produce much brighter thermal bremsstrahlung emission from the heated plasma, which is not observed. Thus, this scenario is unlikely.

Future X-ray observations with high angular resolution would be important to distinguish these scenarios. If the knot size is defined by the adiabatic cooling, we should see no dependence on the photon energies. If the knot size corresponds to the size of the region where the magnetic field is enhanced due to turbulence, we expect patchy bright emission inside the emitting region due to the inhomogeneity of magnetic field strength.

4.5.2 IC Emitter Size in SS433 Jets

The size of γ-ray emitting regions, $s^{\rm VHE}$, is not yet clear. The γ-rays with an energy of 25 TeV are predominately generated on the cosmic microwave background, and the emitting electrons have an energy of 100 TeV. The synchrotron cooling time is $0.5\ (B/15\,\mu{\rm G})^{-3/2}$ kyr, during which these electrons are advected to a distance of

$$s^{\rm VHE}_{\rm syn} = 40\ \left(\frac{B}{15\,\mu{\rm G}}\right)^{-\frac{3}{2}} \left(\frac{v_z}{0.26c}\right)\ {\rm pc}\,. \tag{4.34}$$

Adiabatic losses may produce a comparable advection distance for a conical jet, or smaller distance if they are locally enhanced. In any case, the IC emitter is likely larger than X-ray knots.

The difference between $s^{\rm VHE}$ and $s^{\rm X}$ can induce uncertainties in our calculation. In particular, though we have used the observed VHE flux to derive physical parameter for the

e1 and w1 regions, the real TeV flux from these two knots are likely smaller, provided that $s^{\rm VHE} > s^{\rm X}$. This should primarily affect the estimate on B. Because the dominant target for IC scattering is provided by the diffuse background, synchrotron and IC luminosities relate as $L_{\rm syn}/L_{\rm ic} \propto B^2$, and thus the magnetic field strength may be larger approximately by a factor of $\sqrt{s^{\rm VHE}/s^{\rm X}}$ when we take the size of emitting regions into account. Future CTA observations would better constrain the size of the IC emitter with its unparalleled angular resolution.

4.6 Limitations

In this section, we examine limitations of our model and their impact on our results.

4.6.1 Acceleration Site

We have focused on the case where $z_{\rm acc} = z_s$, but in principle they could be different. If $z_{\rm acc} \ll z_s$, we should take into account the particle cooling during $z_{\rm acc}$ and z_s. In such a situation, the magnetic field at the acceleration site, $B_{\rm acc}$, can also be substantially different from the field at the emission region, $B_{\rm emit}$, which is derived by the spectral fitting. This difference would change our upper limits on $\eta_{\rm acc}$ by a factor of $B_{\rm emit}/B_{\rm acc}$ (see Eq. 4.10). In particular, $B_{\rm acc}$ could be smaller than $B_{\rm emit}$ because otherwise we should see brighter synchrotron emission from the acceleration site. If this is the case, future observations should reveal fainter synchrotron emission from the acceleration site, placing better constraints on the magnetic field there. The difference between $B_{\rm acc}$ and $B_{\rm emit}$ might be the reason why shocks are not yet resolved (Abeysekara et al., 2018).

4.6.2 Velocity in Knot Region

In our calculation, we have used $v_z = 0.26c$, which is determined at the jet base. The bulk velocity in the knot region is less certain from observations, but possibly be smaller than $0.26c$ because knots are located at large distances from the core (Goodall et al., 2011a,b; Monceau-Baroux et al., 2014, 2015; Panferov, 2014, 2017; Bowler & Keppens, 2018). The primarily effect of adopting a smaller bulk velocity would be flattening of the spectrum, because the transition from advection-dominated regime to fast cooling regime would occur at lower energy. This would produce a flat ($\Gamma_{\rm ph} \simeq 2$) X-ray spectrum before a cutoff. In addition, the estimate on the size of the emitting regions would be proportionally changed for a different jet velocity. In other words, a better determination of both the spectrum and morphology in X-ray bands would be critical to constrain the bulk velocity in the knot region.

4.7 Conclusions

Multiwavelength observations of the microquasar SS433 offer the potential for detailed studies on particle acceleration in astrophysical jets. In this Chapter, we first present a theoretical

foundation to interpret nonthermal emission from astrophysical jets quantitatively. We then consider leptonic emission from the X-ray knots in SS433's jets. We use the same datasets as in Abeysekara et al. (2018) and Xing et al. (2019), but treat the particle transport and evolution in the jet in more detail, and produce substantially different predictions.

Our analysis produced three main results. First, leptonic models can explain the radio, X-ray and VHE γ-ray data for both the e1 and w1 regions. However, the GeV data remain unexplained for any reasonable parameter set, which indicates that they are mostly from different regions or mechanisms. Second, the efficiency of particle acceleration should be very high, $\eta_{\rm acc} \lesssim 10^2$, to explain the X-ray and TeV γ-ray data. This could be realized by the diffusive shock acceleration, for a strong confinement case close to the Bohm limit, $\eta_g \sim 1$. Such high efficiency of particle acceleration may imply that SS433 jets can also accelerate protons beyond a PeV. Third, future X-ray/MeV observations would be most critical to constrain models and better understand the acceleration processes. In particular, our models predict a spectral turnover and cutoff in this energy band.

We note that our models have broader implications that can be studied by future observations.

- We have focused on the emission from e1 and w1 throughout this work. Our model can also predict emission from different regions by changing the parameter z_s and z_f in Eq. (4.19), provided that there is no effect of re-acceleration. As sketched in Fig. 4.1 and explained in Sec. 4.2.5 , in regions farther away from the binary, the synchrotron emission has spectral break steeper than expected from the cooling break. Interestingly, a hint of such a steep break is seen from observations of e2 and w2 regions (Safi-Harb & Ögelman, 1997). A better determination of the X-ray spectrum in these regions is the key to test this prediction.
- We have focused on leptonic emission throughout this work. If protons are also accelerated in the jets, they may interact with the ambient medium to produce pionic γ-rays. Since the cooling time for protons, t_{pp}, is long, we may see emission from protons accumulated during the lifetime of SS433's jets, which should extend over much a larger region than X-ray knots. The jet kinetic power $\sim 10^{39}$ erg s^{-1} and system age ~ 30 kyr suggest that the jet has released the total energy of $E_{\rm jet} \sim 10^{51}$ erg. Assuming that 10% of this goes to nonthermal protons between 1 GeV and 1 PeV, and for an E_p^{-2} injection spectrum, the proton energy would be $0.1E_{\rm jet}/\ln(10^6)$, yielding a TeV γ-ray luminosity of $\sim 0.1E_{\rm jet}/(3t_{pp}\ln(10^6))$. Thus, we could expect TeV γ-ray flux of

$$F_\gamma \sim 10^{-13}(n_{\rm gas}/0.2\ {\rm cm}^{-3})\ {\rm erg\ s}^{-1}\ {\rm cm}^{-2}. \tag{4.35}$$

  This could suggest that the hadronic γ-rays from the W50/SS433 system could also be detected at CTA and LHAASO. Furthermore, they may contribute to the VHE flux detected by HAWC, though it requires strong confinement of protons close to the emitting regions.

4.8 Notes Added

After the work is published, there have been two more papers that analyzed the GeV data (Fang et al., 2020; Li et al., 2020). They both argue that previous papers on GeV emission are highly affected by inappropriate treatment of nearby contaminating sources, which make the previous GeV results suspicious. This finding is in agreement with our results that the GeV flux cannot be explained. However, new results by these two papers are in somewhat contradiction each other (in flux, morphology and periodicity) and flux levels in both papers are much brighter than predicted by our knot model. Thus, our arguments that GeV fluxes are dominated by different regions and/or mechanism remain unchanged. Main conclusions from this work is the particle acceleration is unchanged because it is mainly determined by the X-ray and VHE observations.

Very recently, Kimura et al. (2020) showed that hadronic emission can also explain the observed HAWC flux from the eastern part, because there exists a region of filamentary dense gas. Although this possibility is viable for eastern jet, we stress that leptonic emission is the only feasible scenario that can explain VHE emission from both eastern and western knots. This work reached the same conclusion on the particle acceleration efficiency.

Chapter 5

Physical Conditions and Particle Acceleration in the Kiloparsec Jet of Centaurus A

This chapter is based on the paper "Physical Conditions and Particle Acceleration in the Kiloparsec Jet of Centaurus A" by Sudoh T., Khangulyan D., Inoue Y., 2020, published in the Astrophysical Journal Letters, Volume 901, Issue 2, id.L27, 7 pp.

5.1 Introduction to this Chapter

It is widely believed that jets from active galactic nuclei (AGN) are launched by electromagnetic mechanisms near supermassive black holes (SMBHs) (e.g., Blandford & Znajek, 1977; Blandford & Payne, 1982; Komissarov et al., 2007; McKinney et al., 2012). As a result, jets are expected to be initially highly magnetized. The dissipation of the magnetic field converts the Poynting flux into the bulk kinetic energy, accelerating the jet to a relativistic speed. A fraction of the jet power is also transferred to particles, heating the jet material and accelerating particles to nonthermal energies. Particle acceleration can proceed effectively either in a magnetically-dominated (e.g., via magnetic reconnection) or kinetically-dominated (e.g., via formation of shocks) jet (e.g., Sironi et al., 2015). Therefore, to understand the production mechanism of nonthermal particles, the determination of the energy balance in the jets, especially their magnetization, is essential.

Observational studies of energy balance in AGN jets are mostly conducted for blazars, i.e., radio galaxies with their jets aligned toward Earth (e.g., Tavecchio et al., 1998; Celotti & Ghisellini, 2008; Ghisellini et al., 2010; Zhang et al., 2012; Inoue & Tanaka, 2016). These studies typically find relatively weak magnetization. However, they are usually restricted to one-zone treatment aimed to explain observations at various phases. As blazars are highly variable (e.g., Ackermann et al., 2016), it is unclear whether the emission of each phase correctly probes conditions in the large-scale jet. Most blazars are located at cosmological distances, which makes any study beyond one-zone treatment difficult.

The radio galaxy Centaurus A (Cen A) enables invaluable insights on this problem thanks to its unequaled proximity (3.8 Mpc; Harris et al., 2010). Broadband emission from this

object has been resolved over a wide range of spatial scales from the core ($\lesssim 10^{-2}$ pc) to the giant lobes ($\gtrsim 10^5$ pc) (e.g., Kraft et al., 2002; Hardcastle et al., 2006; Kataoka et al., 2006; Goodger et al., 2010). Recently, the H.E.S.S. collaboration has reported evidence of very-high-energy (VHE) γ-rays from the kpc-scale jet in Cen A (Abdalla et al., 2020). A combination of new γ-ray data with previous multi-wavelength data brings new information on jet properties on kpc distances from SMBH.

Here, we study the origin of nonthermal emission and physical conditions of the kpc-jet in Cen A. Our approach is model-independent, meaning that we rely on observational data only. In Sec. 5.2, we summarize observational properties. In Sec. 5.3, we constrain physical conditions in the jet required from X-ray observations. In Sec. 5.4, we further constrain the parameter space with the VHE data. In Sec. 5.5, we study the contributions from hadronic processes. In Sec. 5.6, we summarize our findings.

5.2 Observational Properties

The SMBH at the core of Cen A has a mass of 5.5×10^7 $M_\odot$ measured by stellar kinematics (Cappellari et al., 2009), with corresponding Eddington luminosity of $7 \times 10^{45}\,\mathrm{erg\,s^{-1}}$. It provides an ultimate energy source to the jet, which has an estimated power of $\sim 10^{43}\,\mathrm{erg\,s^{-1}}$(Wykes et al., 2013), an apparent velocity of $\simeq 0.5c$ (Hardcastle et al., 2003) on a hundred-parsec scale, and an opening angle of $10^\circ - 15^\circ$ (e.g., Horiuchi et al., 2006).

On kpc scales, the jet produces diffuse synchrotron emission. Kataoka et al. (2006) utilized *Chandra* data and obtained the X-ray flux along the jet from the core up to about 240″ (4 kpc). The observed 0.5−5 keV luminosity of the diffuse unresolved kpc-scale jet is $L^{\rm D}_{\rm keV} \simeq 8 \times 10^{38}\,\mathrm{erg\,s^{-1}}$, where the superscript D stands for the diffuse component. We define this energy range as the keV band. The spectral index of this component, $\alpha = -d\ln F_\nu / d\ln \nu$, is consistent with $\alpha \simeq 1$.

The jet contains individual knots resolved in X-ray and radio observations (Kraft et al., 2002; Goodger et al., 2010). The number of X-ray knots identified in Kataoka et al. (2006) is about 30. While $\sim 2-5$ of them could be low-mass X-ray binaries unrelated to the jet emission (Goodger et al., 2010), the majority are produced by the jet material (Blandford & Koenigl, 1979; Sanders, 1983; Hardcastle et al., 2003; Mao & Wang, 2007; Bednarek & Banasiński, 2015; Vieyro et al., 2017; Torres-Albà & Bosch-Ramon, 2019). The typical keV-band luminosity of each knot is $L^{\rm K}_{\rm keV} \simeq 10^{37}\,\mathrm{erg\,s^{-1}}$, where the superscript K stands for knots. The X-ray spectral indices are consistent with $\alpha \simeq 0.5-1$ (Goodger et al., 2010; Tanada et al., 2019b). For some knots, the spectral indices in radio band (4.8−8.4 GHz) are also measured, in the range of $\alpha \simeq 0.5-2$, although uncertainties are large (Goodger et al., 2010).

The sizes of knots are constrained only for some of the brightest ones, typically $\simeq 2-10$ pc (Tingay & Lenc, 2009; Goodger et al., 2010; Tanada et al., 2019b). The magnetic fields in the knots are also largely unconstrained. For two bright knots, BX2 and AX1C, *Chandra* observations suggest upper limits of $B \lesssim 80$ μG due to the absence of spectral steepening expected for synchrotron cooling (Snios et al., 2019).

The production of synchrotron emission in the energy of $\epsilon = 1\epsilon_1$ keV implies the presence of electrons with energies of $E_e \simeq 10\epsilon_1^{1/2} B_{100}^{-1/2}$ TeV, where $B = 100 B_{100}$ μG is the magnetic field strength. The same population of electrons produces γ-rays by inverse Compton (IC)

Table 5.1. Luminosity of the host galaxy NGC 5128

Band	Wavelength [μm]	Luminosity [erg s^{-1}]
optical	0.6	$\sim 9\times10^{43}$
near-IR	2	$\sim 6\times10^{43}$
mid-IR	25	$\sim 0.6\times10^{43}$
far-IR	100	$\sim 2\times10^{43}$

scattering. If the scattering proceeds in the Thomson regime, the characteristic γ-ray energy is

$$\epsilon_{\rm ic} = 300 \left(\frac{\hbar\omega_0}{6\times10^{-4}\,{\rm eV}}\right)\left(\frac{E_e}{10\,{\rm TeV}}\right)^2 \ {\rm GeV}, \tag{5.1}$$

where $\hbar\omega_0$ is the energy of target photons and the Thomson limit is valid for $\hbar\omega_0 \ll 0.1\,(E_e/10\,{\rm TeV})^{-1}$ eV. The recent H.E.S.S. analysis has confirmed that VHE emission is produced in the kpc-jet (Abdalla et al., 2020). The flux is approximately 2×10^{-10} GeV cm^{-2} s^{-1} at $\epsilon_{\rm ic} \simeq 300$ GeV and the spectrum is fit by a power-law with $\alpha \simeq 1.5$ up to ~ 10 TeV (H. E. S. S. Collaboration et al., 2018). Thus, the luminosity in the VHE band, which we define as 0.3−3 TeV, is $L_{\rm VHE} \simeq 7\times10^{38}\,{\rm erg\,s^{-1}}$.

The target photon fields may be produced by the jet itself, objects in it, and external sources. The host galaxy provides the brightest external soft photons in optical and infrared. Table 5.1 shows their characteristics taken from NASA/IPAC Extragalactic Database. Note that soft photons with shorter wavelengths are affected by Klein–Nishina suppression. For example, for an electron spectrum of $dN_e/dE_e \propto E_e^{-3}$, the contributions from optical and near-IR are smaller than that of far-IR above $\epsilon_{\rm ic} \simeq 100$ GeV, despite the higher luminosities. The nucleus of Cen A could also provide target photons with a bolometric luminosity of $\sim 10^{43}\,{\rm erg\,s^{-1}}$ (Chiaberge et al., 2001; Beckmann et al., 2011).

Although γ-rays can be produced also by hadronic processes, their contributions are likely small (Section 5.5). In Sections 5.3-5.4, we assume that VHE γ-rays are predominately generated by leptons .

5.3 Constraints from X-ray data

5.3.1 Jet Energy Balance

The average physical conditions in the jet are determined by its basic properties. We assume that the kpc jet is cylindrical with a radius R and height $Z = 3Z_3$ kpc, starting from a distance of 1 kpc from the core. We use an opening angle of $\theta = 0.2\theta_{0.2}$ rad, which results in $R = 200\theta_{0.2}$ pc. This might appear an overestimate for the radius at 1 kpc (e.g., Wykes et al., 2019). However, for our cylindrical approximation, it would be appropriate as the mean radius of the kpc jet. We assume a total jet power of $P_{\rm jet} = 10^{43}P_{43}\,{\rm erg\,s^{-1}}$. The energy flux in the jet is

$$\frac{P_{\rm jet}}{\pi R^2} \simeq 8\,P_{43}\theta_{0.2}^{-2}\ {\rm erg\,s^{-1}\,cm^{-2}}\,. \tag{5.2}$$

The jet bulk speed, $\beta = 0.5\beta_{0.5}$, defines the energy density

$$w_{\rm jet} = \frac{P_{\rm jet}}{\pi R^2 \beta c} \simeq 350\, P_{43}\theta_{0.2}^{-2}\beta_{0.5}^{-1}\ {\rm eV\ cm^{-3}}\,, \tag{5.3}$$

which is distributed to thermal gas, magnetic field, and nonthermal protons and electrons, such that

$$w_{\rm Th} + w_{\rm B} + w_{e,{\rm NT}} + w_{p,{\rm NT}} = w_{\rm jet}\,. \tag{5.4}$$

We define the corresponding fractions, $\eta_i = w_i/w_{\rm jet}$:

$$\eta_{\rm Th} + \eta_{\rm B} + \eta_{e,{\rm NT}} + \eta_{p,{\rm NT}} = 1\,. \tag{5.5}$$

The magnetic energy density,

$$w_{\rm B} = \frac{B^2}{8\pi} = \eta_{\rm B} w_{\rm jet}\,, \tag{5.6}$$

converts to the strength of the magnetic field [*1]:

$$B = \sqrt{\frac{8\pi\eta_{\rm B}P_j}{\pi R^2\beta c}} = 120\sqrt{\frac{\eta_{\rm B}P_{43}}{\beta_{0.5}}}\theta_{0.2}^{-1}\ \mu{\rm G}\,. \tag{5.7}$$

The energy distribution for nonthermal particles is often approximated with a broken power law:

$$\frac{dn_Y}{dEdV} = \begin{cases} A_Y\,(E/E_{Y,{\rm br}})^{-p_{Y,H}} & E \geq E_{Y,{\rm br}}\,, \\ A_Y\,(E/E_{Y,{\rm br}})^{-p_{Y,L}} & E_{Y,\min} < E \leq E_{Y,{\rm br}}\,. \end{cases} \tag{5.8}$$

Here Y denotes the particle type, $p_{Y,L}$ and $p_{Y,H}$ define power-law slopes, $E_{Y,{\rm br}}$ is the break energy, A_Y is the normalization, and $E_{Y,\min}$ is the minimum energy of the nonthermal distribution. The energy density in nonthermal particles is

$$w_{Y,{\rm NT}} = \int_{E_{Y,\min}}^{\infty} \frac{dn_Y}{dEdV} E dE\,. \tag{5.9}$$

For electrons, radio-emitting particles typically have low energies ($E_e < E_{e,{\rm br}}$), while X-ray emitting particles have high energies ($E_e > E_{e,{\rm br}}$). Therefore, the energy content in nonthermal electrons that produce emission in the keV-band is

$$w_{e,{\rm keV}} = A_e \int_{\sqrt{0.5}E_{e,{\rm keV}}}^{\sqrt{5}E_{e,{\rm keV}}} \left(\frac{E}{E_{e,{\rm br}}}\right)^{-p_{e,H}} E dE\,, \tag{5.10}$$

where $E_{e,{\rm keV}}$ is the energy of electrons which are responsible for the production of 1 keV synchrotron photons: $E_{e,{\rm keV}} \simeq 10\,(B/100\ \mu{\rm G})^{-1/2}$ TeV. It is useful to define another parameter,

$$\chi_{\rm keV} = \frac{w_{e,{\rm keV}}}{w_{e,{\rm NT}}} = \frac{\eta_{e,{\rm keV}}}{\eta_{e,{\rm NT}}}, \tag{5.11}$$

which is determined by the electron spectrum.

[*1] Note that this equation for the magnetic field is different from the expression in the previous Chapter by a factor of 2. This is because we here define η_B based on the energy density in the comoving frame, while in the previous Chapter it is defined based on the energy flux in the lab frame.

5.3.2 X-ray Emission from the Jet

X-ray observations of Cen A revealed both diffuse unresolved emission and many compact knots in the kpc jet. The diffuse jet luminosity in the keV band is $L^{\rm D}_{\rm keV} \simeq 8\times10^{38}$ erg s^{-1} (Kataoka et al., 2006), and the volume is $V^{\rm D} \simeq \pi R^2 Z \simeq 10^{64}\theta^2_{0.2}Z_3\,{\rm cm}^3$. The luminosity density, $j = L/V$, of the diffuse jet is

$$j^{\rm D}_{\rm keV} = 7\times10^{-26}\theta^{-2}_{0.2}Z_3^{-1}\,{\rm erg\,s^{-1}cm^{-3}} \tag{5.12}$$

The compact knots have a typical keV-band luminosity of $L^{\rm K}_{\rm keV} = 10^{37}L_{37}\,{\rm erg\,s^{-1}}$. We adopt a characteristic knot size of $r = 5r_5$ pc and assume that knots are spherical. Then, the typical volume is $V^{\rm K} = 2\times10^{58}r_5^3\,{\rm cm}^3$. The luminosity density of the knot radiation is

$$j^{\rm K}_{\rm keV} = 6\times10^{-22}r_5^{-3}L_{37}\,{\rm erg\,s^{-1}cm^{-3}}\,. \tag{5.13}$$

These luminosities are determined by the energy content in keV-emitting electrons and their synchrotron cooling time,

$$t_{\rm syn} \simeq 2\times10^2\left(\frac{\hbar\omega}{1\,{\rm keV}}\right)^{-1/2}\left(\frac{w_{\rm B}}{100\,{\rm eV\,cm^{-3}}}\right)^{-3/4}{\rm yr}\,, \tag{5.14}$$

where $\hbar\omega$ is the synchrotron emission energy. By equating $j_{\rm keV}$ with $w_{e,{\rm keV}}/t_{\rm syn}$, we obtain the following constraints on the production sites of synchrotron emission:

$$(\eta^{\rm D}_{\rm B})^{3/4}\eta^{\rm D}_{e,{\rm keV}} \simeq 3\times10^{-7}\theta^{3/2}_{0.2}Z_3^{-1}\beta^{7/4}_{0.5}P_{43}^{-7/4} \tag{5.15}$$

and

$$(\eta^{\rm K}_{\rm B})^{3/4}\eta^{\rm K}_{e,{\rm keV}}r_5^3 \simeq 3\times10^{-3}L_{37}\theta^{7/2}_{0.2}\beta^{7/4}_{0.5}P_{43}^{-7/4}\,. \tag{5.16}$$

To relate $\eta_{e,{\rm keV}}$ to $\eta_{e,{\rm NT}}$, we need the electron spectrum. In general, the ratio of these two, $\chi_{\rm keV}$, is larger for a harder spectrum. For the diffuse jet, Hardcastle & Croston (2011) derived $p_{e,L} \simeq 2.06$ for radio-emitting electrons and a very steep spectrum for X-ray emitting particles, $p_{e,H} \simeq 3.88$ and $E_{e,{\rm br}} \sim 10^{-1.5}E_{e,{\rm keV}}$, based on multi-wavelength data (Hardcastle et al., 2006). If we assume $E_{e,{\rm min}} \sim 10^{-3}E_{e,{\rm br}}$, these values convert to $\chi^{\rm D}_{\rm keV} \sim 10^{-4}$. We note that this spectrum is obtained from about 2−4 arcmin (2−4 kpc) from the core. Closer to the core, the X-ray spectrum may be harder. Indeed, the X-ray spectrum derived in Kataoka et al. (2006) for the 1−2 kpc jet yields $p_{e,H} \simeq 3.0-3.4$, resulting in $\chi^{\rm D}_{\rm keV} \sim 10^{-3}$. Therefore, the value of $\chi^{\rm D}_{\rm keV}$ averaged over the kpc-jet is likely larger than 10^{-4}. Utilizing this, we rewrite Eq. (5.15) as

$$(\eta^{\rm D}_{\rm B})^{3/4}\eta^{\rm D}_{e,{\rm NT}} \simeq 3\times10^{-3}\theta^{3/2}_{0.2}Z_3^{-1}\beta^{7/4}_{0.5}P_{43}^{-7/4}\chi_{-4}^{-1}, \tag{5.17}$$

where $\chi_{-4} = \chi^{\rm D}_{\rm keV}/10^{-4}$. We constrain the jet parameters by limiting the sum of nonthermal electron and magnetic energy, $\eta^{\rm D}_{\rm B} + \eta^{\rm D}_{e,{\rm NT}} < 1$. Figure 5.1 shows this sum under the above constraint (Eq. 5.17) as a function of $\eta^{\rm D}_{\rm B}$. This shows that a wide range of $\eta^{\rm D}_{\rm B}$ and $\eta^{\rm D}_{e,{\rm NT}}$ is allowed from the X-ray data.

The spectral properties of knots are less tightly constrained from observations and may differ from one to another. However, observed X-ray fluxes can place useful constraints. To

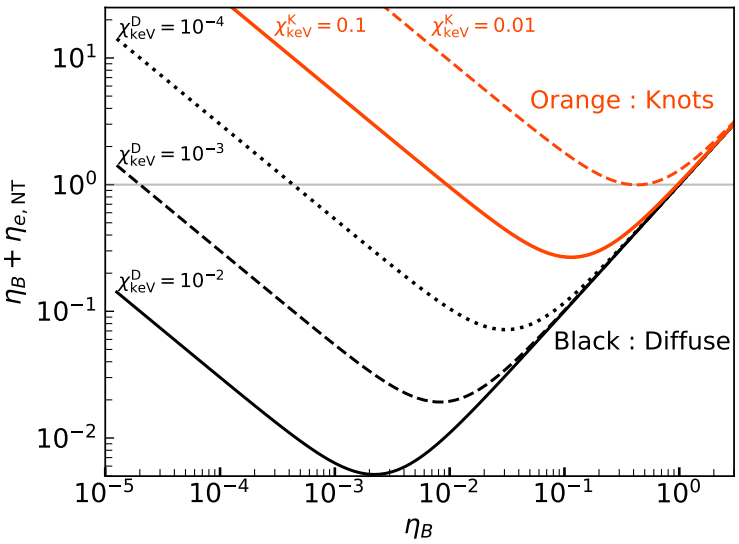

Figure 5.1. The sum of nonthermal electron and magnetic energy as a function of $\eta_{\rm B}$, under the constraints from X-ray observation: Eq. (5.17) for the diffuse jet and Eq. (5.18) for the knots. This sum cannot (significantly) exceed one, which constrains these parameters.

illustrate this, we write Eq. (5.16) as

$$(\eta_{\rm B}^{\rm K})^{3/4}\eta_{e,\rm NT}^{\rm K} \simeq 3\times10^{-2} L_{37}\theta_{0.2}^{7/2}\beta_{0.5}^{7/4}P_{43}^{-7/4}r_5^{-3}\chi_{-1}^{-1}\,, \tag{5.18}$$

where $\chi_{-1} = \chi^{\rm K}_{\rm keV}/10^{-1}$. Figure 5.1 also shows $\eta_{\rm B}^{\rm K}+\eta_{e,\rm NT}^{\rm K}$ under the above constraint. Because this sum should not significantly exceed one, we obtain $\chi^{\rm K}_{\rm keV} \gtrsim 0.01$. This places tight constraints on the spectrum. If we use $p_{e,L} \simeq 2.3$ as an example, then $E_{e,\rm keV}$ should be nearly equal to (or smaller than) $E_{e,\rm br}$ to satisfy this constraint. If we instead use $p_{e,L} \simeq 2.06$ as derived for the diffuse jet, $E_{e,\rm keV}$ still need be relatively close to the break: $E_{e,\rm keV} \lesssim 10\ E_{e,\rm br}$. In the latter case, $\chi^{\rm K}_{\rm keV}$ can be as high as 0.1.

5.3.3 Conditions in the Jet

X-ray observations allow three distinct scenarios for the physical conditions in the diffuse jet.

(i) Strongly magnetized, $\eta_{\rm B}^{\rm D} \sim 1$
(ii) nonthermal electron dominant, $\eta_{e,\rm NT}^{\rm D} \sim 1$
(iii) Thermal plasma dominant, $\eta_{\rm Th}^{\rm D} \sim 1$

Case (i): If the entire jet is strongly magnetized, the knot would also have a high magnetization, $\eta_{\rm B}^{\rm K} \sim 1$. The large difference in luminosity densities would be due to higher electron energy densities in the knots, implying efficient particle (re-)acceleration taking place there.

Case (ii): If the jet total energy is mostly carried by nonthermal electrons, the diffuse jet should be very weakly magnetized: $\eta_{\rm B}^{\rm D} \sim 4\times10^{-4}\ (\chi_{-4})^{-4/3}$ (Eq. 5.17). In this case,

amplification of the magnetic field would be needed to explain the compact knots.

Case (iii): If the bulk of the jet energy is carried by thermal particles, the jet magnetization would be relatively weak because $\eta_{\rm B}^{\rm D} + \eta_{e,{\rm NT}}^{\rm D} \ll 1$. In the knot region, we would expect larger values of $\eta_{\rm B}^{\rm K}$ and $\eta_{e,{\rm NT}}^{\rm K}$, but the thermal particles should still have most of the energy there. A plausible realization of such a scenario is equipartition between the magnetic field and the nonthermal electrons, $\eta_{\rm B}^{\rm K} \simeq \eta_{e,{\rm NT}}^{\rm K}$, which minimizes the energy requirement for these two components.

Next, we show that only case (iii) is allowed by the VHE data.

5.4 Further Constraints from VHE data

5.4.1 VHE Emission from the Jet

Here, we combine X-ray and γ-ray data to further constrain the jet properties. To do so, we note that X- and γ-ray instruments have different angular resolution. In particular, the VHE flux includes contributions both from the jet and counter-jet. The emission from the counter-jet is Doppler de-boosted by a relative factor of $(\mathcal{D}_{\rm cj}/\mathcal{D})^2$ (see, e.g., Khangulyan et al., 2018a). Here $\mathcal{D}_{\rm cj} = 1/(\Gamma(1-\beta\cos(\pi-\theta_{\rm obs})))$ and $\mathcal{D} = 1/(\Gamma(1-\beta\cos\theta_{\rm obs}))$ are the Doppler factors for the counter-jet and jet, respectively. The bulk Lorentz factor, $\Gamma = 1/\sqrt{1-\beta^2}$, is assumed to be common and $\theta_{\rm obs}$ is the angle between the line-of-sight and the jet velocity. The Doppler de-boosting is significant, ranging between 0.07 and 0.3 for feasible viewing angles of $20^\circ - 50^\circ$ (Tingay et al., 1998; Hardcastle et al., 2003, see also Appendix. C.1).

However, the counter-jet VHE emission can be still important since IC may proceed there at a more favorable scattering angle. Below, we formally ignore the contribution from the counter-jet and use an isotropic approximation for the target photons. If they are indeed isotropic, we overestimate the VHE emission from the jet by the factor of $1 + (\mathcal{D}_{\rm cj}/\mathcal{D})^2$, i.e., our estimate will be accurate within a factor of 1.3.

The photon field may instead originate in the core region. Then, for a power-law distribution of electrons with index p emitting in the Thomson regime, the flux is reduced compared to the isotropic case by a factor of $A(\theta) = (1-\cos\theta)^{p+1/2}$ (see, e.g., Khangulyan et al., 2018a, here for simplicity we adopted the scattering at the angle of 90° as an estimate for the isotropic case). In such a case, the emission from the jet is strongly suppressed and the VHE emission is produced in the counter-jet. Then we underestimate the total VHE emission from the jet by a factor of $A(\theta_{\rm obs}) + A(\pi-\theta_{\rm obs})(\mathcal{D}_{\rm cj}/\mathcal{D})^2$. For a cooled electron spectrum, $p = 3$, this yields 0.3 and 0.9 for the viewing angle of 20° and 50°, respectively.

The above estimates indicate that our simple consideration is accurate within a factor of 3 independently of the angular distribution of the photons, leaving us with the target energy density, $w_{\rm ph}$, as the only parameter for our estimates.

We assume that the VHE emission is produced by IC scattering in the Thomson regime, which is valid if the target photon is dominantly provided by far-IR radiation. The observed keV and VHE luminosity relates as $L_{\rm keV}/L_{\rm VHE} = w_{\rm B}/w_{\rm ph}$. Therefore, the following conditions

are required, depending on the production site of VHE emission:

$$\begin{aligned} w_{\rm ph} &= \frac{L_{\rm VHE}}{L^{\rm D}_{\rm keV}} w^{\rm D}_{\rm B} \simeq w^{\rm D}_{\rm B} \text{ (diffuse jet)}, \\ w_{\rm ph} &= \frac{L_{\rm VHE}}{N L^{\rm K}_{\rm keV}} w^{\rm K}_{\rm B} \simeq 2 w^{\rm K}_{\rm B} \text{ (knots)}, \end{aligned} \tag{5.19}$$

where $N(\simeq 30)$ is the number of knots.

Since knots have much higher synchrotron luminosity density than the diffuse jet, we would naturally expect $w^{\rm K}_{\rm B} \geq w^{\rm D}_{\rm B}$. Then, if VHE emission is dominated by knots, they should have locally enhanced photon fields. To be relevant, the knot additional photon field should have an energy density comparable to that of the magnetic field. The luminosity should be

$$\begin{aligned} L^{\rm add}_{\rm ph} &= 4\pi r^2 c w^{\rm K}_{\rm B} \,, \\ &\simeq 5 \times 10^{40} \eta^{\rm K}_{\rm B} r_5^2 P_{43} \theta_{0.2}^{-2} \beta_{0.5}^{-1} \,{\rm erg\,s^{-1}} \,. \end{aligned} \tag{5.20}$$

Since the knot magnetic field is $\eta^{\rm K}_{\rm B} \gtrsim 10^{-2}$ from X-ray observation (Figure 5.1), a luminous photon source brighter than 5×10^{38} erg s^{-1} would be needed. This is much brighter than the X-ray luminosity of each knot, which indicates that synchrotron self-Compton cannot be sufficient. In principle, luminous stars could provide this photon field, but in that case, the production of VHE should proceed in the Klein-Nishina regime, significantly decreasing the efficiency of the IC process. Therefore, we regard this possibility as unlikely and consider the diffuse jet as the origin of the VHE emission.

If the target photons are generated inside the jet, the required photon luminosity is

$$\pi R Z c w_{\rm ph} = 3 \times 10^{44} \eta^{\rm D}_{\rm B} \frac{P_{43} Z_3}{\theta^2_{0.2}} \,{\rm erg\,s^{-1}} \,. \tag{5.21}$$

This scenario necessitates a relatively small jet magnetization, $\eta^{\rm D}_{\rm B} \lesssim 0.03$, because otherwise the required luminosity would exceed the total jet power. The required luminosity can be decreased by a factor of $R/Z \sim 0.2$, if we assume that the target photons are strongly beamed along the jet axis (e.g., if emitted by the highly relativistic inner jet, see Bednarek, 2019), but this still requires $\eta^{\rm D}_{\rm B}$ well below 0.1.

If the soft photons are supplied from external sources, the luminosity should be

$$w_{\rm ph} 4\pi d^2 c = 2 \times 10^{45} \eta^{\rm D}_{\rm B} \frac{P_{43} d_1^2}{\theta^2_{0.2} \beta_{0.5}} \,{\rm erg\,s^{-1}} \tag{5.22}$$

where $d = 1 d_1$ kpc is the distance from the emitting region to the source of soft photons. We note that the use of a single parameter d is a simplification, because external photon sources (starlight and dust) are spatially extended. A more realistic calculation by Stawarz et al. (2006) finds an energy density of $\sim 10^{-11}$ erg cm^{-3} from stars in the kpc-jet (see their Figure 2), consistent with $d \sim 1$ kpc in our estimate. This scenario necessitates a relatively small jet magnetization, $\eta^{\rm D}_{\rm B} \lesssim 0.03$, because otherwise the luminosity of the host galaxy would not be sufficient.

Both internal and external sources of target photons require $\eta^{\rm D}_{\rm B} < 0.03$. This excludes the possibility of a strongly magnetized jet (case i). Figure 5.2 shows the jet magnetization parameter in the diffuse jet as a function of the photon energy density. It also shows that the jet magnetization should satisfy $\eta^{\rm D}_{\rm B} \gtrsim 10^{-3}$, because otherwise the emission produced on

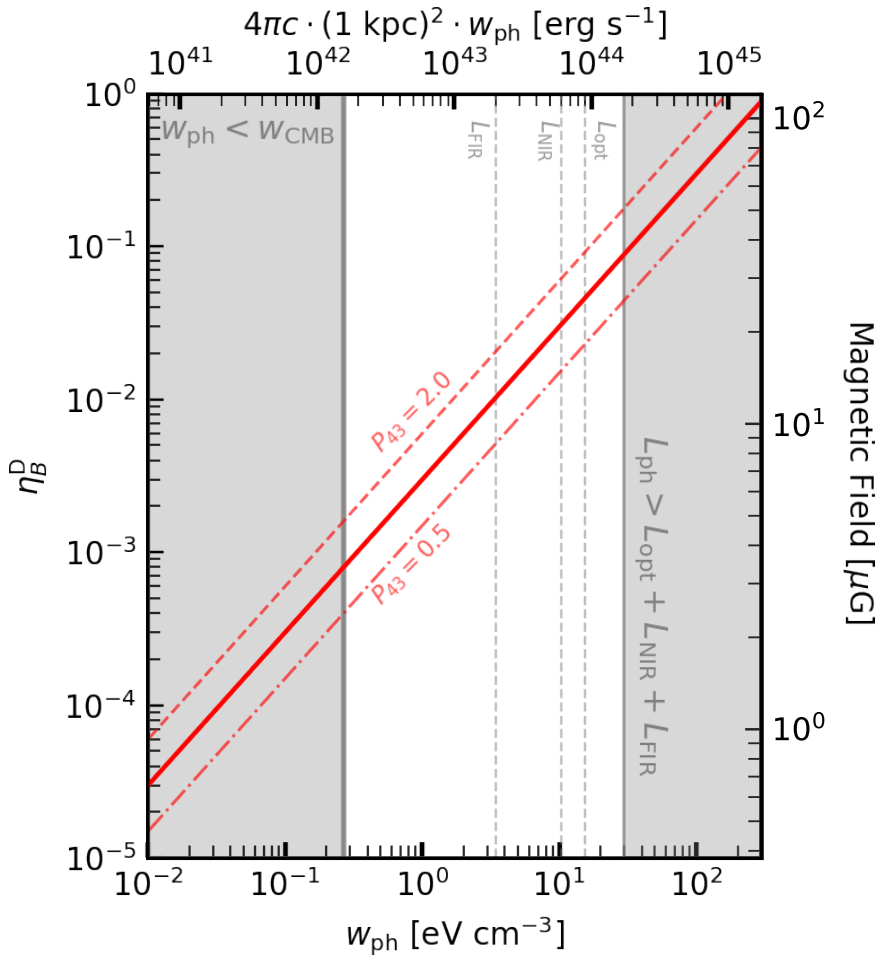

Figure 5.2. Jet magnetization that is required for explaining VHE emission, as a function of soft photon energy density. The solid line adopts $P_{43} = 1$, while other two lines show the cases when P_{43} is changed to 2 (dashed) and 0.5 (dot-dashed). Other model parameters are fixed to the value as adopted in the main text.

the cosmic microwave background radiation would be brighter than observed. This excludes the case of a very weakly magnetized jet (case ii). Adopting a luminosity of $\simeq 10^{44}$ erg s^{-1}, we find $\eta_{\mathrm{B}}^{\mathrm{D}} \simeq 5\%$ and $\eta_{e,\mathrm{NT}}^{\mathrm{D}} \simeq 3\%$. We conclude that the thermal plasma dominates the jet energetics (case iii).

Thus far, we have shown that thermal particles carry most of the energy in the diffuse jet. It may not seem straightforward to relate this with the energetics in knots, because they locally have very different conditions. However, considering that knots are likely produced by the same material that composes the diffuse jet, in which nonthermal electrons and magnetic field make only $\simeq 8\%$ of the energy in total, thermal plasma is likely dominant also in the

knot regions. In principle, we cannot rule out a possibility that magnetic fields are amplified to $\eta_{\rm B}^{\rm K} \simeq \eta_{\rm Th}^{\rm K}$, but it would require very efficient conversion of thermal energy to the magnetic field. A more feasible scenario is to keep most of the energy in thermal particles in the knot region by minimizing $\eta_{\rm B}^{\rm K} + \eta_{e,{\rm NT}}^{\rm K}$ (i.e., equipartition), with $\eta_{\rm B}^{\rm K}$ and $\eta_{e,{\rm NT}}^{\rm K}$ amplified by a factor of $\mathcal{O}(1)$ compared to the diffuse jet. This argument favors $\eta_{\rm B}^{\rm K} \simeq \eta_{e,{\rm NT}}^{\rm K} \sim 0.1$ (see Fig. 5.1). This results in a relatively weak magnetic field, $B^{\rm K} \sim 40$ μG, consistent with the observed upper limits for two bright knots ($B^{\rm K} < 80$ μG; Snios et al., 2019).

5.4.2 Implications for Particle Acceleration

The dominance of thermal particles implies a relatively small magnetic field even in the knot region. Particles produced in knots can travel a distance of

$$\begin{aligned} r_{\rm syn} &= c\beta t_{\rm syn}^{\rm K}\,, \\ &\simeq 60 \left(\frac{\hbar\omega}{1\,{\rm keV}}\right)^{-1/2} \left(\frac{\eta_{\rm B}^{\rm K}}{0.1}\right)^{-3/4} P_{43}^{-3/4}\theta_{0.2}^{3/2}\beta_{0.5}^{7/4}\,{\rm pc}\,. \end{aligned} \tag{5.23}$$

before losing energy to the synchrotron cooling. This is significantly larger than typical knot size, which indicates that they escape from the knots and contribute to the diffuse emission. The electron power supplied by escaping particles from each knot is $L_{\rm keV}^{\rm K} t_{\rm syn}^{\rm K}/t_{\rm adv}^{\rm K}$, where $t_{\rm adv}^{\rm K} = r/\beta c$ is the advection time in the knot. They would cool down in the diffuse jet, radiating with an X-ray luminosity of

$$\begin{aligned} L_{\rm keV} &\sim \frac{\xi}{2} N L_{\rm keV}^{\rm K} \frac{t_{\rm syn}^{\rm K}}{t_{\rm adv}^{\rm K}} \\ &\sim 90 L_{\rm keV}^{\rm K} \left(\frac{\xi}{0.5}\right)\left(\frac{N}{30}\right) P_{43}^{-3/4} r_5^{-1} \beta_{0.5}^{7/4}\theta_{0.2}^{3/2} \\ &\sim 9\times 10^{38}\ {\rm erg\,s^{-1}}\,, \end{aligned} \tag{5.24}$$

where 1/2 roughly accounts for the synchrotron and IC cooling. The parameter ξ takes the difference in magnetic fields between diffuse jet and knots: since $E_{e,{\rm keV}} \propto (\eta_B)^{-1/4}$, the energy in keV-emitting electrons differ by a factor of $\xi \sim (\eta_B^{\rm K}/\eta_B^{\rm D})^{(2-p_H)/4} \sim 0.5$. This estimate is remarkably close to the diffuse luminosity, suggesting that the particles accelerated in the compact knots may play an essential role in producing the jet diffuse emission.

5.5 Hadronic Scenario

Here, we assess the contribution of hadronic processes to the observed VHE emission. We assume that a sub-volume $\mathcal{V}$ of the jet produces γ-rays via pp interactions. The total energy in nonthermal protons in this region is

$$\begin{aligned} W_{p,{\rm NT}} &= w_{\rm jet}\eta_{p,{\rm NT}}\mathcal{V}\,, \\ &\simeq 6\times 10^{54}\eta_{p,{\rm NT}} P_{43} Z_3 \beta_{0.5}^{-1} f_{\rm V}\ {\rm erg}\,, \end{aligned} \tag{5.25}$$

where $f_{\rm V} = \mathcal{V}/V_{\rm jet}$ is the filling factor of the production sites. These protons produce VHE γ-rays on a timescale of $t_{pp} = 10^{15} n^{-1}$ s, where n is the gas density in the cgs unit. The

luminosity is then

$$\begin{aligned} L_{\rm VHE,}pp &\sim \kappa \frac{\chi_{\rm TeV} W_{p,\rm NT}}{t_{pp}} \,, \\ &\sim 10^{39} \eta_{p,\rm NT} n f_{\rm V} P_{43} Z_3 \beta_{0.5}^{-1} \ {\rm erg\,s^{-1}} \,, \end{aligned} \tag{5.26}$$

where $\chi_{\rm TeV} W_{p,\rm NT}$ is the energy of nonthermal protons in the TeV regime and $\kappa \sim 0.17$ is the fraction of the proton energy converted into γ-rays. To explain the observed luminosity, $7 \times 10^{38}\,{\rm erg\,s^{-1}}$, the target density should be very high:

$$n f_{\rm V} \sim 70 \left(\frac{\eta_{p,\rm NT}}{0.1}\right)^{-1} \left(\frac{\chi_{\rm TeV}}{0.1}\right)^{-1} P_{43}^{-1} Z_3^{-1} \beta_{0.5} \ {\rm cm^{-3}}. \tag{5.27}$$

If the target gas were involved with the jet motion, the kinetic energy flux would significantly exceed the total jet energy flux (Eq. 5.2):

$$\begin{aligned} F_{\rm gas} &= (\Gamma - 1)\, m_p c^2 n f_{\rm V} \beta c \\ &\simeq 3 \times 10^6 f_{\rm V} n \ {\rm erg\,s^{-1}\,cm^{-2}}, \end{aligned} \tag{5.28}$$

Therefore, it is difficult to explain the observed VHE emission by hadronic emission alone. However, some contributions may be possible from the γ-ray production on dense external cloud or stellar winds (Barkov et al., 2010, 2012).

5.6 Conclusion

In this Chapter, we study the origin of nonthermal emission and physical conditions in the kpc-jet of Cen A. By combining X-ray and VHE data, we determine the jet magnetization to be $\eta_{\rm B}^{\rm D} \sim 10^{-2}$ in the kpc-jet. This result is consistent with a recent study on FR II radio galaxies (Sikora et al., 2020). In knot regions, the energy densities in the magnetic field and nonthermal electrons should be amplified to an equipartition value, $\eta_{\rm B}^{\rm K} \simeq \eta_{e,\rm NT}^{\rm K} \sim 0.1$. Such a weak magnetic field implies that most particles leave knots uncooled. We find that it remains viable that entire jet X-ray and VHE emission is produced by particles that are accelerated at and escaped from knots. More detailed modeling will test this scenario.

Chapter 6

Conclusions

In this thesis, we have explored theoretical insights into the nonthermal universe based on recent observations of VHE particles. In particular, we have studied the following four topics:

- **TeV Halos:** We have examined the importance of TeV halos for the first time theoretically. We use standard methods for pulsar population synthesis and assume a model where the TeV halo luminosity is calculated based on Geminga observations but introduces the age dependence of halo formation phenomenologically. Our analysis shows that TeV halos could be one of the most important source classes in future TeV γ-ray surveys, dominating the source counts and diffuse Galactic emission. We also show that the HGPS catalog might contain many TeV halos. Moreover, we find that TeV halos observations can constrain the distribution of the initial pulsar spin period. Current 2HWC data allow a wide range of values, 50 ms $\lesssim \langle P_0 \rangle \lesssim$ 300 ms, but recent 3HWC data suggest that further studies will place tighter constraints.
- **MSPs and Radio-SFR Correlation:** We have pointed out, for the first time, that MSPs can significantly contribute to the radio flux in quiescent galaxies, modifying the low-end tail of the radio-SFR correlation. We analyze the LOFAR data, finding that including an MSP contribution significantly improves the fit, explaining the observed excess in low-SFR and high-mass galaxies. Additionally, we point out the possible effects of systematic uncertainties in the SFR measurements and discuss future ways to test our scenario and implications.
- **SS433:** We have theoretically studied implications from multiwavelength observations of the microquasar SS433. We treat the particle transport and evolution in the jet in more detail than in previous studies (Abeysekara et al., 2018; Xing et al., 2019). We show, for the first time for both the e1 and w1 regions, that leptonic models can explain the radio, X-ray, and VHE γ-ray data. We suggest that GeV data have a different origin, which is partly supported by the latest observations. We further quantify the efficiency of particle acceleration, finding that it should be very high, $\eta_{\rm acc} \lesssim 10^2$. This could be realized by the diffusive shock acceleration for a strong confinement case close to the Bohm limit. Such high efficiency of particle acceleration suggests that SS433 jets can also accelerate protons beyond a PeV. Future X-ray and MeV observations would be critical to test our models.
- **Centaurus A:** We have studied the physical conditions and particle acceleration mechanism in the kpc-scale jets of Cen A. By combining X-ray and VHE data, we determine

the jet magnetization to be $\eta_{\rm B}^{\rm D} \sim 10^{-2}$ in the kpc-jet. For knot regions, we suggest a scenario where the energy densities in the magnetic field and nonthermal electrons should be amplified to an equipartition value, which is sufficiently weak to allow nonthermal particles to remain uncooled before they leave knots. We show that the entire kpc-scale jet X-ray and VHE emission may be produced by particles that are accelerated at and escaped from knots. Finally, we show that hadronic emission very unlikely is relevant for the observed VHE data.

This thesis highlights the importance of VHE observations for our understanding of the multi-wavelength sky.

An important source class, TeV halos, escaped identification until the development of TeV γ-ray instruments, especially those that can detect extended sources. Although TeV halos may have corresponding emission in radio, X-ray, and GeV photons, this was not sufficiently obvious to recognize this source class.

TeV observations also suggest MSPs as an efficient production site of cosmic-ray electrons. This allowed us to show the potential importance of this source class in galactic radio emission, which had not been recognized before. Our work illustrates a close connection between γ-ray astrophysics and galactic astronomy.

TeV and X-ray observations of SS433 and Cen A have produced significant consequences not only for the production of VHE particles in these systems but also for the physics of relativistic outflows produced by compact objects.

In the coming few years, we expect a significant improvement in the observational data. LHAASO, which has just started operation this year, will provide unprecedented capabilities of detecting extended sources like TeV halos, measuring the diffuse Galactic emission, and surveying γ-ray sources up to PeV energies. CTA, which will begin observations in a few years, would have the ability to detect many TeV γ-ray sources with unprecedented sensitivities with great angular and energy resolutions, allowing us to uncover the nature of extreme γ-ray sources in great details. In the further future, IceCube-Gen2 would further offer key information in our understanding of the VHE sky by detecting many extreme neutrinos above TeV energies. This thesis indicates the importance of these new developments in multi-messenger astronomy.

Appendix A

Appendix for Chapter 2

Here we present additional analysis and discussion related to Chapter 2.

A.1 Effect of Uniform Pulsar Period Distributions

One of the most important modeling assumptions in this paper is the spin-period of the pulsar at birth. In the main paper, we utilized several models that utilized a Gaussian distribution to describe the initial pulsar period distribution. We chose three average periods of 50 ms, 120 ms, or 300 ms with this Gaussian, along with variances $\sigma_{P_0} = 50/\sqrt{2}$ ms, $\sigma_{P_0} = 60$ ms and $\sigma_{P_0} = 150$ ms, respectively. However, recent modelling of pulsar population indicates that a uniform period distribution of $0 < P_0 < 500$ ms may be consistent with the pulsar statistics (Gullón et al., 2015).

We produced additional analysis where pulsars have uniform initial spin-period distributions between the breakup limit and $2\langle P_0 \rangle$. We find that, in general, models with a uniform pulsar distribution of P_0 predict a greater number of pulsar than Gaussian models. This is because the uniform distribution produces a larger number of sources with very small P_0. In general, the effect of these models on the number of pulsars as a function of $T_{\rm age}$ is about a factor of ~ 2, compared to models with a Gaussian distribution centered at $\langle P_0 \rangle$.

A.2 Model Uncertainties

Here, we describe all uncertainties in Table 2.2. In Fig. A.2, we show how our results are changed for alternative models for the case of $\langle P_0 \rangle = 120$ ms.

- P_0 **distribution**: In the main text, we adopt a Gaussian distribution following Faucher-Giguère & Kaspi (2006); Watters & Romani (2011). In Fig. A.2 (top left), we compare this with a uniform distribution, motivated by Gullón et al. (2015).
- B_0 **distribution**: In the main text, we adopt a log-normal distribution with mean $\langle \log_{10} B_0 \rangle = 12.65$ and $\sigma_{\log_{10} B_0} = 0.55$ following Faucher-Giguère & Kaspi (2006). In Fig. A.2 (top left), we compare this with another lognormal distribution with $\langle \log_{10} B_0 \rangle = 13.10$ and $\sigma_{\log_{10} B_0} = 0.65$, as defined in Gullón et al. (2014).
- $\dot{E}$ **dependence**: In the main text, we adopt $L_\gamma \propto \dot{E}$. In Fig. A.2 (top right), we compare this with different models which adopt $L_\gamma \propto \dot{E}^{0.8}$ and $L_\gamma \propto \dot{E}^{1.2}$, normalizing the γ-ray flux with the Geminga halo.

- **age dependence**: In the main text, we assume that γ-ray efficiency $L_\gamma/\dot{E}$ is constant for all pulsars. In Fig. A.2 (bottom left), we compare this with different models where $L_\gamma/\dot{E}$ depends on the age of pulsars as $L_\gamma/\dot{E} \propto (T_{\rm age})^{0.5}$ and $L_\gamma/\dot{E} \propto (T_{\rm age})^{-0.5}$, normalizing the γ-ray flux with the Geminga halo and adopting 340 kyr as the age of Geminga. In the case of $L_\gamma/\dot{E} \propto (T_{\rm age})^{0.5}$, we do not assume age dependence for sources older than 340 kyr, in order to avoid producing unrealistically bright late-time sources.
- **source-to-source scatter**: In the main text, we assume that $L_\gamma/\dot{E}$ is constant for all systems. In Fig. A.2 (bottom right), we compare this with different models where $\log_{10}(L_\gamma/\dot{E})$ is a random variable drawn from a normal distribution with mean 1 and standard deviation 0.5.

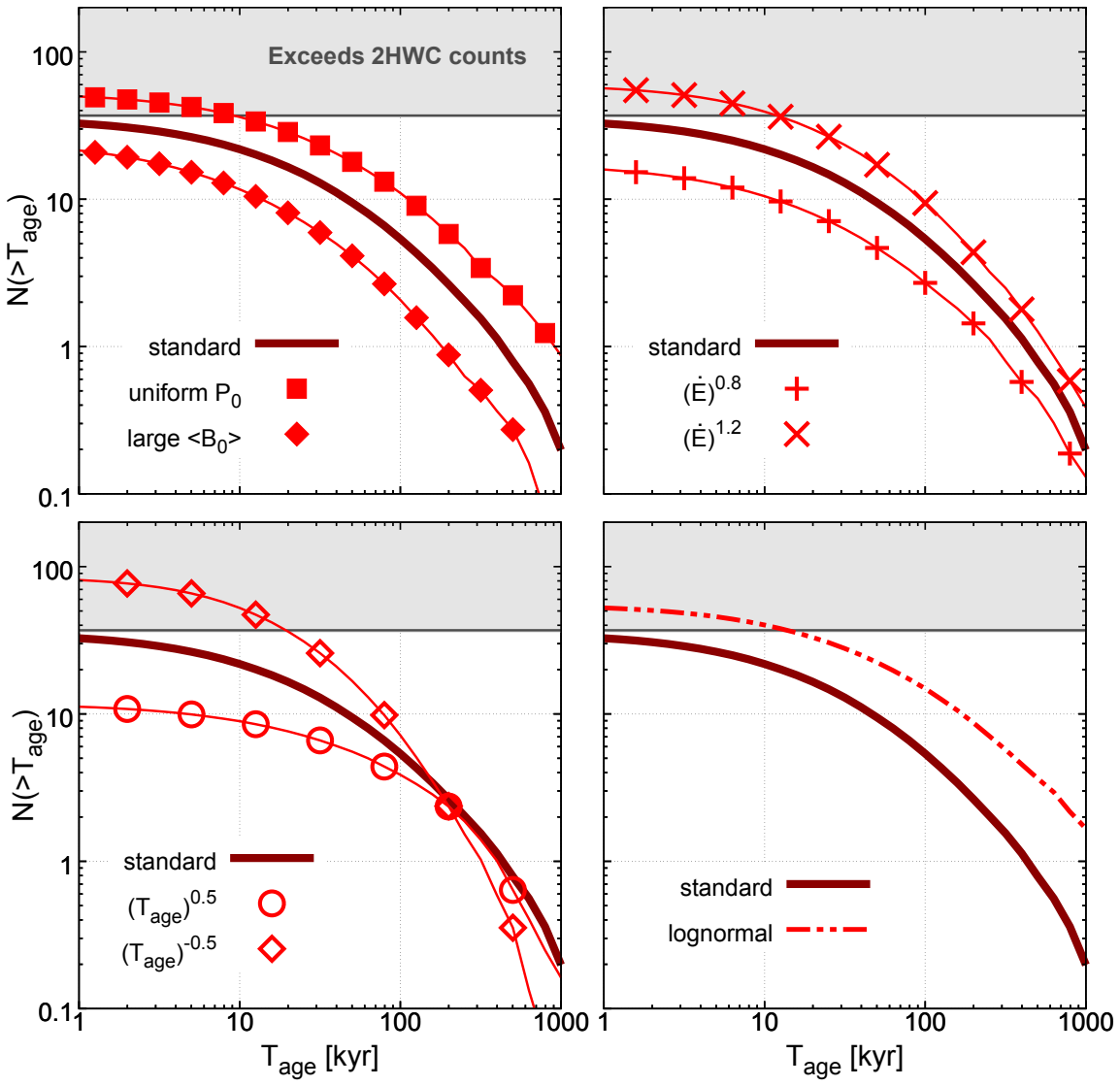

Figure A.1. Same as the upper panel of Fig. 2.4, but for alternative models in the case of $\langle P_0 \rangle = 120$ ms.

Appendix B

Appendix for Chapter 4

Here we present additional analysis and discussion related to Chapter 4.

B.1 Models using Log-Luminosity

In the main text, we fit our model against the luminosity values and uncertainties for each source using a linear fit to the data. This was due to the fact that some sources have negative best-fit values due to instrumental or systematic issues. Here, we re-analyze the data after taking the logarithm of the luminosity values, producing a probability model given by:

$$P_i(L) = \frac{1}{\sqrt{2\pi\sigma^2_{\log_{10} L}}} \exp\left(-\frac{|\log_{10}(L) - \log_{10}(L^{\rm model})|^2}{2\sigma^2_{\log_{10} L}}\right), \tag{B.1}$$

where $\sigma_{\log_{10} L}$ is a free parameter. In this analysis, we use only the 3215 sources that have positive best-fit luminosities. In Table B.1, we calculate $-\ln\mathcal{L}$ for each model, verifying that the SNR+MSP model fits significantly better than other models. These values cannot be directly compared with those in Table 3.1 because the definitions of P_i are different. In particular, while the 1σ error in the uncertainty of each source is identical in both the linear and logarithmic constructions, the likelihood function for any other offset between the modeled and measured source flux will differ.

In Table B.2, we show the best-fit parameters, showing that they are also not significantly changed, and thus the main physical features of our model are robust to this choice.

Table B.1. Values of $-\ln\mathcal{L}$ for different models for the case when we use log-luminosity (Eq. B.1).

	All Sources ($N = 3215$)	Low sSFR ($N = 108$)
Scaling (ψ; Eq. 3.16)	2704	356.7
Scaling (ψ and M; Eq. 3.17)	2193	193.3
Model (SNR only; Eq. 3.18)	2400	384.0
Model (SNR + MSP; Eq. 3.19)	2050	117.4

Figure B.1 shows a scaled version of radio-SFR luminosities, as schematically il- lustrated in the bottom panel of Fig. 3.1. Along with data points for individual galaxies, we separate sources into bins of specific SFRs and show the mean and standard deviation of logarithmic

Table B.2. Best-fit parameters when we use log-luminosity (Eq. B.1).

	α	β	γ	$\sigma_{\log_{10} L}$	
Scaling(ψ)	0.108	0.973	-	0.561	
Scaling(ψ and M)	0.127	0.665	0.530	0.479	
	a_1	a_2	a_3	$\beta_{\rm syn}$	$\sigma_{\log_{10} L}$
Model (SNR only)	0.119	1.06e-9	-	0.351	0.351
Model (SNR+MSP)	0.031	0.046	0.026	0.199	0.458

radio luminosities scaled by masses, $\log_{10}(L/M_*)$, in each bin. It shows a plateau feature, which strongly supports a mass-dependent term in determining the radio luminosity.

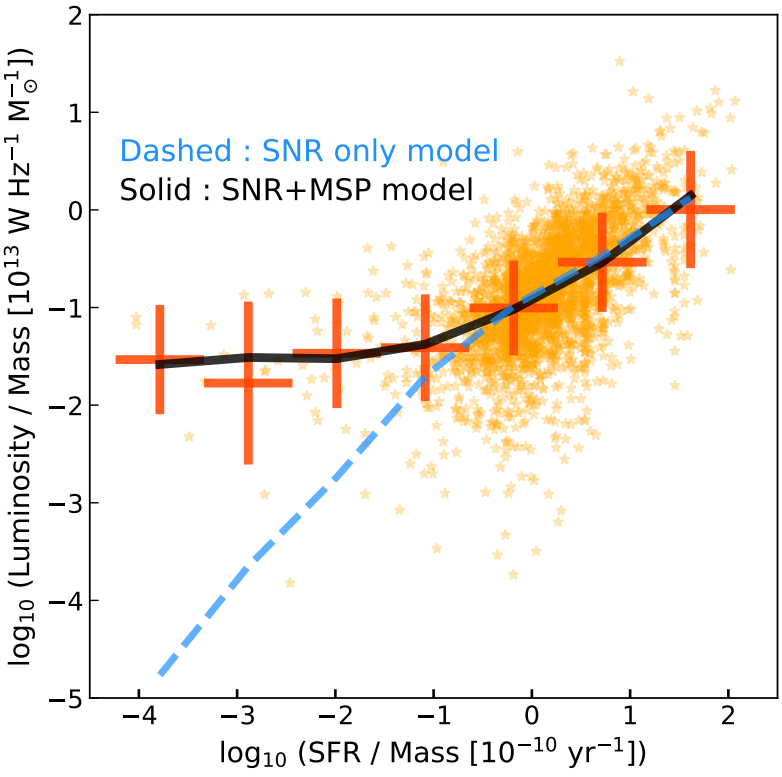

Figure B.1. The radio luminosity - SFR correlation scaled by the stellar masses. Along with data points for individual galaxies (orange), we show the mean and standard deviation with bars. Lines show theoretical predictions, connecting the mean value in each specific-SFR bin that we show with the bars. Theoretically predicted values for individual galaxies are not shown here.

Table B.3. Values of $-\ln\mathcal{L}$ for different models for the case when we include all 3097 sources in our analysis.

	All Sources ($N = 3907$)	Low sSFR ($N = 137$)
Scaling (ψ; Eq. 3.16)	2625.7	566.3
Scaling (ψ and M; Eq. 3.17)	-213.4	17.9
Model (SNR only; Eq. 3.18)	375.2	312.4
Model (SNR + MSP; Eq. 3.19)	-580.6	-32.0

B.2 The Effect of Removing Outliers

In the main text, we removed from our analysis several outliers hat had radio luminosities that significantly exceeded model predictions. This is well justified, because other emission sources (e.g, AGN) or additional effects (e.g., galaxy interactions) may produce radio excesses that do not correlate with recent or historic star formation.

In Table B.3, we show the values of $-\ln\mathcal{L}$ for each model in a scenario where we do not discard these outliers. This confirms that the SNR+MSP models still provide the best fit. However, a comparison of these fits against those in Table 3.1 indicates that our fits are highly affected by several very bright sources. In Fig. B.2, we show the distribution of the log-likelihood value for individual sources. While most of sources have $-\ln\mathcal{L}$ smaller than 10, some individual sources have $-\ln\mathcal{L}$ more than 50 or even 100. These sources dominate the sum of log-likelihood fit, which could potentially affect our results.

Repeating our analysis, we have verified that our conclusions are unchanged if we set the upper limit for outlier removal to log-likliehood values of 100, 25, and 12.5. In all cases, the SNR+MSP model is favored over any other model by $2\Delta\ln\mathcal{L} > 196$. The best-fit parameters remain largely unchanged.

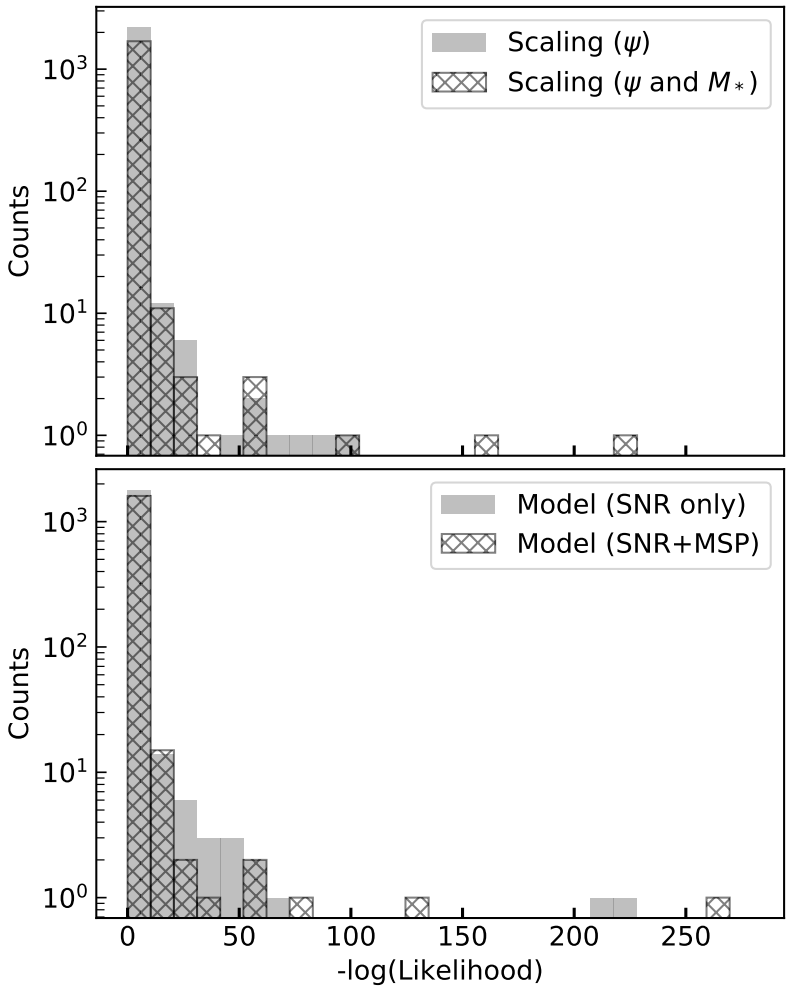

Figure B.2. The distribution of $-\ln\mathcal{L}$ for each SFG. For the scaling model with ψ (top, gray), there is one source that has $-\ln\mathcal{L} = 989$, which is not shown in this histogram.

B.3 The Effect of SFR Modeling

Here, we present an alternative analysis produced by replacing SFRs and masses from G18 with those obtained in S18 (Salim et al., 2018). S18 produces three separate catalogs for three different exposure times for UV imaging. While the shallowest catalog contains the largest dataset (about 90% of SDSS sources are contained), it can be inaccurate for quiescent and passive galaxies. On the other hand, the deepest catalog covers only a small field, and thus includes only ∼7% of SDSS sources. Therefore, we choose to use the catalog of medium exposure time, which can be used for off-main-sequence galaxies and contains about 50% of SDSS sources. We utilize SFRs and masses from this catalog, but continue to utilize the radio luminosities and galaxy classifications determined by G18.

We utilize sources from the S18 catalog that are also contained in the study by G18. Since only 1094 out of 3907 SFGs in G18 are included in the S18 catalog, we have to check if this procedure does not induce any bias. Figure B.3 shows the histogram of sources binned using

the SFRs determined by G18. This shows that the cross-correlated catalog is not significantly biased toward high SFR sources. However, we should keep in mind that more than half of low-SFR sources ($< 10^{-2}$ $M_{\odot}yr^{-1}$) are not included in the S18 catalog.

Figure B.4 compares the masses (top) and SFRs (bottom) determined by each catalog. We find that mass estimations are generally in good agreement, although there are orders of magnitude discrepancies for a small fraction of sources. For SFRs, we find that sources with small ($< 10^{-2}$ $M_{\odot}yr^{-1}$) SFRs in G18 systematically have much higher SFRs in the model of S18. This is worrisome, because this suggests that the radio excess in low-SFR sources may be attributed to SFR measurement errors.

Figure 3.4 (in the main text) compares the radio-SFR correlation for different SFR estimations. There are two notable changes. First, the main body of radio-SFR correlation (SFR$> 10^{-1}$ $M_{\odot}yr^{-1}$) remain largely unchanged, but the scatter gets significantly larger. Due to this, our method of fitting the correlation with a linear-luminosity model is biased toward bright sources. Therefore, we fit the data using log-luminosity with the method detailed in Appendix B.1 to derive the slope of radio-SFR correlation. Restricting our analysis to a region with sSFR$>10^{-11}$ yr^{-1}, where the radio-SFR correlation should hold, we find a flatter slope for S18 SFRs, $L \propto \psi^{0.6}$, which is in significant tension with previous estimates of the radio-SFR correlation at low-frequencies Cox et al. (1988).

Second, there are few low-SFR sources when we utilize SFRs from S18. This makes the excess feature in low-SFR sources is much less pronounced. As a result, our mass dependent model is not statistically preferred compared to the SFR-only scaling, contrary to what we observed for G18 SFRs.

However, we note that more than half of the low-SFR sources ($< 10^{-2}$ $M_{\odot}yr^{-1}$) observd

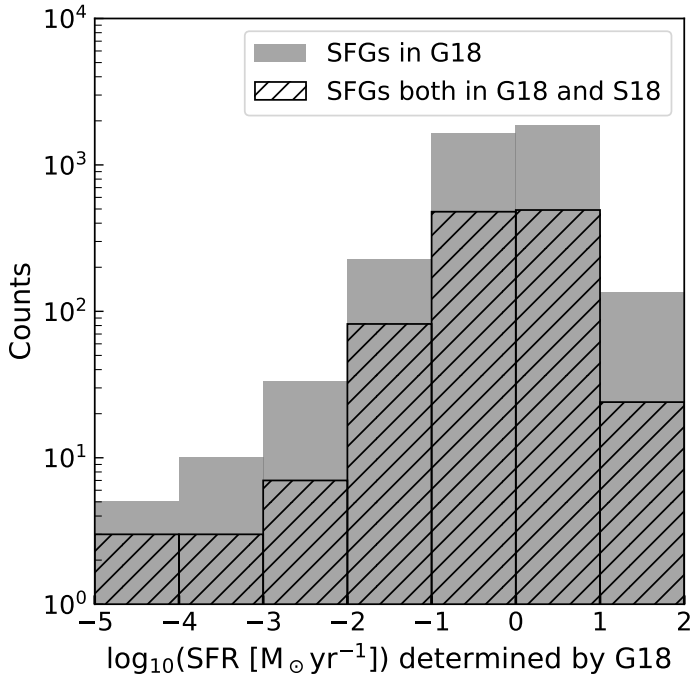

Figure B.3. Histogram of SFGs that are included in G18 (gray) and both in G18 and S18 (black, hatched).

by G18 are not contained in S18. Therefore, to determine whether the excess feature can be robust against SFR estimates, we need deeper observations and a better determination of SFRs for the low-SFR sources that are not included in the medium- or deep- catalog by S18.

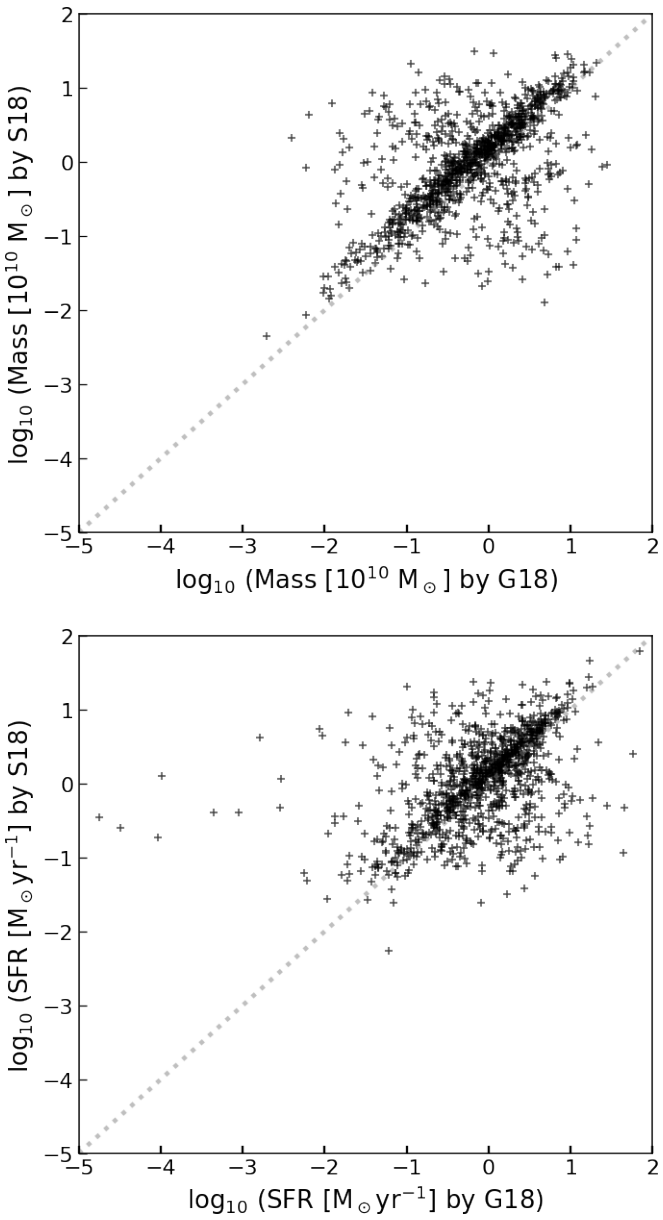

Figure B.4. Comparison of stellar masses (top) and SFRs (bottom) determined by Gürkan et al. (2018) (G18, x-axis) and Salim et al. (2018) (S18, y-axis). Dashed line correspond to the case where these two estimates are identical.

B.4 The Inclusion of Unclassified Sources

In the main text, we used 3907 sources that are classified by G18 as SFGs using a BPT-diagram. There are 6370 sources that are not classified due to the absence or weak detection ($< 3\sigma$) of emission lines. Although these "unclassified" sources are not used in the main text, they necessarily include many high-mass and low-SFR sources, which are important for testing our model.

Here, we check whether our model is consistent with LOFAR observations when we include unclassified sources. This analysis should be taken with caution, because there can be sources that are affected by AGN. To avoid biasing our results with the brightest sources that might be strongly affected by AGN, we fit the data using log-luminosity following the method in Appendix B.1.

We find that, if we use the SFRs and masses determined by G18, our SNR+MSP model is preferred over the SNR-only model by $\Delta\mathrm{LG}(\mathcal{L}) = 3480$. If we replace the SFR and mass determinations by those in S18, the SNR+MSP model is still preferred by $\Delta\mathrm{LG}(\mathcal{L}) = 746$. In this cases, and restricting ourselves to sources with sSFR$>10^{-11}$ yr^{-1} we find a slightly harder value for the radio-SFR correlation, fitting $L \propto \psi^{0.8}$, which is somewhat more consistent with the value obtained in the main text.

Figure B.5 shows the scaled luminosities vs specific SFRs for two different galactic parameters derived by G18 (left) and S18 (right). In both datasets, we can see a pleateau feature for low specific SFR sources, which is consistent with original findings by G18. This figure clearly illustrates that MSP-based model is significantly favored.

As noted in the main text, this agreement does not prove that MSPs produce the mass-dependent radio emission. In particular, for unclassified sources, we need more careful examination of the contributions from AGN activities. However, it is encouraging that we do see a feature that is expected for MSPs, and the derived parameters are consistent with this interpretation.

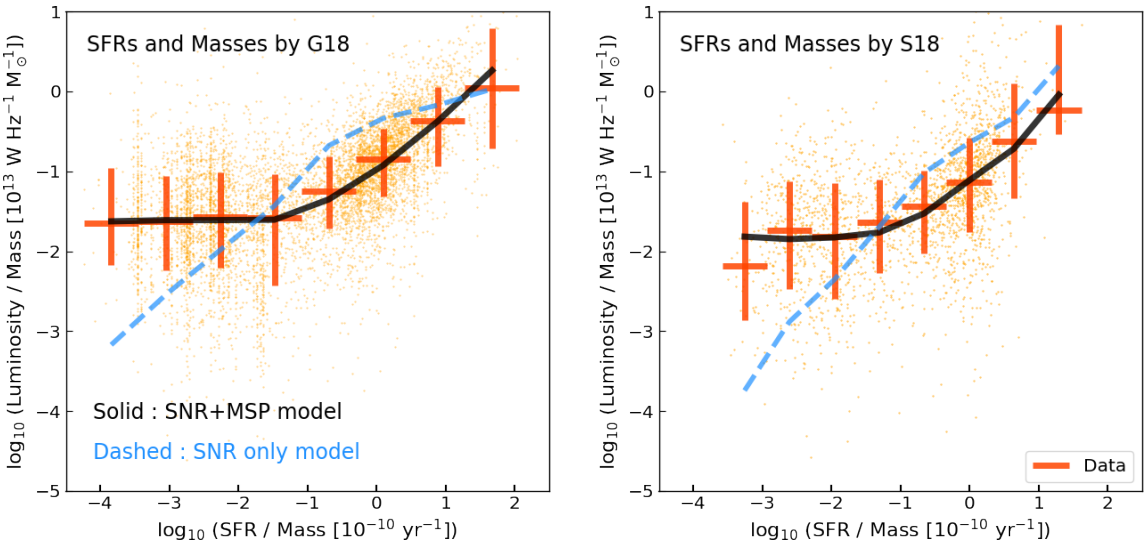

Figure B.5. The radio luminosity - SFR correlation scaled by the stellar masses for SFGs and unclassified sources, with galactic parameters determined by G18 (left) and S18 (right). Along with data points for individual galaxies (orange), we show the median and the 16th - 84th percentile range (bars). Lines show theoretical predictions, connecting the median value in each specific-SFR bin that we show with the bars. Theoretically predicted values for individual galaxies are not shown.

Appendix C

Appendix for Chapter 6

Here we present additional analysis and discussion related to Chapter 6.

C.1 Relativistic Beaming

Since the jet bulk velocity is only mildly-relativistic, we do not consider relativistic effects in the main text. Here we discuss their possible impact.

Relativistic effects depend on the jet bulk velocity, β, and the viewing angle, $\theta_{\rm obs}$, through the Lorentz and Doppler factors, $\Gamma = 1/\sqrt{1-\beta^2}$ and $\mathcal{D} = 1/(\Gamma(1-\beta\cos\theta_{\rm obs}))$. The viewing angle is observationally uncertain, probably being in the range of $\theta_{\rm obs} \simeq 20^\circ - 50^\circ$ (Tingay et al., 1998; Hardcastle et al., 2003). This also induces some uncertainties in the jet velocity, because it is obtained from the viewing angle and the apparent velocity $\beta_{\rm app}$ as

$$\beta = \frac{\beta_{\rm app}}{\beta_{\rm app}\cos\theta_{\rm obs} + \sin\theta_{\rm obs}} \,. \tag{C.1}$$

If we fix the jet apparent velocity to $\beta_{\rm app} \simeq 0.5c$ (Hardcastle et al., 2003) and use $20^\circ < \theta_{\rm obs} < 50^\circ$, then the Lorentz factor Γ is at most 1.3, and $\mathcal{D}$ is smaller than 2. While these suggest that relativistic effects are not critical, they may deserve a more careful check because they could strongly depend on Γ and $\mathcal{D}$.

To correctly account for relativistic effects, we have three points to be modified. First, the jet energy density in the jet comoving frame should be $P_{\rm jet}/(\pi R^2\Gamma^2\beta c)$, i.e., the definition in Eq. (5.3) needs to be modified by a factor of Γ^{-2}. Other energy parameters w_i and η_i are defined in the jet comoving frame in the main text. Second, the X-ray luminosity density $j^{\rm D}_{\rm keV}$ is calculated in the observer frame, since it is estimated from the observed X-ray flux and volume. To transform $j^{\rm D}_{\rm keV}$ to the comoving frame, we use a well-known fact that j_ν/ν^2 is a Lorentz invariant, where we adopt the standard notation of $j_\nu = dE/(dV dt d\Omega d\nu)$ (e.g., Rybicki & Lightman, 1979). Therefore, j_ν transforms as $\mathcal{D}^2$. Since we consider an isotropic emitter, $j_{\rm keV}$ is related to j_ν as $j_\nu d\nu = j_{\rm keV}/4\pi$. This indicates that the X-ray luminosity density in the jet comoving frame is $\mathcal{D}^{-3} j^{\rm D}_{\rm keV}$. Third, since the synchrotron cooling time ($t_{\rm syn}$) is proportional to $\nu^{-1/2}B^{-3/2}$, in the comoving frame it is longer by a factor of $D^{1/2}\Gamma^{3/2}$. Combining these three points, the energy density of electrons ($w^{\rm D}_{e,{\rm keV}}$) should be proportional to $\mathcal{D}^{-5/2}\Gamma^{3/2}$, and, the parameter $\eta^{\rm D}_{e,{\rm NT}}$ should change as

$$\eta^{\rm D}_{e,{\rm NT}} \propto \mathcal{D}^{-5/2}\Gamma^{7/2} \tag{C.2}$$

If we fix $\beta_{\rm app} \simeq 0.5c$ (Hardcastle et al., 2003), the RHS in Eq. (C.2) falls in the range between 0.48 ($\theta_{\rm obs} = 20°$) and 0.85 ($\theta_{\rm obs} = 50°$).

We should also note that we do not consider the transformation of $w_{\rm ph}$ to the jet comoving frame. This would require information about the angular distribution of the target photon field. For example, if the photon field is isotropic in the laboratory frame then its energy density transforms to the jet co-moving frame as $\mathcal{T} = \Gamma^2 \left(1 + {}^{\beta^2}/_{3}\right)$, which falls between 1.4 ($\theta_{\rm obs} = 50°$) and 2 ($\theta_{\rm obs} = 20°$). If we instead consider the target photons are from a point source at the jet base, then the correction would be $\mathcal{T} = \Gamma^{-2}(1+\beta)^{-2}$, which is in the range of 2.7 ($\theta_{\rm obs} = 50°$) and 4.2 ($\theta_{\rm obs} = 20°$). If we take the transformation of $w_{\rm ph}$ into account, the magnetization parameter $\eta_{\rm B}^{\rm D}$ would decrease by $\mathcal{T}$, which strengthen our conclusion that the jet is weakly magnetized. While $\eta_{\rm e,NT}^{\rm D}$ can be increased by $\mathcal{T}^{3/4}$, combined with the correction due to Eq. (C.2), the total increase in $\eta_{\rm e,NT}^{\rm D}$ would be less than a factor of 1.8 for cases considered here.

Bibliography

Aartsen, M. G., et al. 2014, Physical Review Letters, 113, 101101
—. 2017, The Astrophysical Journal, 849, 67
—. 2020, The Astrophysical Journal, 898, 117
Abazajian, K. N. 2011, JCAP, 03, 010
Abdalla, H., et al. 2018a, Astron. and Astrophys., 612, A1
—. 2018b, Astron. and Astrophys., 612, A2
—. 2019, Astron. and Astrophys., 621, A116
Abdalla, H., et al. 2020, Nature, 582, 356
Abdo, A. A., et al. 2008, The Astrophysical Journal, 688, 1078
—. 2009a, Science, 325, 845
—. 2009b, Astrophys. J. Lett., 700, L127
—. 2010, The Astrophysical Journal, 713, 146
—. 2013, The Astrophysical Journal, Supplement, 208, 17
Abdollahi, S., et al. 2020, The Astrophysical Journal, Supplement, 247, 33
Abell, G. O., & Margon, B. 1979, Nature, 279, 701
Abeysekara, A. U., et al. 2013, Astroparticle Physics, 50, 26
—. 2017a, Science, 358, 911
—. 2017b, The Astrophysical Journal, 843, 39
—. 2017c, The Astrophysical Journal, 843, 40
—. 2018, Nature, 562, 82
Abeysekara, A. U., Albert, A., Alfaro, R., et al. 2020, Physical Review Letters, 124, 021102
Abramowski, A., et al. 2012, Astron. and Astrophys., 548, A38
Acharya, B. S., et al. 2017, ArXiv e-prints, arXiv:1709.07997
Ackermann, M., et al. 2012, The Astrophysical Journal, 750, 3
Ackermann, M., et al. 2012, Astrophys. J., 755, 164
Ackermann, M., et al. 2016, The Astrophysical Journal, Letters, 824, L20
—. 2017, The Astrophysical Journal, 836, 208
Adriani, O., et al. 2010, Physical Review Letters, 105, 121101
Aguilar, M., et al. 2013, Phys. Rev. Lett., 110, 141102
Aharonian, F. 2013, Astrophysics at Very High Energies, Saas-Fee Advanced Course, Volume 40. ISBN 978-3-642-36133-3. Springer-Verlag Berlin Heidelberg, 2013, p. 1, 40, 1
Aharonian, F., et al. 2006, Astron. and Astrophys., 457, 899
Aharonian, F. A. 1995, Nuclear Physics B Proceedings Supplements, 39, 193
—. 2004, Very high energy cosmic gamma radiation : A crucial window on the extreme Universe (World Scientific Publishing Co), doi:10.1142/4657
Aharonian, F. A., Atoyan, A. M., & Kifune, T. 1997, Mon. Not. R. Astron. Soc., 291, 162

Aharonian, F. A., Kelner, S. R., & Prosekin, A. Y. 2010, Physical Review D, 82, 043002
Ahlers, M., & Murase, K. 2014, Physical Review D, 90, 023010
Ahnen, M. L., et al. 2018, Astronomy & Astrophysics, 612, A14
Ajello, M., Di Mauro, M., Paliya, V. S., & Garrappa, S. 2020, The Astrophysical Journal, 894, 88
Ajello, M., et al. 2016, Astrophys. J., 819, 44
Albert, A., et al. 2020, arXiv e-prints, arXiv:2007.08582
Albert, J., et al. 2008, The Astrophysical Journal, 674, 1037
Amano, T., & Hoshino, M. 2012, Astrophysics and Space Science Proceedings, 33, 143
Appleton, P. N., et al. 2004, The Astrophysical Journal, Supplement, 154, 147
Aramaki, T., Adrian, P. O. H., Karagiorgi, G., & Odaka, H. 2020, Astroparticle Physics, 114, 107
Araudo, A. T., Bell, A. R., & Blundell, K. M. 2015, The Astrophysical Journal, 806, 243
Atkins, R., et al. 2005, Physical Review Letters, 95, 251103
Atoyan, A. M., & Aharonian, F. A. 1999, Monthly Notices of the Royal Astronomical Society, 302, 253
Atoyan, A. M., Aharonian, F. A., & Völk, H. J. 1995, Physical Review D, 52, 3265
Atwood, W. B., et al. 2009, The Astrophysical Journal, 697, 1071
Baade, W., & Zwicky, F. 1934, Proceedings of the National Academy of Science, 20, 259
Badenes, C., Maoz, D., & Draine, B. T. 2010, Mon. Not. R. Astron. Soc., 407, 1301
Bai, X., et al. 2019, arXiv e-prints, arXiv:1905.02773
Bamba, A., Anada, T., Dotani, T., et al. 2010, Astrophys. J. Lett., 719, L116
Barkov, M. V., Aharonian, F. A., & Bosch-Ramon, V. 2010, The Astrophysical Journal, 724, 1517
Barkov, M. V., Bosch-Ramon, V., & Aharonian, F. A. 2012, The Astrophysical Journal, 755, 170
Bartels, R., Krishnamurthy, S., & Weniger, C. 2016, Phys. Rev. Lett., 116, 051102
Bartels, R., Storm, E., Weniger, C., & Calore, F. 2018a, Nature Astronomy, 2, 819
Bartels, R. T., Edwards, T. D. P., & Weniger, C. 2018b, Monthly Notices of the Royal Astronomical Society, 481, 3966
Bartoli, B., et al. 2015, The Astrophysical Journal, 806, 20
Basu, A., Beck, R., Schmidt, P., & Roy, S. 2015, Monthly Notices of the Royal Astronomical Society, 449, 3879
Bates, S. D., Lorimer, D. R., Rane, A., & Swiggum, J. 2014, Mon. Not. R. Astron. Soc., 439, 2893
Beck, R., Chamandy, L., Elson, E., & Blackman, E. G. 2019, Galaxies, 8, 4
Beck, R., & Golla, G. 1988, Astronomy & Astrophysics, 191, L9
Beckmann, V., Jean, P., Lubiński, P., Soldi, S., & Terrier, R. 2011, Astronomy & Astrophysics, 531, A70
Bednarek, W. 2019, Monthly Notices of the Royal Astronomical Society, 483, 1003
Bednarek, W., & Banasiński, P. 2015, The Astrophysical Journal, 807, 168
Bednarek, W., & Sitarek, J. 2007, Monthly Notices of the Royal Astronomical Society, 377, 920
Bednarek, W., Sitarek, J., & Sobczak, T. 2016, Monthly Notices of the Royal Astronomical

Society, 458, 1083
Begelman, M. C., King, A. R., & Pringle, J. E. 2006, Monthly Notices of the Royal Astronomical Society, 370, 399
Bell, A. R. 2013, Astroparticle Physics, 43, 56
Bell, A. R., Araudo, A. T., Matthews, J. H., & Blundell, K. M. 2018, Monthly Notices of the Royal Astronomical Society, 473, 2364
Bell, E. F. 2003, Astrophys. J., 586, 794
Berezinskii, V. S., Bulanov, S. V., Dogiel, V. A., & Ptuskin, V. S. 1990, Astrophysics of cosmic rays
Best, P. N., & Heckman, T. M. 2012, Monthly Notices of the Royal Astronomical Society, 421, 1569
Blandford, R. D., & Koenigl, A. 1979, aplett, 20, 15
Blandford, R. D., & Payne, D. G. 1982, Monthly Notices of the Royal Astronomical Society, 199, 883
Blandford, R. D., & Znajek, R. L. 1977, Monthly Notices of the Royal Astronomical Society, 179, 433
Blondin, J. M., Chevalier, R. A., & Frierson, D. M. 2001, The Astrophysical Journal, 563, 806
Blumenthal, G. R., & Gould, R. J. 1970, Reviews of Modern Physics, 42, 237
Blundell, K. M., & Bowler, M. G. 2004, The Astrophysical Journal, 616, L159
Bordas, P., Bosch-Ramon, V., Paredes, J. M., & Perucho, M. 2009, Astronomy & Astrophysics, 497, 325
Bordas, P., Sun, X., Yang, R., Kafexhiu, E., & Aharonian, F. A. 2017, in American Institute of Physics Conference Series, Vol. 1792, 6th International Symposium on High Energy Gamma-Ray Astronomy, 040020
Bordas, P., Yang, R., Kafexhiu, E., & Aharonian, F. 2015, The Astrophysical Journal, 807, L8
Boroson, B., Kim, D.-W., & Fabbiano, G. 2011, The Astrophysical Journal, 729, 12
Bosch-Ramon, V., Romero, G. E., & Paredes, J. M. 2006, Astronomy & Astrophysics, 447, 263
Bowler, M. G., & Keppens, R. 2018, Astronomy & Astrophysics, 617, A29
Brinkmann, W., Aschenbach, B., & Kawai, N. 1996, Astronomy & Astrophysics, 312, 306
Brinkmann, W., & Kawai, N. 2000, Astronomy & Astrophysics, 363, 640
Brinkmann, W., Kotani, T., & Kawai, N. 2005, Astronomy & Astrophysics, 431, 575
Brinkmann, W., Pratt, G. W., Rohr, S., Kawai, N., & Burwitz, V. 2007, Astronomy & Astrophysics, 463, 611
Brisbois, C., Riviere, C., Fleischhack, H., & Smith, A. 2018, The Astronomer's Telegram, 12013
Broderick, J. W., et al. 2018, Monthly Notices of the Royal Astronomical Society, 475, 5360
Brown, M. J. I., et al. 2017, The Astrophysical Journal, 847, 136
Bucciantini, N. 2011, Astrophysics and Space Science Proceedings, 21, 473
—. 2018, Mon. Not. R. Astron. Soc., 480, 5419
Bykov, A. M., Amato, E., Petrov, A. E., Krassilchtchikov, A. M., & Levenfish, K. P. 2017, Space Science Rev., 207, 235

Bykov, A. M., Pavlov, G. G., Artemyev, A. V., & Uvarov, Y. A. 2012, Monthly Notices of the Royal Astronomical Society, 421, L67

Bykov, A. M., Petrov, A. E., Krassilchtchikov, A. M., et al. 2019, The Astrophysical Journal, Letters, 876, L8

Calistro Rivera, G., et al. 2017, Monthly Notices of the Royal Astronomical Society, 469, 3468

Calzetti, D., et al. 2010, The Astrophysical Journal, 714, 1256

Cappellari, M., Neumayer, N., Reunanen, J., et al. 2009, Monthly Notices of the Royal Astronomical Society, 394, 660

Carlson, E., Linden, T., & Profumo, S. 2016, Phys. Rev. D, 94, 063504

Celotti, A., & Ghisellini, G. 2008, Monthly Notices of the Royal Astronomical Society, 385, 283

Chen, K., & Ruderman, M. 1993, The Astrophysical Journal, 402, 264

Cheng, K. S., Chernyshov, D. O., Dogiel, V. A., Hui, C. Y., & Kong, A. K. H. 2010, The Astrophysical Journal, 723, 1219

Cherepashchuk, A. M., Postnov, K. A., & Belinski, A. A. 2019, Monthly Notices of the Royal Astronomical Society, 485, 2638

Cherepashchuk, A. M., Sunyaev, R. A., Molkov, S. V., et al. 2013, Monthly Notices of the Royal Astronomical Society, 436, 2004

Chiaberge, M., Capetti, A., & Celotti, A. 2001, Monthly Notices of the Royal Astronomical Society, 324, L33

Chyży, K. T., et al. 2018, Astronomy & Astrophysics, 619, A36

Cieślar, M., Bulik, T., & Osłowski, S. 2018, ArXiv e-prints, arXiv:1803.02397

Clemens, M. S., Scaife, A., Vega, O., & Bressan, A. 2010, Monthly Notices of the Royal Astronomical Society, 405, 887

Condon, J. J. 1992, Annual Review of Astronomy & Astrophysics, 30, 575

Condon, J. J., Cotton, W. D., & Broderick, J. J. 2002, The Astronomical Journal, 124, 675

Corbet, R. H. D. 1984, Astronomy & Astrophysics, 141, 91

Coroniti, F. V. 1990, The Astrophysical Journal, 349, 538

Cowsik, R., & Madziwa-Nussinov, T. 2016, The Astrophysical Journal, 827, 119

Cox, M. J., Eales, S. A. E., Alexander, P., & Fitt, A. J. 1988, Monthly Notices of the Royal Astronomical Society, 235, 1227

da Cunha, E., Charlot, S., & Elbaz, D. 2008, Monthly Notices of the Royal Astronomical Society, 388, 1595

D'Angelo, M., Morlino, G., Amato, E., & Blasi, P. 2018, Mon. Not. Roy. Astron. Soc., 474, 1944

Davies, L. J. M., et al. 2017, Monthly Notices of the Royal Astronomical Society, 466, 2312

Daylan, T., Finkbeiner, D. P., Hooper, D., et al. 2016, Phys. Dark Univ., 12, 1

De Angelis, A., et al. 2017, Experimental Astronomy, 44, 25

de Jager, O. C. 2008, Astrophys. J. Lett., 678, L113

de Jager, O. C., Slane, P. O., & LaMassa, S. 2008, Astrophys. J. Lett., 689, L125

de Jager, O. C., Ferreira, S. E. S., Djannati-Ataï, A., et al. 2009, ArXiv e-prints, arXiv:0906.2644

de Jong, T., Klein, U., Wielebinski, R., & Wunderlich, E. 1985, Astronomy & Astrophysics,

147, L6

Dermer, C. D., & Menon, G. 2009, High Energy Radiation from Black Holes: Gamma Rays, Cosmic Rays, and Neutrinos

Di Mauro, M., Manconi, S., & Donato, F. 2019, Physical Review D, 100, 123015

—. 2020, Physical Review D, 101, 103035

Di Sciascio, G., & LHAASO Collaboration. 2016, Nuclear and Particle Physics Proceedings, 279, 166

Dickey, J. M., & Salpeter, E. E. 1984, The Astrophysical Journal, 284, 461

Downes, A. J. B., Pauls, T., & Salter, C. J. 1986, Monthly Notices of the Royal Astronomical Society, 218, 393

Dubner, G. M., Holdaway, M., Goss, W. M., & Mirabel, I. F. 1998, The Astronomical Journal, 116, 1842

Eckner, C., et al. 2018, The Astrophysical Journal, 862, 79

Eikenberry, S. S., Cameron, P. B., Fierce, B. W., et al. 2001, The Astrophysical Journal, 561, 1027

Evoli, C., Linden, T., & Morlino, G. 2018, Physical Review D, 98, 063017

Evoli, C., Linden, T., & Morlino, G. 2018, Phys. Rev. D, 98, 063017

Evoli, C., Morlino, G., Blasi, P., & Aloisio, R. 2020, Physical Review D, 101, 023013

Fabian, A. C., & Rees, M. J. 1979, Monthly Notices of the Royal Astronomical Society, 187, 13P

Fabrika, S. 2004, Astrophysics and Space Physics Reviews, 12, 1

Fang, K., Bi, X.-J., & Yin, P.-F. 2019, Monthly Notices of the Royal Astronomical Society, 488, 4074

Fang, K., Charles, E., & Blandford, R. D. 2020, The Astrophysical Journal, Letters, 889, L5

Faucher-Giguère, C.-A., & Kaspi, V. M. 2006, The Astrophysical Journal, 643, 332

Filho, M. E., Tabatabaei, F. S., Sánchez Almeida, J., Muñoz-Tuñón, C., & Elmegreen, B. G. 2019, Monthly Notices of the Royal Astronomical Society, 484, 543

Fragos, T., et al. 2013, The Astrophysical Journal, 764, 41

Fujita, Y., Ohira, Y., & Takahara, F. 2010, The Astrophysical Journal, Letters, 712, L153

Fujita, Y., Takahara, F., Ohira, Y., & Iwasaki, K. 2011, Monthly Notices of the Royal Astronomical Society, 415, 3434

Funk, S. 2015, Annual Review of Nuclear and Particle Science, 65, 245

Gaensler, B. M., & Slane, P. O. 2006, Annual Review of Astronomy & Astrophysics, 44, 17

Geldzahler, B. J., Pauls, T., & Salter, C. J. 1980, Astronomy & Astrophysics, 84, 237

Gelfand, J. D., Slane, P. O., & Zhang, W. 2009, The Astrophysical Journal, 703, 2051

Ghisellini, G., Tavecchio, F., Foschini, L., et al. 2010, Monthly Notices of the Royal Astronomical Society, 402, 497

Giacinti, G., Mitchell, A. M. W., López-Coto, R., et al. 2020, Astronomy & Astrophysics, 636, A113

Gilfanov, M. 2004, Monthly Notices of the Royal Astronomical Society, 349, 146

Gilfanov, M. 2004, Mon. Not. Roy. Astron. Soc., 349, 146

Gonthier, P. L., Harding, A. K., Ferrara, E. C., et al. 2018, The Astrophysical Journal, 863, 199

Gonthier, P. L., Van Guilder, R., & Harding, A. K. 2004, The Astrophysical Journal, 604,

775

Goodall, P. T., Alouani-Bibi, F., & Blundell, K. M. 2011a, Monthly Notices of the Royal Astronomical Society, 414, 2838

Goodall, P. T., Blundell, K. M., & Bell Burnell, S. J. 2011b, Monthly Notices of the Royal Astronomical Society, 414, 2828

Goodenough, L., & Hooper, D. 2009, arXiv:0910.2998

Goodger, J. L., et al. 2010, The Astrophysical Journal, 708, 675

Green, D. A. 2004, Bulletin of the Astronomical Society of India, 32, 335

Grenier, I. A., Black, J. H., & Strong, A. W. 2015, Annual Review of Astronomy & Astrophysics, 53, 199

Griffin, R. D., Dai, X., & Thompson, T. A. 2016, The Astrophysical Journal, Letters, 823, L17

Grindlay, J. E. 1984, Advances in Space Research, 3, 19

Grondin, M.-H., Romani, R. W., Lemoine-Goumard, M., et al. 2013, The Astrophysical Journal, 774, 110

Gullón, M., Miralles, J. A., Viganò, D., & Pons, J. A. 2014, Mon. Not. R. Astron. Soc., 443, 1891

Gullón, M., Pons, J. A., Miralles, J. A., et al. 2015, Monthly Notices of the Royal Astronomical Society, 454, 615

Gupta, S., Böttcher, M., & Dermer, C. D. 2006, The Astrophysical Journal, 644, 409

Gürkan, G., et al. 2018, Monthly Notices of the Royal Astronomical Society, 475, 3010

H. E. S. S. Collaboration, et al. 2018, Astronomy & Astrophysics, 619, A71

Haberl, F. 2005, in 5 years of Science with XMM-Newton, ed. U. G. Briel, S. Sembay, & A. Read, 39–44

Hardcastle, M. J., & Croston, J. H. 2011, Monthly Notices of the Royal Astronomical Society, 415, 133

Hardcastle, M. J., Kraft, R. P., & Worrall, D. M. 2006, Monthly Notices of the Royal Astronomical Society, 368, L15

Hardcastle, M. J., Worrall, D. M., Kraft, R. P., et al. 2003, The Astrophysical Journal, 593, 169

Harding, A. K., & Muslimov, A. G. 2011, The Astrophysical Journal, 743, 181

Harris, G. L. H., Rejkuba, M., & Harris, W. E. 2010, pasa, 27, 457

Harwit, M., & Pacini, F. 1975, The Astrophysical Journal, Letters, 200, L127

Heesen, V., Brinks, E., Leroy, A. K., et al. 2014, The Astronomical Journal, 147, 103

Heesen, V., et al. 2019, Astronomy & Astrophysics, 622, A8

Heinz, S., & Sunyaev, R. 2002, Astronomy & Astrophysics, 390, 751

Helou, G., Soifer, B. T., & Rowan-Robinson, M. 1985, The Astrophysical Journal, Letters, 298, L7

Hillas, A. M. 1984, Annual Review of Astronomy & Astrophysics, 22, 425

Hillwig, T. C., & Gies, D. R. 2008, The Astrophysical Journal, Letters, 676, L37

Hillwig, T. C., Gies, D. R., Huang, W., et al. 2004, The Astrophysical Journal, 615, 422

Hindson, L., Kitchener, G., Brinks, E., et al. 2018, The Astrophysical Journal, Supplement, 234, 29

Hinton, J. A., Funk, S., Parsons, R. D., & Ohm, S. 2011, Astrophys. J. Lett., 743, L7

Hinton, J. A., & Hofmann, W. 2009, Ann. Rev. of Astron. and Astrophys., 47, 523

Hodge, J. A., Becker, R. H., White, R. L., & de Vries, W. H. 2008, The Astronomical Journal, 136, 1097

Hooper, D., Cholis, I., & Linden, T. 2018, Physics of the Dark Universe, 21, 40

Hooper, D., Cholis, I., Linden, T., & Fang, K. 2017, Physical Review D, 96, 103013

Hooper, D., & Linden, T. 2016, Journal of Cosmology and Astroparticle Physics, 2016, 018

—. 2018a, Physical Review D, 98, 083009

—. 2018b, Physical Review D, 98, 043005

—. 2018c, Physical Review D, 98, 043005

Horiuchi, S., Meier, D. L., Preston, R. A., & Tingay, S. J. 2006, Publications of the Astronomical Society of Japan, 58, 211

Hui, C. Y., & Becker, W. 2006, Astronomy & Astrophysics, 448, L13

Hummel, E. 1991, Astronomy & Astrophysics, 251, 442

Hummel, E., Davies, R. D., Wolstencroft, R. D., van der Hulst, J. M., & Pedlar, A. 1988, Astronomy & Astrophysics, 199, 91

IceCube Collaboration. 2013, Science, 342, 1242856

Igoshev, A. P., & Popov, S. B. 2013, Mon. Not. R. Astron. Soc., 432, 967

Inoue, Y., & Tanaka, Y. T. 2016, The Astrophysical Journal, 828, 13

Ishizaki, W., Asano, K., & Kawaguchi, K. 2018, The Astrophysical Journal, 867, 141

Israel, F. P., & Mahoney, M. J. 1990, The Astrophysical Journal, 352, 30

Israel, F. P., Wall, W. F., Raban, D., et al. 2010, Astron. and Astrophys., 519, A67

James, F., & Roos, M. 1975, Computer Physics Communications, 10, 343

Jarvis, M. J., et al. 2010, Monthly Notices of the Royal Astronomical Society, 409, 92

Johnson, T. J., et al. 2014, The Astrophysical Journal, Supplement, 213, 6

Joshi, V., Jardin-Blicq, A., & HAWC Collaboration. 2017, International Cosmic Ray Conference, 35, 806

Kaplan, D. L., & van Kerkwijk, M. H. 2009, The Astrophysical Journal, 705, 798

Kar, P. 2017, International Cosmic Ray Conference, 35, 713

Kargaltsev, O., & Pavlov, G. G. 2008, in American Institute of Physics Conference Series, Vol. 983, 40 Years of Pulsars: Millisecond Pulsars, Magnetars and More, ed. C. Bassa, Z. Wang, A. Cumming, & V. M. Kaspi, 171–185

Kargaltsev, O., & Pavlov, G. G. 2010, X-ray Astronomy 2009; Present Status, Multi-Wavelength Approach and Future Perspectives, 1248, 25

Kargaltsev, O., Rangelov, B., & Pavlov, G. G. 2013, arXiv e-prints, arXiv:1305.2552

Kataoka, J., Stawarz, Ł., Aharonian, F., et al. 2006, The Astrophysical Journal, 641, 158

Kelner, S. R., Aharonian, F. A., & Khangulyan, D. 2013, The Astrophysical Journal, 774, 61

Kennel, C. F., & Coroniti, F. V. 1984, The Astrophysical Journal, 283, 710

Khangulyan, D., Aharonian, F. A., & Kelner, S. R. 2014, The Astrophysical Journal, 783, 100

Khangulyan, D., Bosch-Ramon, V., & Uchiyama, Y. 2018a, Monthly Notices of the Royal Astronomical Society, 481, 1455

Khangulyan, D., Koldoba, A. V., Ustyugova, G. V., Bogovalov, S. V., & Aharonian, F. 2018b, The Astrophysical Journal, 860, 59

Kimura, S. S., Murase, K., & Mészáros, P. 2020, arXiv e-prints, arXiv:2008.04515

Kisaka, S., & Kawanaka, N. 2012, Monthly Notices of the Royal Astronomical Society, 421, 3543

Komissarov, S. S., Barkov, M. V., Vlahakis, N., & Königl, A. 2007, Monthly Notices of the Royal Astronomical Society, 380, 51

Kotani, T., Kawai, N., Matsuoka, M., & Brinkmann, W. 1996, Publications of the Astronomical Society of Japan, 48, 619

Kraft, R. P., Forman, W. R., Jones, C., et al. 2002, The Astrophysical Journal, 569, 54

Kubota, K., Ueda, Y., Fabrika, S., et al. 2010, The Astrophysical Journal, 709, 1374

Lacki, B. C., & Beck, R. 2013, Monthly Notices of the Royal Astronomical Society, 430, 3171

Lacki, B. C., Thompson, T. A., & Quataert, E. 2010, Astrophys. J., 717, 1

Lacki, B. C., Thompson, T. A., Quataert, E., Loeb, A., & Waxman, E. 2011, The Astrophysical Journal, 734, 107

Lattimer, J. M., & Prakash, M. 2007, Phys. Rep., 442, 109

Lee, J., Hui, C. Y., Takata, J., & Lin, L. C. C. 2018, Astronomy & Astrophysics, 620, L14

Lee, S. K., Lisanti, M., Safdi, B. R., Slatyer, T. R., & Xue, W. 2016, Phys. Rev. Lett., 116, 051103

Lehmer, B. D., Alexander, D. M., Bauer, F. E., et al. 2010, The Astrophysical Journal, 724, 559

Li, J., Torres, D. F., Liu, R.-Y., et al. 2020, Nature Astronomy, arXiv:2008.10523

Licquia, T. C., & Newman, J. A. 2015, The Astrophysical Journal, 806, 96

Linden, T. 2017, Phys. Rev., D96, 083001

Linden, T., Auchettl, K., Bramante, J., et al. 2017, Physical Review D, 96, 103016

Linden, T., & Buckman, B. J. 2018, Physical Review Letters, 120, 121101

Lipari, P. 2017, Physical Review D, 95, 063009

Lockman, F. J., Blundell, K. M., & Goss, W. M. 2007, Monthly Notices of the Royal Astronomical Society, 381, 881

Lopez, L. A., Auchettl, K., Linden, T., et al. 2018, The Astrophysical Journal, 867, 44

Lorimer, D. R. 2013, in IAU Symposium, Vol. 291, Neutron Stars and Pulsars: Challenges and Opportunities after 80 years, ed. J. van Leeuwen, 237–242

Lorimer, D. R., et al. 2006, Mon. Not. R. Astron. Soc., 372, 777

Macias, O., Horiuchi, S., Kaplinghat, M., et al. 2019, Journal of Cosmology and Astroparticle Physics, 2019, 042

MAGIC Collaboration. 2019, Monthly Notices of the Royal Astronomical Society, 484, 2876

Magnelli, B., et al. 2015, Astronomy & Astrophysics, 573, A45

Magorrian, J., et al. 1998, The Astronomical Journal, 115, 2285

Malkov, M. A., Diamond, P. H., Sagdeev, R. Z., Aharonian, F. A., & Moskalenko, I. V. 2013, The Astrophysical Journal, 768, 73

Malofeev, V. M., & Malov, O. I. 1997, Nature, 389, 697

Manchester, R. N., Hobbs, G. B., Teoh, A., & Hobbs, M. 2005, VizieR Online Data Catalog, 7245

Mao, J., & Wang, J. 2007, The Astrophysical Journal, Letters, 669, L13

Margon, B., & Anderson, S. F. 1989, The Astrophysical Journal, 347, 448

Marshall, H. L., Canizares, C. R., & Schulz, N. S. 2002, The Astrophysical Journal, 564, 941

Martín, J., Torres, D. F., & Pedaletti, G. 2016, Mon. Not. R. Astron. Soc., 459, 3868

Marvil, J., Owen, F., & Eilek, J. 2015, The Astronomical Journal, 149, 32

Mathews, W. G., & Brighenti, F. 2003, Annual Review of Astronomy & Astrophysics, 41, 191

McDaniel, A., Jeltema, T., & Profumo, S. 2019, Physical Review D, 100, 023014

McEnery, J., van der Horst, A., Dominguez, A., et al. 2019, in Bulletin of the American Astronomical Society, Vol. 51, 245

McKinney, J. C., Tchekhovskoy, A., & Bland ford, R. D. 2012, Monthly Notices of the Royal Astronomical Society, 423, 3083

Medvedev, A., & Fabrika, S. 2010, Monthly Notices of the Royal Astronomical Society, 402, 479

Molina, E., & Bosch-Ramon, V. 2018, Astronomy and Astrophysics, 618, A146

Monceau-Baroux, R., Porth, O., Meliani, Z., & Keppens, R. 2014, Astronomy & Astrophysics, 561, A30

—. 2015, Astronomy & Astrophysics, 574, A143

Morić, I., Smolčić, V., Kimball, A., et al. 2010, The Astrophysical Journal, 724, 779

Morlino, G., & Amato, E. 2020, Physical Review D, 101, 083017

Mostafa, M., BenZvi, S., Schoorlemmer, H., Schüssler, F., & HAWC Collaboration. 2017, International Cosmic Ray Conference, 35, 851

Mostafa, M., & HAWC Collaboration. 2017, in APS April Meeting Abstracts, R4.005

Murase, K., & Waxman, E. 2016, Physical Review D, 94, 103006

Murphy, E. J., Helou, G., Kenney, J. D. P., Armus, L., & Braun, R. 2008, Astrophys. J., 678, 828

Murphy, E. J., Kenney, J. D. P., Helou, G., Chung, A., & Howell, J. H. 2009, Astrophys. J., 694, 1435

Murphy, E. J., et al. 2006, The Astrophysical Journal, 638, 157

Nava, L., Gabici, S., Marcowith, A., Morlino, G., & Ptuskin, V. S. 2016, Monthly Notices of the Royal Astronomical Society, 461, 3552

Ndiyavala, H., Venter, C., Johnson, T. J., et al. 2019, The Astrophysical Journal, 880, 53

Niklas, S., & Beck, R. 1997, Astronomy & Astrophysics, 320, 54

Noll, S., Burgarella, D., Giovannoli, E., et al. 2009, Astronomy & Astrophysics, 507, 1793

Noutsos, A., Schnitzeler, D. H. F. M., Keane, E. F., Kramer, M., & Johnston, S. 2013, Mon. Not. R. Astron. Soc., 430, 2281

Olmi, B., Del Zanna, L., Amato, E., Bucciantini, N., & Mignone, A. 2016, Journal of Plasma Physics, 82, 635820601

Orellana, M., Bordas, P., Bosch-Ramon, V., Romero, G. E., & Paredes, J. M. 2007, Astronomy & Astrophysics, 476, 9

O'Sullivan, S., Reville, B., & Taylor, A. M. 2009, Monthly Notices of the Royal Astronomical Society, 400, 248

Paladino, R., Murgia, M., Helfer, T. T., et al. 2006, Astronomy & Astrophysics, 456, 847

Panferov, A. 2014, Astronomy & Astrophysics, 562, A130

Panferov, A. A. 2017, Astronomy & Astrophysics, 599, A77

Park, J., Caprioli, D., & Spitkovsky, A. 2015, Physical Review Letters, 114, 085003

Pepe, C., Vila, G. S., & Romero, G. E. 2015, Astronomy & Astrophysics, 584, A95

Perucho, M., & Bosch-Ramon, V. 2008, Astronomy & Astrophysics, 482, 917

Petrović, J., Serpico, P. D., & Zaharijas, G. 2015, Journal of Cosmology and Astroparticle Physics, 2015, 023

Ploeg, H., Gordon, C., Crocker, R., & Macias, O. 2017, Journal of Cosmology and Astroparticle Physics, 2017, 015

Popescu, C. C., Yang, R., Tuffs, R. J., et al. 2017, Monthly Notices of the Royal Astronomical Society, 470, 2539

Popov, S. B., Pons, J. A., Miralles, J. A., Boldin, P. A., & Posselt, B. 2010, Mon. Not. R. Astron. Soc., 401, 2675

Popov, S. B., & Turolla, R. 2012, Astrophysics and Space Science, 341, 457

Porter, T. A., Jóhannesson, G., & Moskalenko, I. V. 2017a, The Astrophysical Journal, 846, 67

—. 2017b, The Astrophysical Journal, 846, 67

Posselt, B., Pavlov, G. G., Slane, P. O., et al. 2017, The Astrophysical Journal, 835, 66

Prodanović, T., Fields, B. D., & Beacom, J. F. 2007, Astroparticle Physics, 27, 10

Profumo, S., Reynoso-Cordova, J., Kaaz, N., & Silverman, M. 2018, Physical Review D, 97, 123008

Qiu, J., Shi, Y., Wang, J., Zhang, Z.-Y., & Zhou, L. 2017, The Astrophysical Journal, 846, 68

Rasul, K., Chadwick, P. M., Graham, J. A., & Brown, A. M. 2019, Monthly Notices of the Royal Astronomical Society, 485, 2970

Read, S. C., et al. 2018, Monthly Notices of the Royal Astronomical Society, 480, 5625

Rees, M. J., & Gunn, J. E. 1974, Mon. Not. R. Astron. Soc., 167, 1

Reynolds, S. P., Pavlov, G. G., Kargaltsev, O., et al. 2017, Space Science Reviews, 207, 175

Reynoso, M. M., & Carulli, A. M. 2019, Astroparticle Physics, 109, 25

Reynoso, M. M., Romero, G. E., & Christiansen, H. R. 2008, Monthly Notices of the Royal Astronomical Society, 387, 1745

Rickard, L. J., & Harvey, P. M. 1984, The Astronomical Journal, 89, 1520

Ridley, J. P., & Lorimer, D. R. 2010, Mon. Not. R. Astron. Soc., 406, L80

Riviere, C., Fleischhack, H., & Sandoval, A. 2017, The Astronomer's Telegram, 10941

Romero, G. E., Torres, D. F., Kaufman Bernadó, M. M., & Mirabel, I. F. 2003, Astronomy & Astrophysics, 410, L1

Romero, G. E., & Vila, G. S. 2008, Astronomy & Astrophysics, 485, 623

Rybicki, G. B., & Lightman, A. P. 1979, Radiative processes in astrophysics

Safi-Harb, S., & Ögelman, H. 1997, The Astrophysical Journal, 483, 868

Safi-Harb, S., & Petre, R. 1999, The Astrophysical Journal, 512, 784

Salim, S., Boquien, M., & Lee, J. C. 2018, The Astrophysical Journal, 859, 11

Salim, S., et al. 2009, The Astrophysical Journal, 700, 161

Salim, S., Lee, J. C., Janowiecki, S., et al. 2016, The Astrophysical Journal, Supplement, 227, 2

Sanders, R. H. 1983, The Astrophysical Journal, 266, 73

Sarbadhicary, S. K., Badenes, C., Chomiuk, L., Caprioli, D., & Huizenga, D. 2017, Monthly Notices of the Royal Astronomical Society, 464, 2326

Schleicher, D. R. G., & Beck, R. 2016, Astronomy & Astrophysics, 593, A77

Schoorlemmer, H., Lopez-Coto, R., & Hinton, J. 2017, International Cosmic Ray Conference,

35, 819

Shao, L., Koribalski, B. S., Wang, J., Ho, L. C., & Staveley-Smith, L. 2018, Monthly Notices of the Royal Astronomical Society, 479, 3509

Shapiro, S. L., & Teukolsky, S. A. 1983, Black holes, white dwarfs, and neutron stars: The physics of compact objects

Sick, J., Courteau, S., Cuilland re, J.-C., et al. 2015, in IAU Symposium, Vol. 311, Galaxy Masses as Constraints of Formation Models, ed. M. Cappellari & S. Courteau, 82–85

Sikora, M., Nalewajko, K., & Madejski, G. M. 2020, arXiv e-prints, arXiv:2004.03606

Sironi, L., Petropoulou, M., & Giannios, D. 2015, Monthly Notices of the Royal Astronomical Society, 450, 183

Slane, P., et al. 2018, The Astrophysical Journal, 865, 86

Snios, B., et al. 2019, The Astrophysical Journal, 871, 248

Solarz, A., Pollo, A., Bilicki, M., et al. 2019, Publications of the Astronomical Society of Japan, 71, 28

Song, D., Macias, O., & Horiuchi, S. 2019, Physical Review D, 99, 123020

Stafford, J. N., Lopez, L. A., Auchettl, K., & Holland-Ashford, T. 2019, The Astrophysical Journal, 884, 113

Stage, M. D., Allen, G. E., Houck, J. C., & Davis, J. E. 2006, Nature Physics, 2, 614

Stappers, B. W., Gaensler, B. M., Kaspi, V. M., van der Klis, M., & Lewin, W. H. G. 2003, Science, 299, 1372

Stawarz, Ł., Aharonian, F., Wagner, S., & Ostrowski, M. 2006, Monthly Notices of the Royal Astronomical Society, 371, 1705

Strong, A. W., Porter, T. A., Digel, S. W., et al. 2010, The Astrophysical Journal, Letters, 722, L58

Sun, X.-N., Yang, R.-Z., Liu, B., Xi, S.-Q., & Wang, X.-Y. 2019, Astronomy & Astrophysics, 626, A113

Szary, A., Zhang, B., Melikidze, G. I., Gil, J., & Xu, R.-X. 2014a, The Astrophysical Journal, 784, 59

—. 2014b, The Astrophysical Journal, 784, 59

Tabatabaei, F. S., et al. 2017, The Astrophysical Journal, 836, 185

Tanada, K., Kataoka, J., & Inoue, Y. 2019a, The Astrophysical Journal, 878, 139

—. 2019b, The Astrophysical Journal, 878, 139

Tanaka, S. J., & Takahara, F. 2010, The Astrophysical Journal, 715, 1248

Tang, X., & Piran, T. 2019, Monthly Notices of the Royal Astronomical Society, 484, 3491

Tatischeff, V. 2009, Astronomy & Astrophysics, 499, 191

Tauris, T. M., & Manchester, R. N. 1998, Mon. Not. R. Astron. Soc., 298, 625

Tauris, T. M., & van den Heuvel, E. P. J. 2006, Formation and evolution of compact stellar X-ray sources, Vol. 39, 623–665

Tavecchio, F., Maraschi, L., & Ghisellini, G. 1998, The Astrophysical Journal, 509, 608

Thompson, T. A., Quataert, E., & Waxman, E. 2007, The Astrophysical Journal, 654, 219

Thompson, T. A., Quataert, E., Waxman, E., Murray, N., & Martin, C. L. 2006, The Astrophysical Journal, 645, 186

Thorsett, S. E., Benjamin, R. A., Brisken, W. F., Golden, A., & Goss, W. M. 2003, Astrophys. J. Lett., 592, L71

Tibaldo, L., Zanin, R., Faggioli, G., et al. 2018, Astron. and Astrophys., 617, A78

Tingay, S. J., & Lenc, E. 2009, The Astronomical Journal, 138, 808

Tingay, S. J., et al. 1998, The Astronomical Journal, 115, 960

Torres, D. F. 2004, The Astrophysical Journal, 617, 966

Torres, D. F., Cillis, A., Martín, J., & de Oña Wilhelmi, E. 2014, Journal of High Energy Astrophysics, 1, 31

Torres-Albà, N., & Bosch-Ramon, V. 2019, Astronomy & Astrophysics, 623, A91

Trotta, R., Jóhannesson, G., Moskalenko, I. V., et al. 2011, The Astrophysical Journal, 729, 106

Tsuji, N., Uchiyama, Y., Aharonian, F., et al. 2019, The Astrophysical Journal, 877, 96

Uchiyama, H., Matsumoto, H., Tsuru, T. G., Koyama, K., & Bamba, A. 2009, Publ. Astron. Soc. Jpn., 61, S189

Uchiyama, Y., Aharonian, F. A., Tanaka, T., Takahashi, T., & Maeda, Y. 2007, Nature, 449, 576

van der Kruit, P. C. 1973a, Astronomy & Astrophysics, 29, 263

—. 1973b, Astronomy & Astrophysics, 29, 231

van der Swaluw, E., Downes, T. P., & Keegan, R. 2004, Astron. and Astrophys., 420, 937

van Rensburg, C., Krüger, P. P., & Venter, C. 2018, Mon. Not. R. Astron. Soc., 477, 3853

Venter, C., Kopp, A., Harding, A., Gonthier, P., & Büsching, I. 2015, Astrophys. J., 807, 130

Venter, C., Kopp, A., Harding, A. K., Gonthier, P. L., & Buesching, I. 2015, in International Cosmic Ray Conference, Vol. 34, 34th International Cosmic Ray Conference (ICRC2015), 462

Verbiest, J. P. W., Weisberg, J. M., Chael, A. A., Lee, K. J., & Lorimer, D. R. 2012, The Astrophysical Journal, 755, 39

Vieyro, F. L., Torres-Albà, N., & Bosch-Ramon, V. 2017, Astronomy & Astrophysics, 604, A57

Vila, G. S., & Romero, G. E. 2010, Monthly Notices of the Royal Astronomical Society, 403, 1457

Vorster, M. J., Tibolla, O., Ferreira, S. E. S., & Kaufmann, S. 2013, The Astrophysical Journal, 773, 139

Voss, R., & Gilfanov, M. 2007, Astronomy & Astrophysics, 468, 49

Waisberg, I., Dexter, J., Olivier-Petrucci, P., Dubus, G., & Perraut, K. 2019, Astronomy & Astrophysics, 624, A127

Wang, L., et al. 2019, Astronomy & Astrophysics, 631, A109

Watson, M. G., Willingale, R., Grindlay, J. E., & Seward, F. D. 1983, The Astrophysical Journal, 273, 688

Watters, K. P., & Romani, R. W. 2011, The Astrophysical Journal, 727, 123

Winter, M., Zaharijas, G., Bechtol, K., & Vand enbroucke, J. 2016, The Astrophysical Journal, Letters, 832, L6

Wykes, S., et al. 2013, Astronomy & Astrophysics, 558, A19

Wykes, S., Snios, B. T., Nulsen, P. E. J., et al. 2019, Monthly Notices of the Royal Astronomical Society, 485, 872

Xi, S.-Q., Liu, R.-Y., Huang, Z.-Q., Fang, K., & Wang, X.-Y. 2019, The Astrophysical Journal, 878, 104

Xing, Y., Wang, Z., Zhang, X., Chen, Y., & Jithesh, V. 2019, The Astrophysical Journal, 872, 25

Yamauchi, S., Kawai, N., & Aoki, T. 1994, Publications of the Astronomical Society of Japan, 46, L109

Yin, J., Hou, J. L., Prantzos, N., et al. 2009, Astronomy & Astrophysics, 505, 497

Yuan, Q., & Ioka, K. 2015, The Astrophysical Journal, 802, 124

Yüksel, H., Kistler, M. D., & Stanev, T. 2009, Physical Review Letters, 103, 051101

Yun, M. S., Reddy, N. A., & Condon, J. J. 2001, The Astrophysical Journal, 554, 803

Yusifov, I., & Küçük, I. 2004, Astron. and Astrophys., 422, 545

Zhang, J., Liang, E.-W., Zhang, S.-N., & Bai, J. M. 2012, The Astrophysical Journal, 752, 157

Zhu, B.-T., Zhang, L., & Fang, J. 2018, Astron. and Astrophys., 609, A110